MATERIAL DESIGN AND HYBRIDIZATION FOR GREEN CARBON DIOXIDE CAPTURE

LAU CHER HON

(B.Sc in Nanotechnology (Hons)),

Flinders University

A THESIS SUBMITTED FOR THE DEGREE OF

DOCTOR OF PHILOSOPHY

DEPARTMENT OF CHEMICAL AND

BIOMOLECULAR ENGINEERING

NATIONAL UNIVERSITY OF SINGAPORE

2011

ACKNOWLEDGEMENTS

Many written works include acknowledgements of those individuals who assisted the author. Though this seems to be an easy task, the question to when I should approach this section has been at the back of my head since the early stage of this research project. On one hand, I would like to complete this page way in advance so that I do not miss out the individuals who contributed, while on the other, it seems more appropriate that I mark the completion of the thesis with this section. Therefore in my final days prior to submission, I formally extend my gratitude to the mentioned for it would be an understatement to say that this thesis would be what it is without their suggestions and guidance.

First and foremost, I would like to sincerely thank my advisor, Professor Tai Shung (Neal) Chung, for his enthusiastic advice on various research and life aspects. His insistence on excellence in research and publications exemplifies a great model to replicate for my professional career. I am also deeply indebted to him for his efforts to improve my oral presentation and writing skills, and ability to perform under stress. I also appreciate the assistance from my mentors – Dr. Lu Shao and Dr. Songlin Liu – for their invaluable comments and discussions, which were particularly insightful for research progress while bringing it to a higher level. I would also like to acknowledge the help rendered from Professor Donald R. Paul – for numerous suggestions, discussions and

communications to move this project along.

Several people have contributed to this project in various ways. In particular, Dr. Ming Lin and Ms. Joyce Tan at the Institute of Materials Research and Engineering (IMRE), Singapore whom provided the use of scanning transmission electron microscopy for material characterizations. Mr. Daniel Li from IMRE is responsible for XPS data reported in this dissertation. Mr Poh Chong Lim from IMRE provided help on the wide-angle x-ray diffraction data used in this dissertation. Professor Jerry Jean and Dr. Hongmin Chen at the University of Missouri-Kansas City, USA guided me on bulk positron annihilation lifetime spectroscopy measurements. I would also like to acknowledge the use of NMR facilities in the Department of Chemistry, and high-resolution TEM facilities in the Department of Biological Sciences at the National University of Singapore. Ms Yanhui Han conducted the ^{13}C and ^{29}Si NMR measurements. I would also like to gratefully acknowledge the financial support by the National Research Foundation, under grant number R-279-000-261-281.

It has been pleasant to work with people in the Chung Membrane Research group. I am very grateful for their technical assistance and support. In particular, interactions with the following members have been helpful and productive: Dr. Yi Li, Dr. Na Peng, Dr. Bee Ting Low, Dr. Pei Li, Hangzheng Chen, Fuyun Li, Huan Wang, Jianzhong Xia, and Meiling Chua. Very special

thanks go to Dr. Youchang Xiao and Dr. Kaiyu Wang, who has provided guidance for equipment troubleshooting in my early days in the laboratory.

Finally, I thank my wife, Lilian Liang and son, Zyven Lau for instilling me the greatest motivation to learn and constant love and support.

TABLE OF CONTENTS

SUMMARY

To provide an impetus for a green technology like membranes for carbon dioxide (CO_2) capture, the trade-off relationship between gas permeability and selectivity in membranes must be overcome. An elegant and simple approach to overcome this trade-off relationship is to transform the chemical structures of current polymeric materials in a fashion that enhances both gas permeability and gas selectivity.

In this work, the trade-off relationship between gas permeability and selectivity in glassy polymeric materials for e.g. polyimides is abated via an innovative technique – vapor phase modification that is traditionally used in lithography and nanotube alignment. Traditionally, solution crosslinking is used to overcome the aforementioned trade-off between gas permeability and selectivity. The main problem with solution cross-linking is its inability to maintain structural integrity in hollow fiber membranes, the preferred physical configurations of membranes in the industry. By converting the polyimide structures into dense polyamide structures via the vapor of crosslinking agents, gas selectivity was enhanced whilst retaining structural integrity in hollow fiber membranes.

In another part of this work, material design and hybridization was used to improve the CO_2 permeation properties of polyethylene oxide (PEO), a well-known material with high CO_2 affinity. Silicate nanoparticles were fabricated *in-situ* a PEO-based matrix via a sol-gel approach. The CO_2 transport and CO_2/H_2 separation properties of this organic-inorganic material resemble current state-of-the-art cross-linked PEO rubbers. However, the CO_2 transport properties of this organic-inorganic material remain inferior to polydimethylsiloxane – the preferred gas separation material in current industries. To enhance its CO_2 and CO_2/H_2 transport and separation properties, alkyl chains were grafted onto the main chains of the organic-inorganic material. The resultant nanohybrid material possesses CO_2 permeability that is similar to polydimethylsiloxane. However, the CO_2/H_2 selectivity of this material is much higher than those observed in polydimethylsiloxane, and is comparable with state-of-the-art cross-linked PEO rubbers.

Synthesis parameters like water/silicon ratio, organic/inorganic ratio, graft content and sol-gel synthesis conditions like hydrolysis durations and condensation durations were discovered to be fundamental to attune the CO_2 transport and separation properties of the nanohybrid materials. To obtain optimal nanohybrid membranes, an intricate combination of synthesis parameters and conditions is required. This work reveals that by combining 30 minutes of hydrolysis duration with 1 hour of condensation duration for the

synthesis of nanohybrid membranes consisting 80 wt.% polyether diamines, 20 wt.% alkoxysilanes and 20 wt.% alkyl chain grafts (with respect to the weight of the base material) could yield a CO_2 permeability of about 2000 Barrer and CO_2/H_2 and CO_2/N_2 selectivities of 10.5, and 55.6 respectively. The high CO_2 transport and separation properties of these nanohybrid membranes have pushed the boundaries of using polymeric membranes for CO_2 capture to newer heights.

LIST OF TABLES

LIST OF FIGURES

LIST OF ABBREVIATIONS

Carbon dioxide	CO_2
Hydrogen	H_2
Nitrogen	N_2
Helium	He
Oxygen	O_2
Methane	CH_4
Argon	Ar
Xenon	Xe
Monoethanolamine	MEA
Pressure swing adsorption	PSA
Pore size radius	r
Mean free path of gas molecules	λ
Gas permeability	P
Steady-state gas flux	N
Downstream pressure	p_1
Upstream pressure	p_2
Atmosphere	atm
Standard temperature and pressure	STP
Gas local diffusion coefficient	D_{loc}
Gas concentration dissolved in polymer	C
Weight fraction of gas in membrane	w

Gas solubility coefficient	S
Gas diffusivity coefficient	D
Gas selectivity	α
Henry's Law constant	k_D
Langmuir capacity	C'_H
Langmuir affinity	b
Local effective diffusion coefficient	D_{eff}
Fractional free volume	FFV
Glass transition temperature	T_g
Poly (1-trimethylsilyl-2-propyne)	PTMSP
Poly (4-methyl-2-pentyne)	PMP
Polymers of intrinsic microporosity	PIMs
2,2'-bis (3,4-dicarboxylphenyl) hexafluoropropane dianhydride	6FDA
Tetrahydrofuran	THF
Ultraviolet	UV
4-4' (hexafluoroisopropylidene) diphenyl azide	HFBAA
1,2,4,5-tetramethylbenzene	Durene
1,3-cyclohexanebis (methylamine)	CHBA
Ethylenediamine	EDA
1,3-propane diamine	PDA
1,2-butane diamine	BuDA
Polydimethylsiloxane	PDMS

Polyethylene oxide	PEO
Ethylene oxide	EO
Poly (butylene-terephthalate)	PET
Poly (amide-b-ethylene oxide)	PEBAX®
Fumed silica	FS
Interpenetrating networks	IPNs
Polyhedral oligomeric silsesquioxane	POSS
Field emission scanning electron microscopy	FESEM
High resolution transmission electron microscopy	HRTEM
High angle annular dark field	HAADF
Scanning transmission electron microscopy	STEM
Energy dispersive x-ray spectroscopy	EDX
Atomic number	Z
Fourier transform infra-red spectroscopy	FTIR
Nuclear magnetic resonance microscopy	NMR
Carbon-13	^{13}C
Silicon-29	^{29}Si
X-ray photoelectron spectroscopy	XPS
Differential scanning calorimetry	DSC
Apparent heat of fusion per gram of materials	ΔH_f
Thermodynamic heat of fusion per gram of materials	ΔH^0_f
Positron annihilation lifetime spectroscopy	PALS

Sodium chloride	NaCl
Sodium-22	^{22}Na
Ortho-positroniums	*o*-Ps
Lifetime of ortho-positroniums	τ_3
Intensity of ortho-positroniums	I_3
Free volume cavities	V_f
Downstream pressure built up rate	dp/dt
Film thickness	L
Volume of downstream chamber	V
Effective membrane area	A
Operating temperature of permeation cell	T
Molar fraction of gas in feed gas	*x*
Molar fraction of gas in permeate	*y*
Upstream	US
Downstream	DS
Internal downstream	INT-DS
Pressure transducer	PT
Pressure gauge	PG
Gas chromatograph	GC
Poly (3-butylthiophene)	P3BT
N-methyl-pyrrolidone	NMP
Dimethylacetamide	DMAc

Polysulfone	PSf
Polyethersulfone	PES
1,5-napthalenediamine	NDA
Polybenzimidazole	PBI
Polytetrafluroethylene	PTFE
Polypropylene oxide	PPO
Polyethylene glycol methacrylate	PEGMA
3-glycidyloxypropyltrimethoxysilane	GOTMS
Hydrochloric acid	HCl
Polyether diamine-silicate	PEDS
Polyether diamine-silicate materials grafted with PEGMA	PEDS-Pxx
Activation energy for permeation	E_p
Butyl methacrylate	BuMA
Polyether diamine-silicate materials grafted with BuMA	PEDS-Bxx
Polyether diamine-silicate materials blended with PEGMA	PEDS-Pxx(blend)

CHAPTER ONE:

INTRODUCTION

1.1 CO_2 capture for gas purification

The main cause of global warming is greenhouse gas emissions, in particular, CO_2 emissions. To mitigate the greenhouse effects of CO_2 emissions, strategies to achieve zero-emissions must be adopted. More than 50% of CO_2 emissions result from hydrocarbon combustion in power plants, industrial processes and transportation fuels [1]. In the short term, it is unlikely to replace hydrocarbons with alternative clean energy/fuel sources. Hence, the current emphasis is focused on clean, green techniques that can reduce the carbon footprint of existing energy/fuel production technologies. This objective can be achieved by integrating carbon capture technologies into high footprint industrial applications like hydrogen production, and the purification of nitrogen in flue gases.

Currently, 95 % of global hydrogen production is achieved via the steam reforming of hydrocarbons [2]:

$C_nH_m + nH_2O \xrightarrow[\Delta Heat]{} nCO + (\frac{m}{2} + n)H_2$ (Steam methane reforming)

followed by a water-gas shift reaction that converts CO to CO_2, while increasing H_2 content [2]:

$CO + H_2O \rightarrow CO_2 + H_2$ (Water gas shift reaction)

To obtain high purity H_2 for other applications like hydrocarbon cracking and ammonia production [3], the CO_2 byproduct in the water-gas shift reaction must be sequestered. Prior to using industrial applications of green hydrogen production techniques, steam methane-reforming remains the preferred approach for industrial hydrogen production. As H_2 has been identified as an alternative for petroleum and heavy hydrocarbons as a mainstay fuel and energy source, hydrogen usage is expected to increase exponentially in the next few decades [4]. Thus, it is important for researchers to improve on current purification techniques that facilitate simultaneous CO_2 capture and H_2 purification. Meanwhile, in coal-fired power plants, CO_2 is commonly found in the gaseous byproduct of flue gas. The CO_2 concentration in this low-pressure (1 atm) flue gas is typically 10 - 15%, while N_2 concentration is usually 67% [5]. The N_2 can be isolated from the flue gas, purified, and recycled as a raw material for the food preservation industry [6]. A common characteristic of these industrial processes is the need for CO_2 capture prior to further applications of the desired gas stream. CO_2 capture is categorized into post- and pre- combustion capture, and can be achieved using effective techniques like pressure swing adsorption [7], amine absorption [8], and cryogenic carbon capture [9].

In most amine absorption systems, monoethanolamine (MEA) is usually used to selectively absorb CO_2. **Figure 1.1** shows a standard CO_2 capture process using amine absorption [10] whereby the flue gas comes into contact with aqueous MEA in the absorber. The CO_2-rich MEA is subsequently heated in a stripper to release high purity CO_2 while the CO_2-lean MEA solution is then recycled to the absorber. Typically a compression step is mandatory to facilitate CO_2 transport and storage, where CO_2 is compressed to 100 atm or more. The main limitation of amine absorption systems is high-energy consumption during the recycling of MEA solution, and the mandatory post-compression step. However, this post-combustion CO_2 capture approach is still widely used in power plants because of its high compatibility and flexibility with current technology and the slow development of green power plants. Recently, pressure swing adsorption systems have also been identified as a replacement for these absorption-based post-combustion CO_2 capture techniques [7].

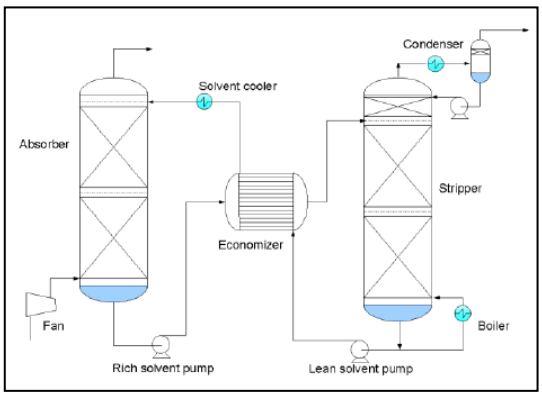

Figure 1.1 A typical post-combustion CO_2 capture process [10].

Pressure swing adsorption (PSA) systems are commonly used for pre-combustion CO_2 capture [11]. In these PSA systems, a high pressure feed gas; in this case, a CO_2 and H_2 gas mixture, comes into contact with a bed of microporous-mesoporous solid adsorbents. CO_2 is preferentially adsorbed onto the heterogeneous solid adsorbents while a CO_2-lean H_2 gas stream is produced. A low-pressure desorption process is usually required to release the adsorbed CO_2. This desorption process does not require any external heat sources [12]. **Figure 1.2** illustrates a double-bed PSA swing system [13]. Due to its capability to work with low CO_2 concentrations, pre-combustion CO_2 capture is preferred over post-combustion methods. The main limitation of pre-combustion CO_2 capture technologies is the requirement for very high gas separation efficiencies and high-energy consumption.

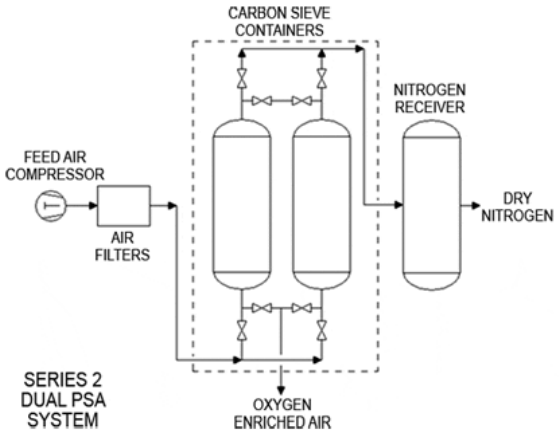

Figure 1.2 A double bed PSA system [13].

A common trait amongst the aforementioned traditional CO_2-capture techniques is the large energy requirements by the CO_2-capture processes. Additionally,

the amine-regeneration process does not guarantee 100% regeneration. Exorbitant fuel costs and depleted hydrocarbon resources, raise energy prices that significantly increase the operating costs of CO_2–capture techniques. Hence, there is an impending need to identify alternative and affordable technologies that can capture CO_2 with low carbon footprints, whilst alleviating our over-reliance on hydrocarbons. Moreover, using high carbon footprint techniques to aid in the production of a green energy and fuel source like hydrogen becomes a futility of identifying which requirement is more important i.e. a circular reference. Therefore, it is of paramount importance that an affordable, green technique for gas purification is identified and improved on.

1.2 Membrane technology

Alternatively, CO_2 capture can be realized using membrane technology [14-19]. The advantages of membrane technology over traditional CO_2 capture techniques are low cost, ease of application, a lack of moving parts and most importantly, low carbon footprint [16, 17, 19]. Thus, averting high-energy costs that are associated with adsorption and desorption processes. Moreover, membrane characteristics can be specifically tailored to application requirements. For example, in the case of CO_2/H_2 separation, if low purity (~ 80 %) H_2 is desired as a combustion fuel, size-selective membranes can be used to purify the feedstock gas mixture so that the desired smaller H_2 gas molecules product end up in a low pressure permeate, while retaining the CO_2 at high

pressures that are ideal for CO_2 transportation and storage. This way, the H_2 decompression step prior to combustion becomes invalid. In a different manner, high purity (~ 99.99999 %) H_2 for transportation fuel can be obtained using reverse-selective membranes in several stages so that CO_2 permeates to low pressures while H_2 is retained in high pressures that are similar to the feed pressure. This approach voids the mandatory recompression step for H_2 transportation and storage.

Since the first commercial application of polymeric membrane systems for H_2 purification via gas separation in 1980 [17], the use of gas separation membranes has been well-established and documented [20]. Although the market share for gas separation polymeric membranes applicable is relatively small when compared to other applications (**Figure 1.3**) [21], it accounted for about US $170 million/year with an expected growth rate higher than 7 % per annum [20].

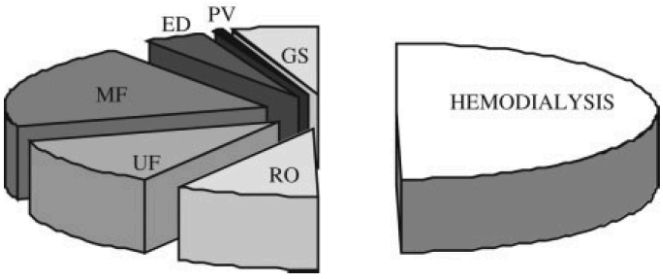

Figure 1.3 Market share of membranes for different applications like reverse osmosis (RO), ultrafiltration (UF), microfiltration (MF), electrically driven membrane processes (ED), pervaporation (PV) and gas separation (GS) in 1998 [21].

Gas separation membranes can be fabricated using organic polymers [22-25], inorganic materials [26, 27], or a combination of both [28, 29]. Gas separation membranes mainly exist in the forms of (1) flat, dense sheet membranes, (2) hollow fiber membranes, (3) spiral wound membranes and (4) tubular structures. Self-supporting hollow fiber membranes are much preferred in the industries. Hollow fiber membranes possess large surface area to volume ratios i.e. gas separation can be achieved using less material and they can also be easily assembled into module systems. Flat sheet dense membranes can be used in spiral wound membranes. Commercially available inorganic membranes consist of palladium, an expensive rare metal, while nanocomposites are rarely used in commercial gas separation. Ascribing to good moldability and inherent gas selectivities, organic polymers are the preferred choice over other membrane materials. The main disadvantage of current commercial polymeric membranes over traditional CO_2-capture techniques is their inabilities to achieve efficient gas separation. Compared to traditional CO_2 capture techniques, the gas permeability and selectivity of current commercial membranes remain inadequate. Hence, it is evident that gas selectivities and permeabilities of membranes must be significantly enhanced prior to widespread commercial applications of gas separation membranes.

1.3 Objectives and Organization of the Thesis

Imperative to industrial applications of gas separation membranes, high gas permeability and excellent permselectivity in membrane materials are highly desired. Naturally, such materials do not exist i.e. gas permeability and selectivity exist in a trade-off relationship. Alternative approaches to fabricate such membrane materials are (1) to molecularly design new materials so that gas transportation can be achieved at desired rates alongside excellent separation capabilities, (2) modify existing membrane materials to improve their gas separation capabilities, and (3) material hybridization using organic and inorganic materials. Adopting the latter two strategies, the objective of this dissertation is to develop multi-purpose gas separation membranes that can be used for the purification of H_2 and N_2 for various applications ranging from combustion fuel to transportation fuel to food preservation, while capturing CO_2 in a green manner.

Inclusive of this introduction chapter, this dissertation consists of ten chapters. The background and theory of gas transport and separation in glassy and rubbery materials, and different modification approaches that can be used to enhance gas transport and separation properties of membranes are presented in Chapter 2. Chapter 3 reveals the experimental methods used in this work. Chapters 4 and 5 discuss the effects of vapor phase modification on flat sheet and hollow fiber gas separation membranes made up of glassy materials,

respectively. The industrial application of the vapor phase modification technique is also discussed in Chapter 5.

The subsequent chapters focus on organic-inorganic nanohybrid rubbery materials synthesized from a sol-gel process. Chapter 6 expounds the modification of a base organic-inorganic nanohybrid material via wet ozonolysis and the gas (CO_2 and H_2) permeations and CO_2/H_2 selectivity of these nanohybrid membranes. Chapter 7 details effects of the ratio between organic and inorganic components on the pure gas permeation, solubility and diffusivity coefficients and ideal CO_2/H_2 selectivity. Chapter 8 describes the effects of hydrolysis, condensation, and ozonolysis durations on the structural conformation of the inorganic phase, the phase dispersion between the organic and the inorganic phases and how these physical differences attribute to pure (CO_2, and H_2) and mixed gas (CO_2/H_2) permeations. Chapter 9 investigates the effects of different modification types and the side chain length on the gas permeation properties of these nanohybrid membranes. Additionally, the N_2 permeability of these nanohybrid membranes is also revealed in Chapter 9. Chapter 10 summarizes this dissertation with the conclusions and recommendations for future work.

CHAPTER TWO:

BACKGROUND AND THEORY

2.1 Theory

2.1.1 Fundamentals of membrane gas separation

In membranes, gas molecules can be transported via (1) Poiseuille flow, (2) Knudsen diffusion, (3) molecular sieving, (4) surface diffusion, and (5) solution-diffusion [14, 30]. Poiseuille flow occurs in porous membranes whereby the pore radius size (r) is larger than the mean free path (λ) of the gas molecules. Collisions between gas penetrant molecules are more likely to happen than collisions between gas penetrant molecules and pore walls in Poiseuille flow. Knudsen diffusion happens in smaller pore sizes of porous membranes whereby the flow of gas penetrants are independent of one another. The $\frac{r}{\lambda}$ value differentiates Poiseuille flow ($\frac{r}{\lambda} >> 1$) from Knudsen diffusion ($\frac{r}{\lambda} << 1$). Molecular sieving is common in membranes consisting of pore sizes that are narrow enough to allow small-sized gas penetrants to diffuse across the membrane while physically retaining the larger gas penetrants. The operating mechanism of molecular sieving is based on the higher diffusion rate of small-sized gas penetrants.

Solution-diffusion, whereby gas sorption plays an equally important role as diffusion rates, is the preferred approach to separate gases of similar sizes. Surface diffusion takes place when surface gas adsorption reaches its threshold

value. Ascribing to a pressure gradient, adsorbed gas molecules preferentially diffuse across the membrane. Solution-diffusion ensues in the absence of direct, continuous gas transportation pathways (pores) in dense, non-porous polymeric membranes. In solution-diffusion transport, the transport of small gas molecules is governed by diffusion rates while the transport of condensable gas molecules is determined by dissolvability rates.

2.1.2 Permeability and selectivity

The steady-state permeability of gas A (P_A) across a membrane with a film thickness, L, is defined as [30, 31]:

$$P_A = \frac{N_A}{(p_2 - p_1)} = \frac{N_A}{-\Delta p / L} \qquad \text{Equation 2.1}$$

where N_A is the steady-state gas flux across the membrane, p_1 and p_2 are the downstream (low) and upstream (high) partial pressures, respectively, and L is the thickness of the membrane. Membrane permeability is expressed in Barrer, where 1 Barrer equates to 10^{-10} cm^3 (STP)-cm / cm^2 sec cm Hg [32, 33].

Fick's Law describes the one-dimensional flux of a gas (Gas A) through a membrane film in the x direction [30]:

$$N_A = \frac{D_{loc}}{1 - w_A} \frac{dC_A}{dx}$$ Equation 2.2

where D_{loc} is the gas local diffusion coefficient in the film, C_A, is the concentration of gas A dissolved in the polymer matrix i.e. local concentration, and w_A is the weight fraction of gas A in the membrane film.

The integral of Equation 2.1 combined with Equation 2.2 from $x = 0$ ($C = C_2$) to $x = l$ ($C = C_1$) yields Equation 2.3.

$$P_A = D_A \frac{C_2 - C_1}{p_2 - p_1}$$ Equation 2.3

D_A is the average effective diffusion coefficient between C_1 to C_2. Gas permeation experiments are usually set up in a way that $p_1 << p_2$ and $C_1 << C_2$ so that Equation 2.3 reduces to:

$P_A = D_A \times S_A$ Equation 2.4

where S_A, the apparent sorption coefficient or the solubility of penetrant A in the membrane material at the upstream pressure is expressed as:

$S_A = C_2 / p_2$ Equation 2.5

The ideal selectivity of a membrane for gas A over gas B is the ratio of their ideal gas permeabilities that can be expressed as a product of the diffusivity $\left(\frac{D_A}{D_B}\right)$ and solubility $\left(\frac{S_A}{S_B}\right)$ selectivities:

$$\alpha_{A/B} = \frac{P_A}{P_B} = \frac{D_A}{D_B} \times \frac{S_A}{S_B} \qquad \text{Equation 2.6}$$

2.1.3 Solubility

Gas solubility in polymeric membranes rely on gas condensability that is closely related to the critical temperature of the gas, interaction between the gas penetrant and polymer matrix, and weakly with polymer free volume. **Table 2.1** shows the critical temperature of some common gases. Depending on polymer type, gas sorption can be described using Henry's law (rubbery polymers) [34] and the dual sorption model (glassy polymers) [35, 36].

Table 2.1 Critical volumes and temperatures of some common gases [37].

	Size (critical volume (cm^3/mole))	Condensability (critical temperature (K))
He	57.4	5.19
H_2	65.1	33.24

O_2	73.4	154.6
N_2	89.8	126.2
CO_2	93.9	304.21
CH_4	99.2	191.05

Gas solubility in rubbery polymers are independent of the gas penetrant concentration in the polymer and is usually expressed using the Henry's law [34]:

$$C = k_D p \qquad \text{Equation 2.7}$$

where k_D (cm^3 gas (STP)/ cm^3 polymer bar) is the solubility coefficient, or Henry's law constant. Gas sorption obeying the Henry's law usually occurs via swelled existing free volume or newly created sorption sites in rubbery polymers.

The dual sorption model is defined as [35]:

$$C = k_D p + \frac{C'_H bp}{1 + bp} \qquad \text{Equation 2.8}$$

where C'_H (cm^3 gas (STP)/cm^3 polymer) is the Langmuir capacity and *b* (1/bar) is the Langmuir affinity. C'_H describes the sorption capacity of the equilibrium excess free volume related to the glassy state of the polymer while *b* is an equilibrium constant that includes the penetrant affinity for Langmuir sorption sites in the polymeric matrix. In the dual sorption model, glassy polymers are considered to comprise a homogeneous dense polymer matrix (akin to a rubbery polymer) with embedded cavity pockets. Gas sorption in the homogeneous dense polymer matrix is described using Henry's law while the cavities are fixed independent sorption sites that correspond to non-equilibrium excess free volume. Sorption in these cavities is described as Langmuir sorption.

2.1.4 Diffusivity

The local effective diffusion coefficient, D_{eff}, describes the penetrant diffusivity in the polymer at a penetrant concentration of C_2 and is expressed as [38]:

$$D_{eff}(\mathrm{C}_2) = \left[P_A + p \frac{dP_A}{dp} \right]_{\mathrm{p}_2} \left(\frac{dp}{dC_2} \right)_{\mathrm{p}_2} \qquad \text{Equation 2.9}$$

From Equation 2.9, it is obvious that D_{eff} can be calculated using measured values of gas permeability and solubility. Gas diffusivity can be described as a function of the fractional free volume (FFV) in the polymer (as shown in

Equation 2.10) and the polymer chain flexibility that is often characterized using the polymer glass transition temperature (T_g):

$$D_A = A_D \exp\left(-\frac{B}{FFV}\right) \qquad \text{Equation 2.10}$$

where A_D is a pre-exponential factor, and B is a constant dependent on penetrant size.

2.2 Background

2.2.1 Glassy polymers for gas separation

The T_g of polymers is the predominant factor that differentiates glassy polymers from their rubbery counterparts. Glassy polymers are generally rigid and brittle below T_g, while becoming rubbery-like above T_g. This behavior is intrinsically linked with material structure.

The molecular structure of glassy polymers is typically formed from long polymer chains, and complex networks of atoms or molecules. Below T_g, most bonds remain intact and the molecules or atoms vibrate slightly in their fixed positions. Hence, glassy polymers with high T_g remain hard, rigid, and possibly brittle at room temperature. Glassy polymers that are commonly used as gas separation membranes possess a T_g higher than 25 °C. These materials are

used in most industrial membrane gas separation applications because of good selectivity and high durability. In most glassy materials, gas separation is mainly achieved through size selection i.e. smaller gas penetrants are preferentially allowed to permeate across the membrane [39-41]. Interesting examples of glassy materials used in gas separation membranes are poly (1-trimethylsilyl-1-propyne) (PTMSP), poly (4-methyl-2-pentyne) (PMP), polymers of intrinsic porosity (PIMs), thermally re-arranged polymers and polyimides.

PTMSP and PMP are super glassy polymers with high free volume content that display outstanding gas permeability and high vapor/gas selectivity. Merkel et al. reported a butane/methane mixed gas selectivity of 22 with butane permeability reaching 26,000 Barrer in PMP nanocomposites consisting of fumed silica nanoparticles [28]. The introduction of fumed silica nanoparticles to PTMSP also enhanced methane permeability by 180 % [39]. Although these materials are highly condensable and permeable to vapors, the physical aging effects on polymer structure circumvent industrial application [16].

PIMs are obtained by inhibiting chain packing through minimal contortion to a backbone with little conformational movement [42]. Unlike other glassy polymers, interconnectivity between small pores (less than 2 nm) in PIMs can be tailored using polymer chemistry. The permeability order in PIMs is CO_2 > H_2 > He > O_2 > Ar > CH_4 > N_2 > Xe, while in most glassy polymers He > CO_2

[43]. Another type of glassy polymer suitable for gas separation is a thermally re-arranged polymer. Using dense glassy polybenzoxazoles and polybenzothiazoles, Park et al. fabricated gas separation membranes possessing outstanding molecular and ionic transport [44]. In these “thermally rearranged polymers”, free volume concentration is enhanced via a thermal decarboxylation of precursor polyimides that induces changes in chain conformations and spatial location of free volumes. Small gas penetrants are allowed to permeate through hourglass-shaped pores while these uniquely shaped pores hinder the gas transport avenues of bigger gas penetrants, in particular, CO_2 separation from CH_4.

Attributing to excellent thermal, chemical, and mechanical properties, polyimides can be used to fabricate gas separation membranes. Compared to other glassy materials like polysulfones and polycarbonates, polyimides display higher gas selectivity for most gas pairs. As polyimides are synthesized over the polycondensation of dianhydrides and diamines, membrane gas transportation properties can be tailored to application requirements via monomer selection. Homopolyimides can be prepared from a variety of dianhydride and diamine combinations, while copolyimides are usually synthesized using two or more dianhydrides and/or diamines. Prior to widespread usage of polyimides as gas separation membranes, the free volume

of this material must be increased so that gas transportation can be enhanced while maintaining good gas selectivity.

Two important parameters that determine the gas transport characteristics of polyimide membranes for gas separation are chain packing density and local polymer chain mobility [19]. The packing density of polyimides depends on chain stiffness (a rough measure of T_g), strength of polymer chain-chain interactions and chain bulkiness. For example, stiff aromatic moieties with low degrees of conformational freedom cause less efficiency in chain packing. Moreover, aromatic moieties exert strong steric hindrance effects [45] that weaken the chain-chain interaction and consequently inefficient chain packing. Besides van der Waals and polar interactions, charge transfer interactions between the dianhydride and diamine moieties contribute significantly to the chain-chain interactions in aromatic polyimides [46, 47]. These interactions are dependent on the electron affinity of the dianhydride and the ionization potential of the diamine and are facilitated in the presence of electron-withdrawing substituents on the benzene ring in the dianhydride moiety e.g. a CF_3 moiety. Stronger charge transfer interactions enhance chain packing efficiency. A method to reduce the strength of charge transfer interactions is to reduce the electron affinity of the dianhydride moiety by disrupting its π-electrons via the introduction of $–C(CF_3)_2-$ moieties [41, 48]. Bulky $-C(CF_3)_2-$ moieties also contribute to inefficient chain packing. Kink units i.e. units that are nonplanar to

main polymer chain also reduce chain packing. For example, when moieties are located at the *ortho* positions to each aromatic ring, the internal rotation around the bond between the diamine and imide ring is sterically inhibited [49]. Chain packing density determines the FFV i.e. the empty space in between the functional groups in the polymer chains that is unoccupied by the electron clouds; and size distribution of free volume holes. With inefficient chain packing i.e. low chain packing density, FFV content increases [50]. For example, inefficient polymer chain packing is prevalent in 2,2'-bis (3,4-dicarboxyphenyl) hexafluoropropane dianhydride (6FDA) -based polyimides. Diffusivity selectivity depends on the local mobility of polymer chains. Local motions of polymer chain and side groups are fundamental for the generation and spatial confinement of small free volume holes in the glassy state. Restricted local motion rigidifies gas transport channels and prevents the diffusion of large gas penetrants. The presence of bulky groups in the polymer chains constricts local motion e.g. CF_3 moieties in 6FDA-based polyimides restrict torsional motion of neighboring aromatic rings.

2.2.2 Modifications of glassy polymer membranes

Although the advantages of using glassy materials as gas separation membranes are highlighted in Section 2.2.1, its widespread usage in industrial membrane gas separation is uncommon when compared to the benchmark industry gas separation polymer, silicone rubber. This is ascribed to physical

aging effects on gas permeability (that is already inadequate for industrial applications when compared to silicone rubber) and plasticization. Plasticization of glassy materials significantly affects gas selectivity [19, 51, 52]. For example, in CO_2/H_2 separation, CO_2 sorption swells a polymeric membrane and accelerates the permeation of H_2. Consequently, the membrane loses its CO_2/H_2 selectivity. Modifications to the chemical structure of these materials can overcome aging [53] and plasticization [47, 52].

Cross-linking, a polymer modification process that covalently or ionically binds polymer chains together, first came into prominence in the 19th century. In 1839, rubber was thermally cross-linked with sulfur by Charles Goodyear [54]. Since then, cross-linking has been used in synthetic polymer chemistry and biological sciences. Cross-linking can also be used to modify gas separation membranes [52, 55-57]. For example, to address the issue of aging in PTMSP, Jia et al. cross-linked PTMSP with 1- 5 wt.% of bis(aryl azide) via UV irradiation or thermal annealing at 180 °C [58]. Compared to pristine PTMSP, O_2 and N_2 permeabilities of cross-linked PTMSP decreased while O_2/N_2 selectivity increased. This comparison is consistent with free volume reduction that is a result of cross-linking. Photochemical modifications induced higher increments in O_2/N_2 selectivity when compared to thermally modified PTMSP. Upon cross-linking, the chemical resistance of PTMSP in toluene and tetrahydrofuran (THF), both good solvents for PTMSP, was enhanced. These observations were

evident in the works of Kelman et al. when the cross-linking of PTMSP was achieved using fumed silica [59], and polysiloxysilsesquioxanes [60]. A common trait of these cross-linked PTMSP membranes is their ability to withstand aging only in a vacuum environment. When exposed to air, aging still occurs in cross-linked PTMSP membrane, albeit at a reduced rate when compared to pristine PTMSP membranes. Aging in PTMSP can be attributed to its unstable chemical structure and impurities in the atmosphere that can react with PTMSP. Hence, the use of PMP is preferred over PTMSP.

Shao et al. cross-linked PMP with 4-4'(hexafluoroisopropylidene) diphenyl azide (HFBAA) to improve chemical and physical stability over time [61]. Gas permeation decreased with longer cross-linking durations. The reduced gas permeabilities are caused by the reductions in gas diffusion coefficients, consistent with reduced free volume content. However, the introduction of nanoparticles like fumed silica and TiO_2 enhanced gas permeability while maintaining gas selectivity similar to cross-linked PMP membranes [62]. Meanwhile, chemical and physical stability were maintained over time in these nanoparticle-filled cross-linked PMP membranes. The cross-linking of PMP and PTMSP is achieved typically via photochemical or thermal means. These approaches are impractical for large-scale membrane modifications. Another straightforward cross-linking method that has been commonly used by researchers to modify glassy materials is solution cross-linking.

Liu et al. developed a clear-cut technology that chemically modifies polyimide membranes at room temperature [53]. In Liu et al.'s approach, a 6FDA-1,2,4,5-tetramethylbenzene (durene) polyimide flat-sheet membrane was immersed in a solution comprising methanol and *p*-xylenediamine for stipulated times. Subsequently, the polyimide membranes were washed with fresh methanol and dried at ambient temperature under vacuum. Imide groups were converted into amide moieties via solution cross-linking. Gas permeability decreased while gas selectivity increased as a function of cross-linking degree. Upon cross-linking, the concentration of larger N_2 penetrants in the permeate decreased; indicating that the constricted gas transport channels only permitted smaller gas penetrants like He and O_2 to pass through. Polyimide membranes have also been solution cross-linked using other forms of diamines e.g. 1,3-cyclohexanebis (methylamine) (CHBA) [63], ethylenediamine (EDA), 1,3-propane diamine (PDA), and 1,2-butane diamine (BuDa) [56], dendrimers [64], and polymers [65]. Low et al. demonstrated that the immersion of polyimide membranes into methanol solutions comprising diamines results in simultaneous occurrence of chemical grafts, cross-links and etching on polyimide membranes i.e. a solution phase modification [57].

2.2.3 Rubbery polymers for gas separation

As glass transition occurs when free-volume is created to permit a number of polymer chains to move together as a unit in the presence of sufficient vibrational (thermal) energy in the polymeric matrix, low T_g (< 0 °C) materials are usually soft and flexible at ambient temperatures i.e. rubbery materials [66]. Classic examples of rubbery materials that are commonly used as gas separation membranes are polydimethylsiloxane (PDMS) and polyethylene oxide (PEO).

PDMS is a polymer with unique properties owing to the inorganic siloxane backbone and organic methyl groups attached to the silicon. The fundamental structural properties of PDMS include low intermolecular forces between the methyl groups, unique flexibility in the siloxane backbone and high bonding energy of the siloxane bond, in particular to acidic gases. Such properties attribute to high gas permeabilities, and high selectivities for condensable gases in PDMS membranes [67]. Prior to using PDMS as membranes, cross-linking must be carried out first [38]. Merkel et al. reported the gas sorption, diffusion and permeation properties of cross-linked PDMS [38]. Gas permeabilities of fluorinated gases in PDMS are approximately an order of magnitude lower than those of their hydrocarbon analogs. This is primarily due to the lower solubility and diffusivity coefficients of perfluorinated carbons in PDMS [38]. Besides using cross-linked PDMS for gas separation membranes, PDMS-based

membranes can also exist in the forms of nanocomposites [68], block copolymers [69], and coatings [70-72].

Kim et al. fabricated a gas separation membrane consisting of single-walled carbon nanotubes embedded in a poly (imide siloxane) copolymer [68]. The poly (imide siloxane) component was synthesized using an aromatic dianhydride and diamine, and amine-terminated PDMS. The purpose of PDMS in this membrane was to facilitate good adherence of the polymer matrix to the carbon nanotubes. Park et al. used a sol-gel reaction to synthesize a imide-siloxane block copolymer/silica hybrid membrane that displayed increasing He, CO_2, O_2 and N_2 gas permeabilities with increasing PDMS content [69]. The increase in siloxane content in these membranes retarded the decrease in gas selectivities at an elevated temperature while plasticization of the organic matrix was restricted. Dal-Cin et al. applied PDMS as a caulking layer to alleviate structural defects in a polyetherimide-polyethylene glycol interpenetrating network (PEI-PEG-IPN) membrane [73]. Owing to its high gas diffusivities, PDMS is an ideal choice as a caulking material as it does not hinder the intrinsic gas transportation and consequently gas separation capabilities of the membrane material.

Polyethylene oxide (PEO) is polyethylene with high concentrations of polar ether oxygens separating each pair of carbon atoms. Polar ether oxygen

moieties are thought to be the only polar moieties that can improve CO_2/H_2 selectivity [74]. This is attributed to the dipole-quadrapole interaction between the polar ether oxygen (EO) units and the acidic CO_2 [24, 74, 75]. The CO_2-affinity of the ether oxygen moiety depend on the nature of the monomeric unit, polymerization degree, end group effect and ether oxygen concentration [76]. For example, EO units in the propylene oxide analog are more CO_2-philic than its counterparts in the form of ethylene oxide and THF [76]. The CO_2-affinity properties of polyether-based polymers can be tuned via modifications to the entropy and enthalpy of mixing. The entropy of mixing of a chain molecule increases with chain flexibility while the enthalpy of mixing is dependent on the number and strength of solute-solute, solvent-solvent, and solute-solvent interactions. Solute-solute and solvent-solvent interactions must be weak while solute-solvent interactions must be strong to favor CO_2 mixing. With low steric factors and glass transition temperatures, PEO is one of the candidates for CO_2-philic rubbery membranes.

The CO_2 permeability of semi-crystalline PEO can reach 12 Barrer and a CO_2/H_2 selectivity of 6.7 while the estimated CO_2 permeability and CO_2/H_2 selectivity of amorphous PEO is expected to be 143 Barrer and 7, respectively [77]. Polymer crystallinity reduces chain molecule flexibility and solute-solvent interactions that consequently reduce CO_2 permeability. Using photochemical reactions, Lin et al. cross-linked low molecular weight PEO-based acrylates to

fabricate rubbery membranes with low crystallinity [24, 74, 75]. CO_2 permeability of these rubbery membranes reached 400 Barrer while achieving a CO_2/H_2 selectivity of 30 at -20 °C. These highly amorphous membranes are considered to be state-of-the-art CO_2/H_2 selective membranes.

2.2.4 Modifications of rubbery polymer membranes

Besides cross-linking low molecular weight PEO-based monomers to form rubbery membranes [78-80], other alternatives include the synthesis of PEO copolymers [81-85], physical blends of PEO-based additives into membranes [23, 86, 87], and integration of nanoparticles into PEO-based polymers via chemical bonds [25, 88, 89].

Common PEO-copolymers that are frequently studied in other works consist of hard and soft segments. Hard segments can comprise of polyamides, polyimides or other glassy polymers e.g. poly(butylene-terephthalate) (PBT). A commercially known polyamide-PEO block copolymer is Pebax® MH 1657 (poly(amide-b-ethylene oxide)). Car et al. reported that the CO_2 permeability of this commercial PEO-based copolymer reached 73 Barrer with a CO_2/H_2 selectivity of 9.1 [86]. The CO_2 transport properties of Pebax® can be described using the solution-diffusion model [90]. In another work, Car studied PEO-PBT block copolymers also commercially known as Polyactive that possessed CO_2 permeabilities reaching up to 120 Barrer while achieving a CO_2/H_2 selectivity of

11 [81]. The CO_2 permeabilities of these PEO-based copolymers were enhanced by blending low molecular weight PEG additives [23, 81]. Membranes containing physically blended low molecular weight PEG additives are unsuitable for industrial gas separation applications as the presence of water causes leaching i.e. removal of these PEG additives.

Mixed-matrix PEO-based membranes can overcome the shortcomings of physically blended materials. Patel et al. reported that the incorporation of functionalized fumed silica (FS) nanoparticles (up to 14 nm in diameter) reduced CO_2 permeability while improving CO_2/light gas selectivity [88]. The chemically bonded FS nanoparticles reduced chain mobility and subsequently penetrant diffusivity. However, as the chain length of the PEO-based oligomer increased, penetrant diffusivity and solubility increased. Consequently, CO_2 permeability increased as well. Wilder et al. cross-linked PEG with dibenzylidene sorbitol, a low molecular weight organic molecule [91] while Mu et al. fabricated interpenetrating networks (IPNs) consisting of poly (ethylene oxide) and polyhedral oligomeric silsesquioxane (POSS) nanoparticles [92]. Although the gas permeation and separation properties of these nanohybrid materials are not reported in these works, the reported physic-thermal and rheological properties of these nanomaterials are aptly suitable for gas separation. Mixed matrix membranes can also be fabricated using catalyzed sol-gel processes using low to mid-range molecular weight organic monomers and inorganic molecules [29,

93-95]. The gas separation properties of these organic-inorganic materials can be tailored by tuning synthesis conditions [96-98].

2.3 Summary on membrane technology

CO_2 separation using polymeric membranes can be achieved using glassy or rubbery materials. Material modifications are cost-effective methods to enhance the gas separation and transportation properties of currently known membrane materials. Depending on application, glassy and rubbery materials can be utilized to separate CO_2 from light gases while achieving purification purposes. In this work, the use of both materials for CO_2 separation is explored. A glassy material is modified using a novel vapor modification technique. The industrial applicability of this approach is also highlighted. Rubbery materials are studied in the form a nanocomposite that consists of CO_2-philic organic and inorganic components. Using a straightforward sol-gel chemistry technique, organic-inorganic materials are first fabricated, followed by a modification via an ozone treatment. Material modifications yield promising CO_2 separation results in both classes of materials.

CHAPTER THREE:

EXPERIMENTAL METHODS FOR MEMBRANE CHARACTERIZATION

3.1 Field emission scanning electron microscopy (FESEM)

The morphology of hollow fiber membranes was observed using a field emission scanning electron microscope (FESEM JEOL JSM-6700LV). An operating voltage of 15 kV and a capture angle of 90° were used. The hollow fibers were immersed and fractured in liquid nitrogen; and coated with a thin layer of platinum using a current of 30 mA over a period of 10-30 seconds prior to FESEM.

3.2 High resolution transmission electron microscopy (HRTEM) & scanning transmission electron microscopy (STEM)

HRTEM and STEM were used to characterize organic-inorganic materials. To prepare the samples for these characterizations, solutions containing 2 wt.% of organic-inorganic materials or nanohybrid materials were diluted to 0.01 wt. %. Subsequently, the diluted solution was pipetted onto a copper grid and allowed to dry (solvent removal). HRTEM was done using a JEOL HRTEM 3010 with an operating current of 113 μA and an accelerating voltage of 40 keV. The high-angle annular dark field scanning-TEM (HAADF-STEM) studies and EDX analysis were carried out on a FEI Titan 80-300 electron microscope that was equipped with an electron beam monochromator, an energy dispersive X-ray spectroscopy (EDX) and a Gatan electron energy loss spectrometer. The accelerating voltage of the electron beam was 200KeV. The scanning electron beam size of EDX measurement was around 0.3 nm.

As the HAADF operation principle relies on atomic number (Z)- contrast imaging, HAADF images show little or no diffraction effects while the brightness intensity of these images is approximately proportional to Z^2 [34]. Hence, the bright shapes in STEM tomographs comprise of elements with a large Z number i.e. inorganic elements in contrast to those in the organic polymer matrix. Additionally, the intensity of these bright shapes is also related to the concentration of inorganic elements.

3.3 Fourier transform infra-red spectroscopy (FTIR)

A Perkin Elmer Fourier transform infrared (FT-IR) spectrometer (Spectrum 2000) was used to characterize changes in the chemical structure of the working materials. Prior to measurements, the spectrometer was purged with nitrogen gas for 30 minutes. After placing a sample into the FT-IR spectrometer, the system was purged with nitrogen gas for another 30 minutes. FTIR measurements in the attenuated total reflectance (ATR) mode were performed over 64 scans in the range of 400 to 4000 cm^{-1}. The resolutions of the spectra were 4 cm^{-1}. The data was analyzed using Spectrum Version 5.3 (analytical software).

3.4 Solid state nuclear magnetic resonance spectroscopy (NMR)

The chemical structures of the organic-inorganic materials were characterized using solid-state ^{29}Si and ^{13}C NMR. The ^{29}Si (79.5 MHz) and ^{13}C (100.6 MHz) NMR with magic angle spinning (MAS) at 7.5 kHz was performed with a Bruker DRX 400 spectrometer. Samples were ground prior to analysis.

3.5 X-ray photoelectron spectroscopy (XPS)

X-ray photoelectron spectroscopy (XPS) measurements were performed using a Thermo Fisher Scientific Theta probe XPS spectrometer with monochromatic Al Kα (E= 1486.6 eV) radiation. The X-ray source was operated at 15 kV and 100 watt. The spectra were first recorded in the fixed analyzer transmission mode of the electron energy analyzer (pass energy = 200 eV). For high resolution scans of peaks of interest, a pass energy of 40 eV was used. The pressure in the chamber was about 5×10^{-10} mbar. The photoelectron take-off angle of 50° was applied. The binding energies were referenced to C 1s peak at 285.0 eV. The raw data was quantified and analyzed using Thermo Avantage 4.12 software.

3.6 Differential scanning calorimetry spectroscopy (DSC)

Differential scanning calorimetry (DSC) was performed using a DSC822^{e} (Mettler Toledo) calorimeter. The temperature range was from –100 °C to 100 °C with a heating rate of 10 °C/minute in a N_2 environment. The raw DSC data

was processed using the S**TA**R^{e} evaluation software from Mettler Toledo. The second heating curve was used for the analysis of organic-inorganic materials. The polymer crystallinity in these hybrid materials was derived using the following equation:

$$\text{Crystallinity (\%)} = \Delta H_f / (\chi_p \times \Delta H^0_f) \times 100\% \qquad \textbf{Equation 3.1}$$

whereby ΔH_f is the apparent heat of fusion per gram of the materials, ΔH^0_f is the thermodynamic heat of fusion per gram of a perfect PEO crystal with the value of 188.9 J/g [99] and χ_p is the weight percentage of PEO in the nanohybrid membranes.

3.7 Bulk positron annihilation lifetime spectroscopy (PALS)

PALS was used to characterize the relative fractional free volume content (FFV) in the organic-inorganic membranes. To prepare the nanohybrid samples for PALS characterization, a positron source (diluted from a ^{22}NaCl purchased from DuPont Pharmaceutical Division, Delaware) was sandwiched in between two pieces of the membrane samples (1 cm x 1 cm), which was sealed in between two 12 μm thick Kapton films. The assembled samples were exposed to different temperatures and CO_2 pressures in a specially designed set-up that was described in references [100, 101]. CO_2 pressure in this set-up was monitored using an Omega transducer pressure gauge (Model 302-1KGY). The

positron annihilation lifetime (PAL) spectra were recorded using a fast-fast coincident PAL spectrometer (resolution = 280 ps) at the University of Missouri-Kansas City. The acquired PAL spectra (1 million counts) were analyzed into 3-mean lifetimes and also into lifetime distributions using PATFIT and MELT computer programs. The longest lifetime from these analyses (τ_3 in ns) is due to the pick off annihilation of ortho-positroniums (*o*-Ps) in free volume cavities (V_f). The V_f mean radius and volume were tabulated using well-established semi empirical equations based on the spherical infinite potential-well model [102-104].

3.8 Slow-beam positron annihilation lifetime spectroscopy (PALS)

Slow-beam PALS was conducted using a slow-positron beam setup in the National University of Singapore. **Figure 3.1** shows the basic design of the slow-positron beam setup in NUS. The vacuum in the sample chamber was about 10^{-6} torr at room temperature. The PALS spectra were recorded at two well-defined positron energies of 1 keV and 5 keV. The slow positrons were generated from a 50 mCi ^{22}Na source, moderated by tungsten foils and electromagnetically transported to the organic-inorganic materials. The spectra were detected and recorded by a BaF_2 crystal scintillator at a counting rate of about 150 cps. The acquired PAL spectra (1 million counts) were analyzed into 3-mean lifetimes and into lifetime distributions using PATFIT and MELT computer programs. The longest lifetime from these analyses (τ_3 in ns) is due

to the pick off annihilation of ortho-positroniums (*o*-Ps) in free volume cavities (V_f). The V_f mean radius and volume were tabulated using well-established semi-empirical equations based on the spherical infinite potential-well model [102-104]. In this dissertation, only the values obtained from MELT are reported.

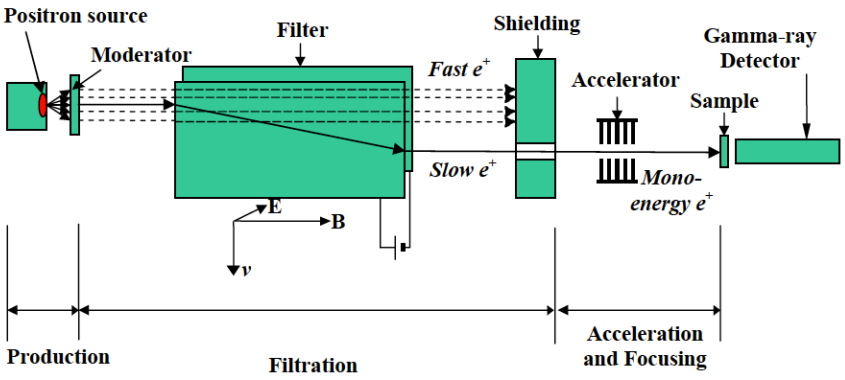

Figure 3.1 The basic setup of the slow-positron beam in NUS.

3.9 Gas transportation and separation capabilities

3.9.1 Pure gas permeability of dense flat sheet membranes

The pure gas permeabilities were determined using a constant volume and variable pressure method. **Figure 3.2** shows a schematic of the gas permeation cell used in this work. The diffusion cell was separated into two compartments by the sample membrane film. Before measuring the gas transport properties, the system was kept under a constant vacuum for 24 hours to remove residual air or other gases. Contact between the gas penetrant and the membrane is made via upstream. The upstream pressure, p_2, was kept

constant at 3.5 atm in the input chamber, while increments in the downstream pressure, p_1, in the permeation chamber was monitored using a MKS Baratron pressure transducer. At steady state, the pressure increments were linear with time *t*. The H_2 and CO_2 permeability at 3.5 atm were determined from **Equation 3.2**:

$$P = D \times S = \frac{273 \times 10^{10}}{760} \frac{VL}{AT[\frac{p_2 \times 76}{14.7}]} (\frac{dp}{dt}) \qquad \text{Equation 3.2}$$

where *P* is the permeability of a membrane to a gas and its unit is in Barrer (1 Barrer = 1 × 10^{-10} cm^3 (STP)-cm/cm^2 sec cmHg) [32, 33], *dp*/*dt* is the downstream pressure build-up rate when permeation reached a steady state, *D* is the average effective diffusivity (cm^2/s), S is the apparent sorption coefficient/solubility (cm^3 (STP)/cm^3 polymer cmHg), V is the volume of the downstream chamber (cm^3), L is the film thickness (cm). *A* refers to the effective area of the membrane (cm^2), T is the experimental temperature (K) and the pressure of the feed gas in the upstream chamber is given by p_2 (psia).

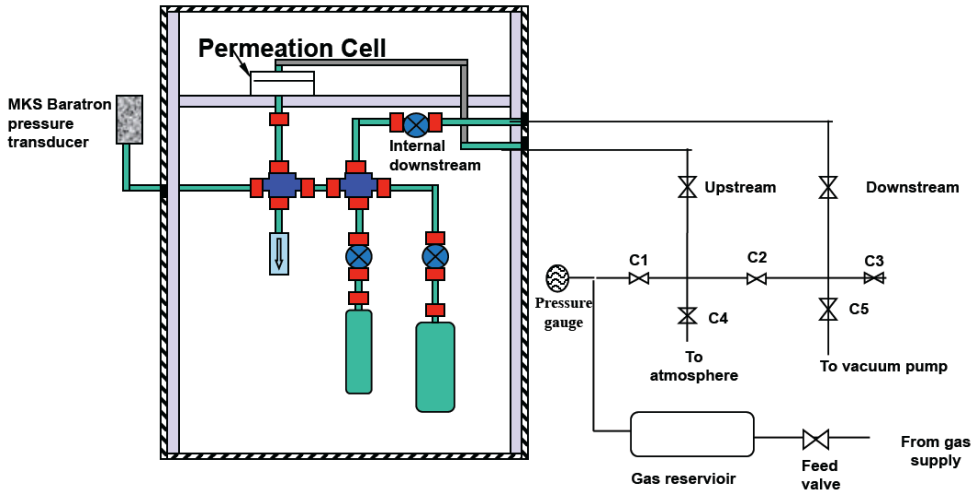

Figure 3.2 A schematic of the gas permeation cell that was used to characterize pure gas transport properties of working materials in this work [105].

The ideal separation factor of a membrane for gas A to gas B, which was a product of diffusivity selectivity and solubility selectivity, was evaluated as follows:

$$\alpha_{A/B} = \frac{P_A}{P_B} = \frac{D_A}{D_B} \times \frac{D_A}{D_B}$$ Equation 3.3

3.9.2 Pure gas permeance of dual layer hollow fiber membranes

The H_2 and CO_2 permeance of pristine and modified hollow fibers were characterized using a variable-pressure constant-volume gas permeation cell. The permeation cell set-up that was described previously in Section 3.9.1 was modified to measure the gas permeance of hollow fibers assembled in a test

module. Each module consisted of 2 or more fibers with an effective length of approximately 7.5 cm. In the upstream side, fibers were sealed at the end with fast curing epoxy. Hence, allowing gas to permeate into the membrane from the feed side only. The upstream pressure was 20 psig and the operating temperature was 35 °C. The permeance (P/L) of each fiber was determined using **Equation 3.4**:

$$\frac{P}{L} = \frac{273 \times 10^{10}}{760} \frac{V}{AT[p_o \times 76/14.7]} \left[\frac{dp}{dt}\right] \qquad \text{Equation 3.4}$$

whereby *P* is the permeability of the separating layer (Barrer); *L* is the thickness of the apparent dense-selective layer (cm); *V* the volume of the permeation side (cm^3); *A* is the effective separating area of the membrane (cm^2); T is the operating temperature of the permeation cell (K); dp/dt is the rate of pressure increase at steady state as a function of time (mmHg/s) and p_o is the gas pressure difference across the membrane (cmHg). The unit of the permeance is GPU (1 GPU = 1x 10^{-6} cm^3(STP)/cm^2s cmHg). The ideal separation factor, $\alpha_{A/B}$, can be determined from **Equation 3.5**:

$$\alpha_{A/B} = \frac{(P/L)_A}{(P/L)_B} \qquad \text{Equation 3.5}$$

3.9.3 Mixed gas permeability of dense flat sheet membrane

A schematic of the mixed gas test setup is shown in **Figure 3.3**. Mixed gas mixtures were used as the feed gas and the measurements were conducted at 35 °C with a CO_2 partial pressure of 3.5 atm. The sampling process was initiated by evacuating the line from the receiving volume (the lower chamber: downstream) to a gas chromatograph (GC) by vacuum. The compositions of the feed and permeate were analyzed by gas chromatography. Similar to the pure gas permeability, the mixed gas steady state permeation rate were then determined by Equations 3.6 and 3.7:

$$P_{H_2} = \frac{273 \times 10^{10}}{760} \frac{(1 - y_{CO_2})VL}{AT(76/14.7)[(1 - \chi_{CO_2})p_2]} \times \left(\frac{dp_1}{dt}\right) \qquad \text{Equation 3.6}$$

$$P_{CO_2} = \frac{273 \times 10^{10}}{760} \frac{y_{CO_2} VL}{AT(76/14.7)(\chi_{CO_2} p_2)} \times \left(\frac{dp_1}{dt}\right) \qquad \text{Equation 3.7}$$

where P_{CO_2} and P_{H_2} are respectively the gas permeability of CO_2 and H_2 (Barrer), p_2 is the upstream feed gas pressure (psia), p_1 is the downstream permeate gas pressure (psia), x_{CO_2} is the molar fraction of CO_2 in the feed gas (%) and y_{CO_2} is the molar fraction of CO_2 in the permeate (%), V is the volume of the downstream chamber (cm^3), L is the film thickness (cm). Subsequently,

the separation factor of mixed gas can be simplified into the calculating equation as described in Equation 3.5 due to the negligible downstream pressure. The mixed gases consisted 20, 50, 80, 70 and 90 mol.% of H_2 in CO_2.

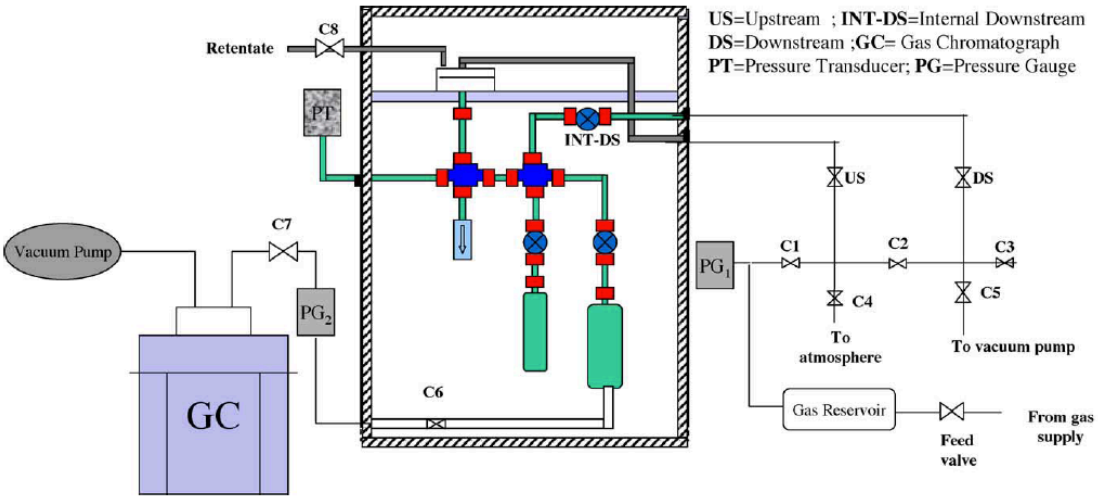

Figure 3.3 The mixed gas test set-up used in this work [106].

3.10 Gas sorption

Carbon dioxide sorption tests were conducted using a Cahn D200 microbalance sorption cell at 35 °C over a pressure range of 0-250 psi (0-17.24 bar). **Figure 3.4** shows a schematic of the microbalance sorption cell used in this work. For each sample, films with thickness of 300 μm, sides of 1 cm, and total mass of approximately 80-100 mg were placed on the sample pan. The system was evacuated for 24 hours prior to testing. The gas at a specific pressure was fed into the system. The mass of the sorbed gas in the membranes at equilibrium was recorded. Subsequent sorption experiments were performed at increased

gas pressures. The buoyancy force corrected the equilibrium sorption value obtained. CO_2 solubility coefficients of each sample were obtained from the gradient of the sorption isotherms. Subsequently, CO_2 diffusivity coefficients were calculated using Equation 3.2.

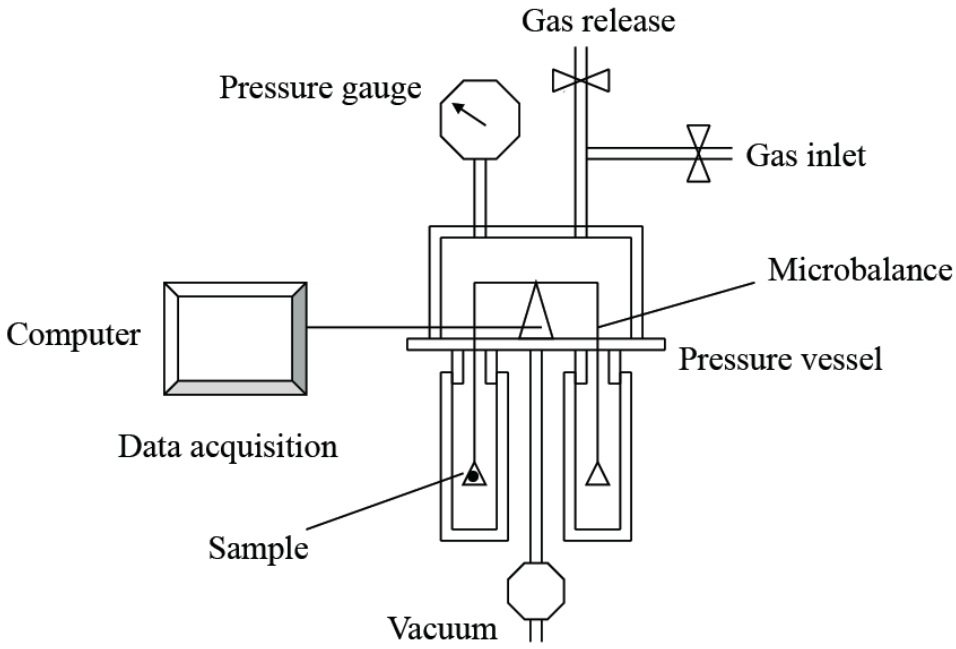

Figure 3.4 A schematic of the microbalance sorption cell.

CHAPTER FOUR:

A STRATEGY FOR SURFACE MODIFICATION OF POLYIMIDE MEMBRANES BY VAPOR PHASE ETHYLENEDIAMINE (EDA) FOR HYDROGEN PURIFICATION

4.1 Introduction – The need for polyimide modification

CO_2 removal from syngas (H_2) streams can be achieved using "H_2 selective" [19, 22, 51, 57] or "CO_2 selective" membranes [24, 25, 29]. This chapter focuses on H_2-selective membranes that are suitable for energy production in power plants, which requires a H_2 purity of 70 - 80% at low pressures of approximately 5 bar. H_2-selective membranes are usually fabricated from glassy polymers like polyimides whereby gas separation is achieved by penetrant size variation [19].

Polyimides possess strong mechanical properties and superior chemical resistance at elevated temperatures; especially in harsh, chemical environments. Like most other polyimides, 6FDA-based polyimides suffer from poor intrinsic H_2/CO_2 selectivity [41] and CO_2 plasticization that further retards H_2/CO_2 separation [107]. To better capitalize on the advantages of 6FDA polyimides, chemical modifications of these glassy materials may improve the H_2/CO_2 separation characteristics and suppress CO_2-induced plasticization.

Extensive research on post-treatment modifications of 6FDA-based polyimide gas separation membranes has previously been done [22, 41, 51, 55, 107, 108]. Traditionally, a polyimide gas separation membrane is modified via a post-treatment cross-linking technique that is facilitated by the immersion of polyimide membranes in diamine/alcohol solutions [41, 51, 53, 64, 106, 109].

The modification results in the formation of amide groups through a favorable cleavage of an imide ring by the NH_2 groups of amine-containing compounds [53, 57, 110]. However, a limitation of this solution phase modification technique is methanol swelling that may inevitably induce some degrees of undesirable alteration to the polymeric structure [55], especially for asymmetric membranes with an ultrathin selective skin. In addition, there is a lack of re-usability of the cross-linking solutions due to the likely contamination after use and considerable time is required to dry solution cross-linked membranes. These factors render the method of solution-phase modification unsuitable for large-scale membrane modification.

Meanwhile, vapor modification has been widely used in various applications [111-114]; and can potentially be a cost-effective technique to modify membrane materials for improving targeted gas separation properties while overcoming the effects of solvent swelling in gas separation membranes. Although this technique has not been applied in membrane modification prior to this work, solvent vapors are known to achieve desirable results in applications ranging from surface modification [111] to nanowire alignment [112] to polymer chain alignment [113]. For example, Piwoński and Ilink functionalized titania surfaces using a series of fluoroalkylsilane vapor [111]. Ryu and Park used aniline vapor to vertically align nanowires of self-assembled peptides [112], while Lu et al. applied solvent vapor to treat and orientate poly (3-

butylthiophene) (P3BT) backbones as an advanced fabrication approach for new semiconducting materials [113]. Voicu et al. used solvent vapor to induce polymer swelling during nanoimprint lithography to obtain operation flexibility [114]. To effectively use vapor-phase modification to enhance gas selectivity in gas separation membranes, the pairing of appropriate cross-linking reagents with specific membrane materials must be carefully designed. In this chapter, a 6FDA-based polyimide dense film membrane was chosen to demonstrate the viability of the vapor-phase modification method using ethylenediamine (EDA). Although flat sheet membranes are usually confined to lab-scale research, membranes of such a physical configuration demonstrate the gas transport and separation properties of a membrane material, prior to possible commercialization.

4.2 Materials and Experimental details

4.2.1 Materials

The ethylenediamine (EDA) was purchased from Aldrich, Singapore and used as received. The 6FDA-durene polyimide was synthesized using the chemical imidization synthesis procedure deployed by Chung et al. [40]. 2,2-bis(3,4-carboxylphenyl)hexafluoropropane dianhydride (6FDA) was purified via sublimation, while 1,2,4,5-tetramethylbenzene (durene) diamine was recrystallized from methanol. N-methyl-pyrrolidone (NMP) was first dried with molecular sieves and distilled at 42 ºC and 1 mbar. The durene diamine was dissolved in NMP via magnetic stirring at room temperature. Subsequently, stoichiometric amounts of 6FDA was added to the diamine solution and stirred magnetically in a nitrogen environment at 25 ºC. After 24 hours of reaction, acetic anhydride and triethylamine (4:1 molar ratio) were slowly added to the solution to perform imidization for 24 hours. Subsequently, the polymers were precipitated in methanol, filtered and dried at 150 ºC for 24 hours.

4.2.2 Dense film membrane preparation

A pre-determined amount of 6FDA-durene polyimide was dissolved in dichloromethane to yield a 2% (w/v) polymer solution that was cast on a silicon wafer at 25 °C. Upon controlled evaporation of the 6FDA-durene/dichloromethane solutions, the nascent films were dried in vacuum at

250 °C for 24 hours to remove the residual solvent. Polyimide films with thickness of 50 ± 5 μm were chosen for further vapor phase modification. The 6FDA-durene polyimide chemical structure is shown in **Figure 4.1**.

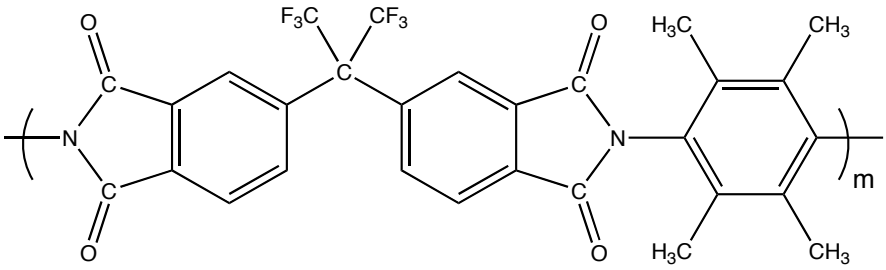

Figure 4.1 Chemical structure of 6FDA-durene polyimide

4.2.3 Vapor-phase EDA modification on dense film membranes

Vapor-phase EDA modification was carried out in a homemade container as shown in **Figure 4.2**. Pre-determined amounts of EDA in the covered containment were stabilized after 30 minutes at 25 °C. Thereafter, 6FDA-durene membranes were quickly exposed to the vapor-phase EDA environment. There was no contact between the 6FDA-durene polyimide membranes with the EDA solution. In this work, 6FDA-durene membranes were exposed to EDA vapor for 1, 2, 5, 10, and 30 minutes. To remove residual EDA, the vapor modified 6FDA-durene membranes were then washed with deionized water immediately upon removal from the containment. Subsequently, these modified membranes were annealed at 70 °C for about 1 day to ensure a complete reaction.

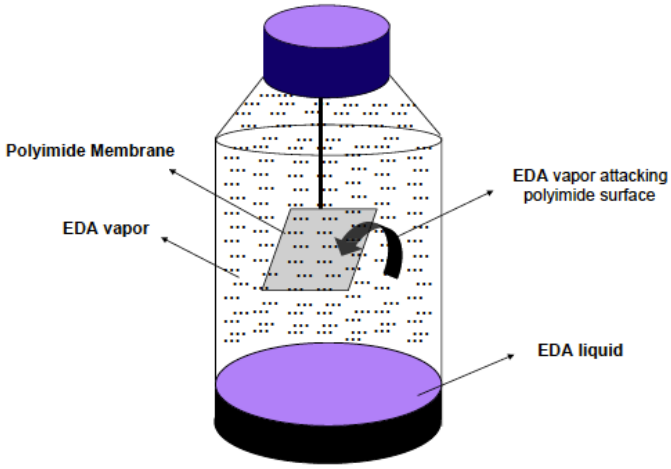

Figure 4.2 Experimental set-up for the vapor-phase modification process of flat sheet membranes.

4.2.4 Membrane characterization

FTIR (ATR mode) spectroscopy and x-ray photoelectron spectroscopy (XPS) was used to characterize the imide conversion process. XRD was used to quantitatively measure the ordered dimension and inter-chain spacing of polyimide membranes at room temperature. The gel content of these vapor-phase modified polyimide membranes was measured by extracting the films in dichloromethane for 24 hours. The insoluble fractions were vacuum dried at 120 °C for about 1 day. The weight of these polyimide films before and after extraction were measured and the gel content was calculated by the following equation:

$$\%\ \text{Gel content} = \frac{W_1}{W_0} \times 100\% \qquad \textbf{Equation 4.1}$$

where W_1 and W_0 are the insoluble fraction weight and original weight of the cross-linked polymer films, respectively. The pure and mixed gas permeability of these vapor-phase modified membranes were characterized using the experimental procedures detailed in Chapter 3. The mixed gas used to characterize these membranes comprised 50 mol.% of H_2 in CO_2. Prior to mixed gas permeation test characterizations, the vapor-phase modified membranes were conditioned at 35 ˚C with a CO_2 partial pressure of 3.5 atm for at least 3 days.

4.3 Results and discussion

4.3.1 Physicochemical characterizations of membranes

Based on calculations using the Antoine equation – **Equation 4.2** [115], the vapor pressure of EDA at 25 °C is 11.99mm of Hg and the air in the covered containment consists of 1.577 % v/v EDA vapor.

$$\log_{10} p = A - \frac{B}{C + T} \qquad \text{Equation 4.2}$$

where p is the vapor pressure, T is temperature and A, B, and C are component-specific constants. For EDA, A = 4.22, B = 1302.26 and C = -81.79 when T = 299 – 390 °K [116].

The chemical structure of the EDA vapor modified polyimide membranes was determined using FTIR-ATR. **Figure 4.3** shows the ATR-FTIR spectra of these EDA-vapor modified materials. Bands indicating the C=O asymmetric stretch of imide groups (1785 cm^{-1}), C=O symmetric stretch of imide groups (1718 cm^{-1}) and C–N stretch of imide groups (1352 cm^{-1}) belong to the original polyimide [117]. Upon EDA vapor modification, new bands are formed due to the presence of CONH groups; a C=O stretch band, a N–H bend and a C–N stretch appearing at around 1644 cm^{-1}, 1617 cm^{-1}, and 1520 cm^{-1}, respectively.

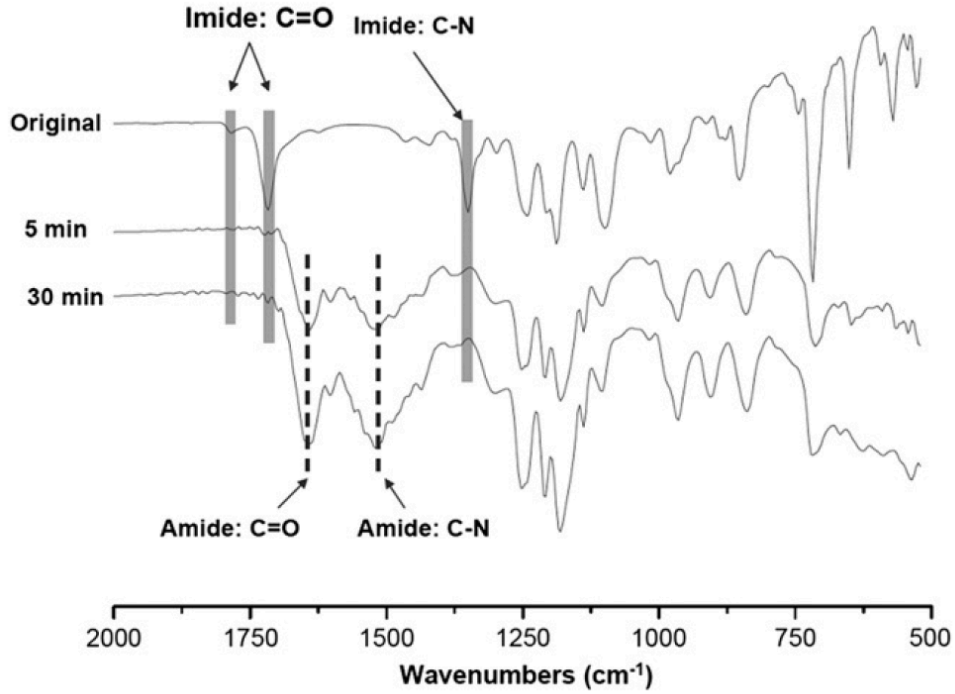

Figure 4.3 ATR-FTIR analyses of the original and EDA vapor-phase modified 6FDA-durene polyimides.

Based on the FTIR-ATR results, **Figure 4.4** describes the chemical reaction mechanism occurred during vapor-phase modification. The main chemical reaction during this process is the conversion of imide groups in polyimides into amide groups alongside simultaneous cross-linking between polymer chains due to the strong nucleophilicity of EDA [56]. Although the current new strategy utilizes EDA vapor, the chemical reaction between the diamines and the polyimides is similar to those observed in other works [51, 53, 55, 57, 64, 106, 109, 110].

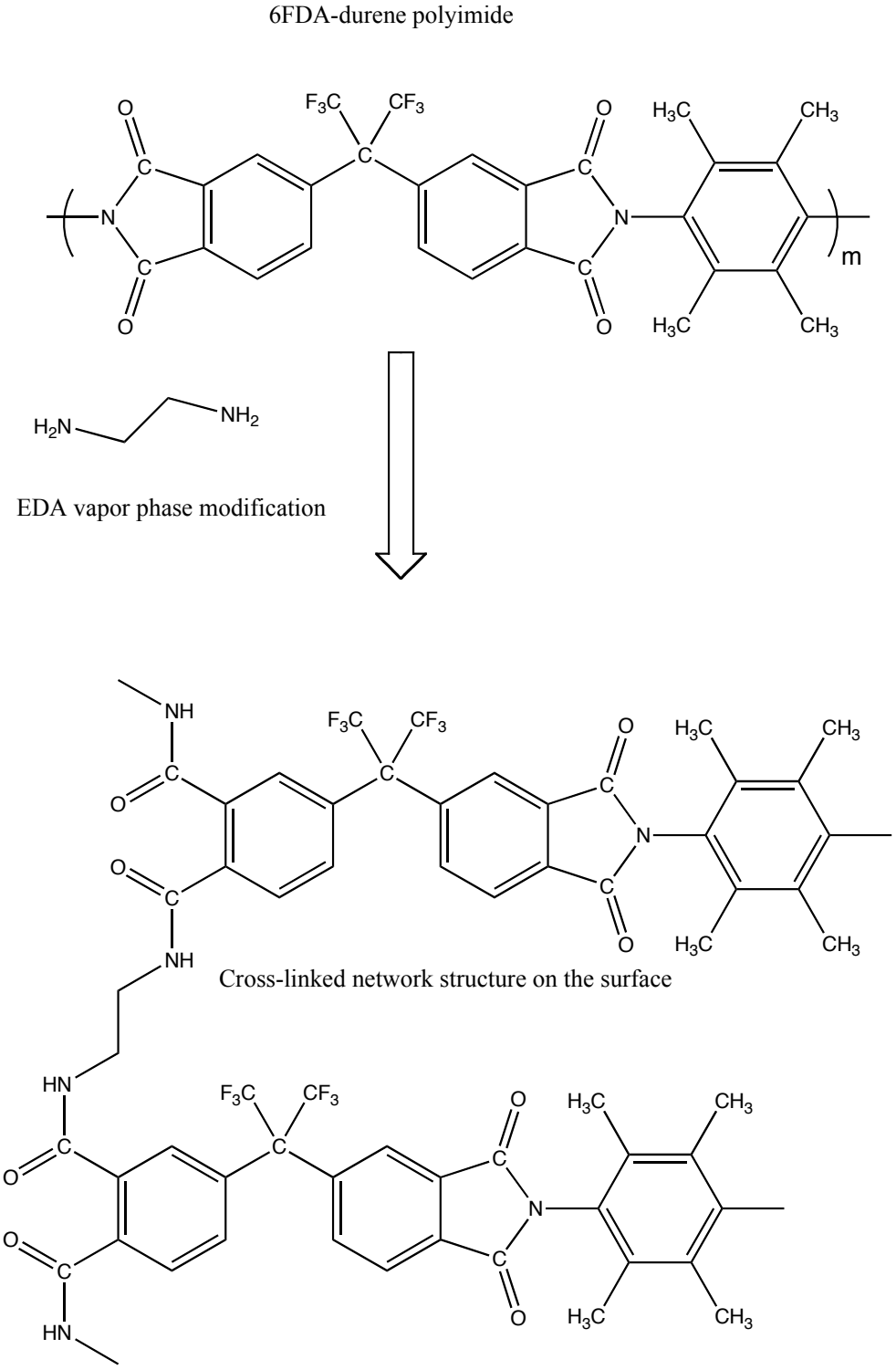

Figure 4.4 Reaction mechanism of vapor-phase EDA modification on the surface of 6FDA-durene membranes.

By comparing the elemental composition differences before and after EDA vapor treatment, the XPS results also validate the chemical modification of imides to amides. The fluorine content in the membranes should remain unaffected (due to non-reactivity between - CF_3 moieties and amines) while the nitrogen content should be increased by the vapor-phase EDA modification. Hence, the nitrogen to fluorine (N/F) ratio can be used to quantify this chemical reaction. After EDA vapor modification, the N/F ratio increases significantly from 0.31 (original) to 0.83 (5-min of EDA-vapor modification). Coupled with the enriched nitrogen content, the shift in FTIR spectra validates the effectiveness of the vapor-phase surface modification of polyimide membranes using vapor-phase EDA.

The d-space of the polyimide membranes before and after EDA vapor modification was examined using XRD. **Figure 4.5** shows that a decrease in d-space from 6.18 Å of the original polyimide membrane to around 6.02 Å of the EDA-vapor modified polyimide membranes was observed. The cross-linked structures in Figure 4.4 may alter chain-packing that subsequently reduces the d-space. These findings indicate a tighter microstructure in EDA vapor-modified polyimide membranes. The effects of altered chemical structures and physicochemical changes in vapor-modified polyimide membranes on the H_2/CO_2 separation performances are discussed in the following section.

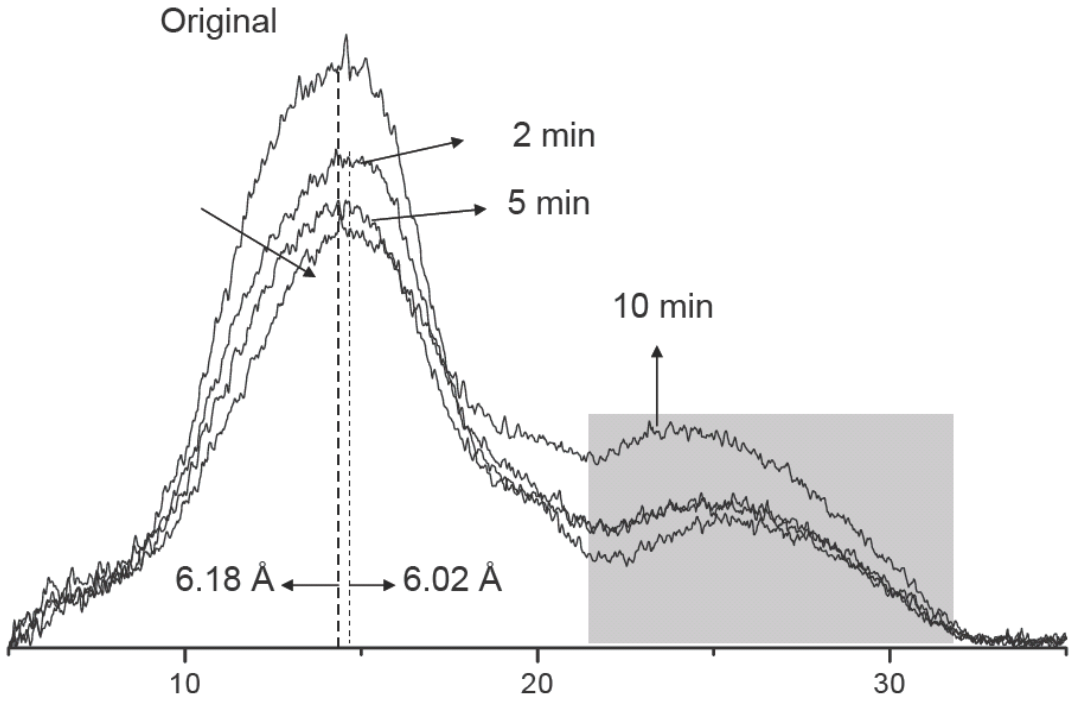

Figure 4.5 XRD spectra of vapor-phase modified 6FDA-durene membranes.

4.3.2 H_2 and CO_2 separation properties of vapor-phase EDA modified polyimide membranes

Due to the trade-off between H_2/CO_2 solubility selectivity and diffusivity selectivity, the separation of H_2 and CO_2 is challenging while H_2/CO_2 selectivity of most H_2-selective polymeric membranes is usually less than 10 [19]. The trade-off between solubility and diffusivity selectivity is ascribed to the difference in molecular size (H_2 (2.89 Å) vs. CO_2 (3.30 Å) in kinetic diameter) that favors H_2 transport and the higher solubility of carbon dioxide that favors CO_2 transport. These competing effects lead to low H_2/CO_2 permselectivity.

To evaluate the H_2/CO_2 selectivity of vapor-modified polyimide membranes,

pure gas tests were carried out in the initial stages and the results are demonstrated in **Figure 4.6**. As vapor-phase modification leads to cross-linking and the densification of polymer chains, the permeabilities of both H_2 and CO_2 continuously decrease with longer vapor-phase EDA treatments. However, the decrease in H_2 permeability is less than that of CO_2 permeability. With a tighter microstructure in vapor-phase modified polimide membranes, bigger-sized CO_2 molecules are predominantly prevented from permeating across the membrane while the small sized H_2 molecules continue to permeate across the membrane, albeit at slower rates. The significant increase in H_2/CO_2 selectivity from around 1 (original) to 102 (10 min EDA vapor modification) validates the aforementioned hypothesis. The significantly enhanced H_2/CO_2 separation performance of vapor-phase modified polyimide membranes can be subscribed to the reduction of CO_2 diffusive pathways as vapor-phase EDA modification transforms these membranes into barriers against CO_2 [56, 118].

Besides, the vapor-phase EDA modification strategy results in a higher H_2/CO_2 selectivity (around 37) compared with that (around 5) by the previous solution approach with 5 minutes of modification time [22], indicating a highly effective modification strategy. This phenomenon is due to (1) intensive EDA-vapor modification on the surface of polyimide membranes, (2) minimal solvent-induced swelling in the substructure as often occurred in the solution immersion method. In retrospect to previous studies on the solution modification of

polyimide membranes with various diamine/methanol solutions, the surface modification effects of propane-1,3- diamine (PDA) and butane-1,4-diamine (BuDA) should potentially further enhance H_2/CO_2 selectivity of polyimide membranes compared to EDA [22]. Therefore, further studies on the effects of various vapor-phase diamines are expected to yield much more impressive results.

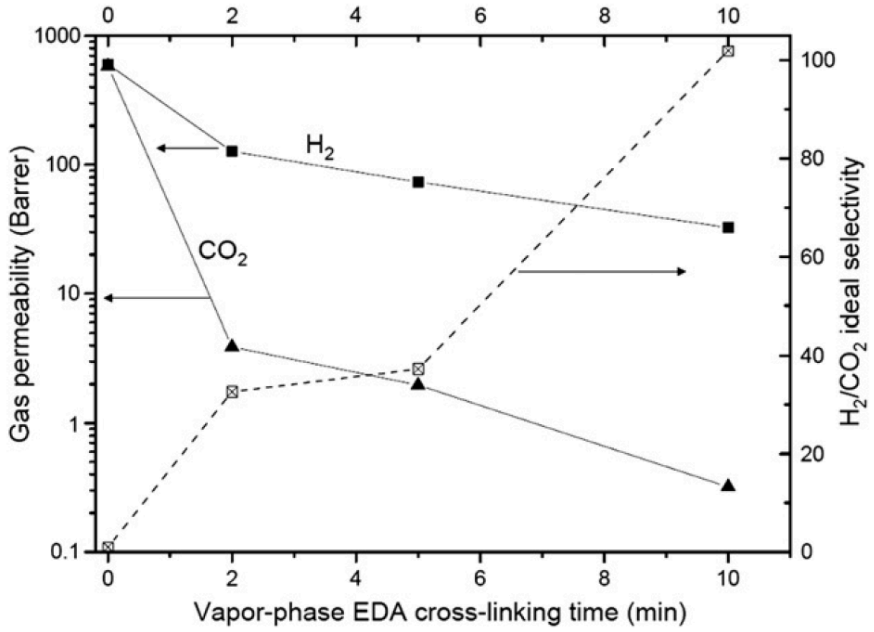

Figure 4.6 Effect of vapor-phase EDA modification time on H_2 and CO_2 separation performance of 6FDA-durene polyimide membranes.

As mentioned, one of the advantages of the vapor-phase EDA modification approach is its convenience to apply a highly effective surface-intensive modification on hollow fiber membranes. However, this surface-intensive modification (as shown in Figure 4.1) also induces structural heterogeneity in flat membranes. A three-layer structure (visualized in **Figure 4.7**) is thought to

exist in vapor-modified flat polyimide membranes. Hence, the intrinsic H_2/CO_2 separation properties of the vapor-phase modified layer in polyimide membranes cannot be estimated by simplistic pure gas permeation tests.

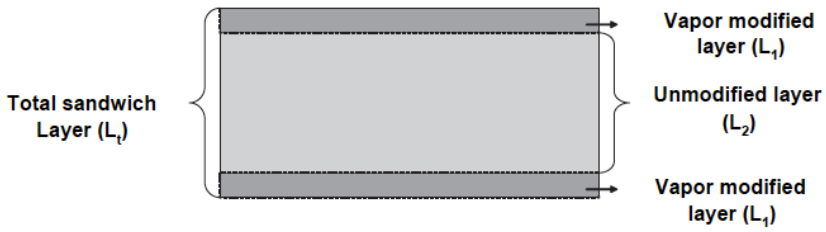

Figure 4.7 Schematic layer structure of vapor-phase EDA modified polyimide membranes

To determine the intrinsic H_2/CO_2 separation performance of the EDA-vapor cross-linked layer, the resistance model was applied and single-sided EDA-vapor modified membranes were prepared for predicting the true modified (cross-linked) layer of membranes. The procedure for the single-sided modification has been elaborated in details in Ref. [57]. According to the resistance model [119], the relationship between the EDA-vapor modified layer thickness (L1) and the permeability of the modified layer (P1) can be calculated using the following equation:

$$\frac{L_t}{P_t A_t} = \frac{L_1}{P_1 A_1} + \frac{L_2}{P_2 A_2} \qquad \textbf{Equation 4.3}$$

where P refers to the permeability, L refers to the thickness and A refers to the

effective membrane area. The subscripts 1 and 2 refer to the EDA-vapor modified and unmodified layers, respectively. T refers to the total/overall property. Equation 4.3 is further simplified by ensuring that the effective membrane area is the same i.e. $A_t = A_1 = A_2$.

The gel content of the vapor modified-side can be used to approximate the thickness of the EDA-vapor modified layer (L1). The L1 of a 6FDA-durene-polyimide membrane modified by 5 minutes of EDA vapor modification is 10.8 ± 0.9 μm. Using Equation 4.3, the intrinsic H_2 and CO_2 permeability of the vapor-phase EDA modified layer are calculated to be 40.1 and 1.02 Barrer, respectively; while achieving a H_2/CO_2 selectivity of 39.3. H_2 and CO_2 permeability in the EDA-vapor modified layer is lower than those of a 5-min EDA-vapor modified membrane that contains three layers (H_2: 73.4 Barrer; CO_2: 1.97 Barrer) as seen in Figure 4.6. However, the H_2/CO_2 selectivity in a vapor-phase EDA modified polyimide layer is slightly higher (39.3) when compared to a three-layered vapor modified polyimide membrane (37.3). These indicate a denser structure and enhanced H_2/CO_2 separation ability of the ‘‘real’’ cross-linked layer.

Furthermore, to meet the practical requirements of hydrogen purification, the mixed gas separation performance of the EDA-vapor modified polyimide membrane is evaluated by an equal molar (H_2 and CO_2) binary system. The

results of mixed gas test are shown in **Table 4.1**. For all polyimide membranes before and after EDA-vapor modification, the H_2 permeability in mixed gas tests is significantly lower than that in pure gas tests, which should be due to the slow CO_2 gases with higher condensability dominating the sorption site, thus reducing fast H_2 gas transport through the membranes.

Conversely, the CO_2 permeability in mixed gas tests is comparable to or higher than that in pure gas tests, which is attributed to the assisted CO_2 transport by the fast gas of H_2 [120-122]. Consequently, the interplay between a fast gas (H_2) and a slow gas (CO_2) lowers H_2/CO_2 selectivity in mixed gas tests compared with that in pure gas tests. However, comparing to other conventional polymers [19], the H_2/CO_2 selectivity of 16.6 for the 10-min EDA-vapor modified polyimide membrane in the mixed gas tests is still higher. Finally, the H_2/CO_2 separation performances before and after the vapor-phase EDA modification in both pure and mixed gas tests are compared with the Robeson's trade-off line [123] in **Figure 4.8**. From Figure 4.8, it is apparent that longer vapor-phase EDA treatment durations enhance the H_2/CO_2 separation performance of membranes. The dominant CO_2 sorption and the enhanced CO_2 transport by the ''fast'' gas of H_2 lowers the H_2/CO_2 separation performance in mixed gas tests when compared to the pure gas tests. The truly cross-linked layer after a 5-min EDA-vapor treatment, can be considered as a pseudo homogeneous dense membrane [57], also demonstrates superior

H_2/CO_2 separation performance in pure gas tests compared to the high-performing conventional polymers [123]. This is due to the enhanced separation ability after vapor phase modification, which further confirms the validity of the vapor phase EDA modification strategy as an economically-viable technique for hydrogen purification by the use of highly effective polyimide membranes.

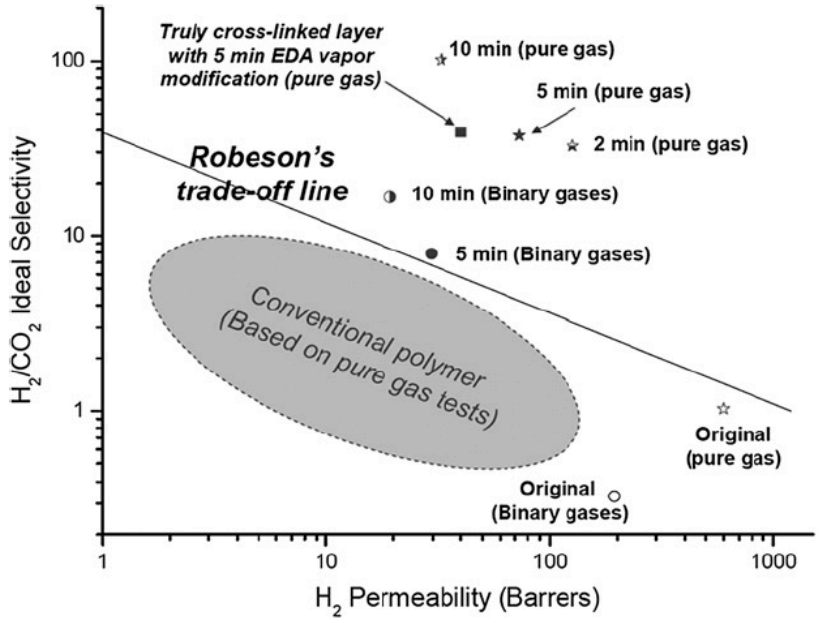

Figure 4.8 H_2/CO_2 separation performance of vapor-phase modified membranes in comparison with Robeson's upper bound line [124].

4.4 Summary

Vapor-phase EDA has been conveniently used to tailor the supramolecular structure of dense, flat sheet polyimide membranes for H_2/CO_2 separation. Due to the strong nucleophilicity of EDA, the imide groups in polyimides have been

converted into amide groups alongside simultaneous cross-linking between polymer chains, which is validated by FTIR-ATR and XPS analyses. The densified structure of the cross-linked membrane surface is also confirmed by XRD. The enhanced separation capability of polyimide membranes after the EDA-vapor modification is indicated by a significant increase in H_2/CO_2 selectivity from around 1 (original) to 102 (10-min vapor treatment). This can be attributed to a reduced diffusive pathway after intensive vapor-phase modification on the surface. Based on the resistance model, the intrinsic H_2/CO_2 separation properties of a vapor-modified polyimide layer were calculated to be higher than that of vapor-modified three-layered polyimide membranes. For vapor-phase modified membranes, the H_2/CO_2 selectivity in mixed gas tests is much lower than that in pure gas tests. However, the H_2/CO_2 separation performance in mixed gas tests is still much higher than that of conventional polymers [19]. The current results indicate that the vapor phase approach can potentially modify polyimide membranes for hydrogen purification. Together with intensive surface modification and the minimization of solvent swelling process of conventional solution approach, the vapor-phase modification technique is believed to be a much more suitable method to modify hollow fiber membranes for hydrogen purification, which will be disclosed in the next chapter.

CHAPTER FIVE:

A NOVEL STRATEGY FOR SURFACE MODIFICATION OF POLYIMIDE HOLLOW FIBER MEMBRANE BY VAPOR-PHASE DIAMINES FOR HYDROGEN PURIFICATION

5.1 Introduction – The vapor phase modification technique

Gas separation membranes exist in the forms of plate and frame, spiral wound, and hollow fibers [17]. Ascribing to high aspect ratios and flux, hollow fibers are preferred as commercial gas separation membranes. Additionally, hollow fiber membranes have self-mechanic support and are easy to handle and scale up. Primarily, hollow fibers are categorized into single layer and dual layer hollow fibers. Although single layer hollow fiber gas separation membranes are relatively easier to fabricate, dual layer hollow fibers maximize gas separation performance by providing lower substructure resistances while minimizing material costs, as only the selective layer is made up of expensive materials that provide gas selectivity [16]. Moreover, a thin selective layer eliminates tedious post-treatment processes like silicon rubber coating that is mandatory to enhance gas separation performances [125].

Methanol swelling renders the technique of solution cross-linking to be unsuitable for chemically modifying hollow fiber membranes [55, 109, 126]; especially for dual layer hollow fibers with an ultrathin selective skin as delamination may occur. Moreover, cross-linking solutions are typically non-recyclable due to contamination after use and considerable time is required to dry solution cross-linked membranes. Thus, in order to enhance the gas separation properties of polyimide hollow fibers while avoiding the disadvantages of solution cross-linking; a practical and cost-effective surface

modification technique must be deployed. Vapor-phase modification can potentially replace the solution-phase modification technique as this innovative process has the advantages of (1) a minimal swelling process; (2) surface-restrictive modifications; (3) the reusability of original diamines for economical considerations; and (4) modification process at room temperature [127].

This chapter demonstrates the effective use of a vapor-phase surface modification technique to enhance the H_2/CO_2 separation capability of polyimide/polyethersulfone (PES) dual layer hollow fibers via alterations to the chemical structure of the dense, selective polyimide outer layer. In addition to designing a batch process for vapor-phase modification, a continuous process has also been explored. To further demonstrate the versatility, other polyimide-based hollow fibers, polybenzimidazole (PBI)-Matrimid®/polysulfone (PSf) dual layer hollow fibers and Torlon® poly (amide imide) single layer hollow fibers were modified using the vapor-phase modification technique for H_2/CO_2 separation. The polyimide membranes modified by vapor-phase EDA were characterized using FTIR-ATR, XPS and XRD. Pure gas tests were performed to explore the H_2/ CO_2 separation ability of vapor-phase EDA modified polyimide membranes.

5.2 Materials and Experimental Methods

5.2.1 Materials for hollow fiber fabrications

Prior to polymer synthesis, the monomers 4,4'-(hexafluoroisopropylidene) diphthalic anhydride (6FDA) from Clariant (Germany) and 1,5-napthalenediamine (NDA) from Acros Organics were purified via vacuum sublimation. Polybenzimidazole (PBI) was purchased from Aldrich Chemical Company Inc. (Milwaukee, USA) and Matrimid® 5218 was bought from Vantico (Luxemburg). Radel A-300P polyethersulfone (PES), Udel® 3500 polysulfone (PSf), and Torlon® 4000T-MV poly (amide imide) were purchased from Amoco Polymers Inc (Marietta, OH). The chemical structures of 6FDA-NDA, Matrimid®, PBI and Torlon® are depicted in **Figure 5.1**. N-Methyl-2-pyrrolidone (NMP) and dimethylacetamide (DMAc) were purchased from Merck. THF was purchased from Fisher Chemicals. All the solvents were used as received unless otherwise stated. Ethylenediamine (EDA) was purchased from Sigma Aldrich and was used as received.

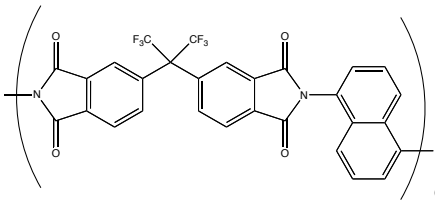

(i) 6FDA-NDA

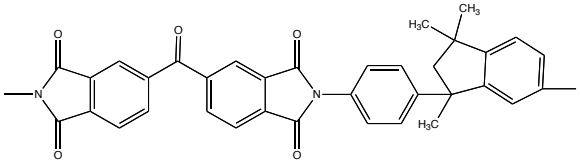

(ii)Matrimid® 5218

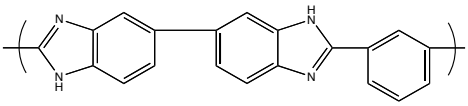

(iii) PBI

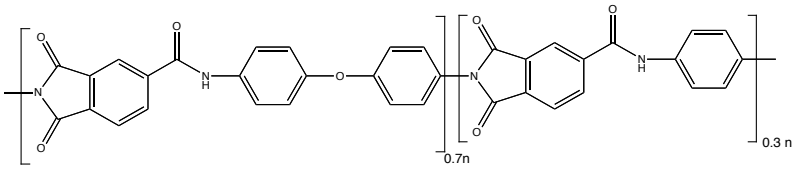

(iv) Torlon® 4000T-MV

Figure 5.1 Chemical structures of various polyimides that were used to fabricate the dense, selective layer of dual hollow fibers studied in this work. (i) 6FDA-NDA, (ii) Matrimid® 5218, (iii) PBI, and (iv) Torlon® 4000T-MV.

5.2.2 Synthesis of 6FDA-NDA and preparation of PBI/Matrimid® blends

A viscous poly(amic acid) solution was formed by dissolving equimolar amounts of 6FDA (dianhydride) and NDA (diamine) (total solid concentration is 20% by weight) in distilled NMP, under a nitrogen atmosphere. 3-picoline and acetic anhydride (molar ratio of 1:4) were added to the solution to form the polyimide. Polymer precipitation occurred in methanol, and the resultant solid polymer fibrils were dried under vacuum at 120°C prior usage. To prepare the PBI/Matrimid® (weight ratio of 1:1) blend, the polymers were dissolved together in DMAc.

5.2.3 Hollow fiber spinning

The dope compositions were determined according to a similar procedure

ascribed elsewhere [128, 129]. Briefly, the polymeric dopes were prepared by dissolving the respective polymers in the solvent under high-speed agitation to ensure complete dissolution [71, 128, 130, 131]. The solutions were degassed for 24 hours under atmospheric conditions prior to spinning. The dope compositions and spinning conditions for fabricating different hollow fiber membranes are shown in **Table 5.1**.

Table 5.1 Spinning conditions for different polyimide hollow fibers

Sample Name	**6FDA-NDA/PES dual layer**	**PBI-Matrimid/PSf dual layer**	**Torlon single layer**
Outer layer dope composition	27 wt.% 6FDA-NDA, 73 wt.% NMP/THF: 5:3 (v/v)	22 wt.% PBI-Matrimid® (1:1), 78 wt.% DMAc	28 wt.% Torlon®, 72 wt.% NMP
Inner layer dope composition	30 wt.% PES, 70 wt.% NMP/H_2O: 10:1 (w/w)	75 wt.% PSf, 25 wt.% NMP	-
Bore fluid composition	95/5 NMP/H_2O	95/5 NMP/H_2O	90/10 NMP/H_2O
External coagulant	Water	Water	Water
Outer layer dope flow rate (ml/min)	0.2	0.3	2
Inner layer dope flow rate (ml/min)	0.8	2	-
Bore fluid flow rate (ml/min)	0.3	1	1
Coagulation bath temperature (˚C)	25	25	25
Spinneret temperature (˚C)	50	25	50
Take-up rate(cm/min)	Free fall	Free fall	20
Air gap (cm)	8	1	5

Solvent exchange of the as-spun fibers using three consecutive 30-minute methanol circulations was done. Subsequently, n-hexane was used to replace methanol in the solvent exchange procedure. These hollow fiber membranes were ready for use after drying in air at ambient temperature (25 °C). The physical configurations of the hollow fiber membranes studied in this work are shown in **Figure 5.2**.

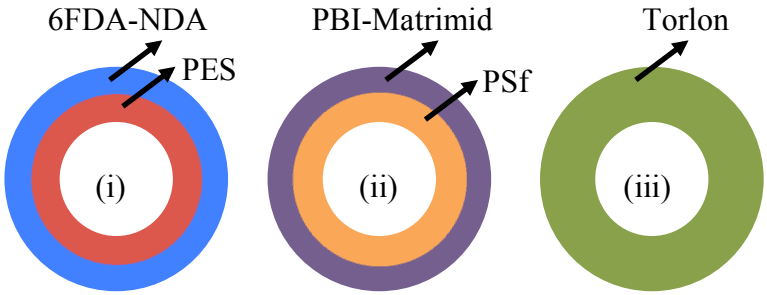

Figure 5.2 Physical configurations of hollow fiber membranes studied in this work. (i) 6FDA-NDA/PES dual layer hollow fiber, (ii) PBI-Matrimid® (blend)/PSf dual layer hollow fiber, (iii) Torlon® single layer hollow fiber

5.2.3 Vapor-phase EDA modification on hollow fiber membranes

All the vapor-phase modification techniques used in this work were done at 25 °C ± 1 °C. Prior to vapor phase modification, the ends of fibers were sealed with fast curing epoxy. This was to prevent chemical modification in the fiber lumen by the EDA vapor. After vapor-phase chemical modification, the test modules or hollow fibers were outgassed in a vacuum environment for 2 h at 30°C [132]. In this work, two vapor-phase modification techniques were utilized. Method A was a batch method similar to the original vapor-phase modification

technique as described in the previous chapter [127]. Method B was a continuous method whereby a stream of inert gas (nitrogen) was used to generate a continuous flow of EDA vapor.

The effect of vapor-phase modification time on H_2/CO_2 transport properties of the resultant fibers was investigated. For the 6FDA-NDA/PES and PBI-Matrimid®/PSf dual layer hollow fibers, the vapor-phase modification times were 2 and 5 minutes. For Torlon® single layer hollow fibers, the modification durations were 30 and 60 seconds. The different modification durations for Torlon® fibers were due to the poor mechanical integrity of the fibers with prolonged modification duration. This will be accounted for in Section 5.3.

5.2.3.1 Method A (batch vapor-phase modification)

Method A is based on the vapor-phase modification technique used in our previous work (detailed in Chapter 4) [127]. The setup of Method A is shown in **Figure 5.3 (a)**. In a covered containment, 100 mL of EDA was allowed to stabilize over 30 minutes. Using Equation 4.2, the EDA vapor pressure at 25 °C was calculated to be 12.0 mmHg and 1.6 v/v% of EDA vapor was present in the confined volume. Upon stabilization, the epoxy-sealed fibers were quickly exposed to the vapor-phase EDA. After stipulated vapor-phase modification durations, the surface modified fibers were removed from the containment and placed in a vacuum environment of 3 torr for 2 hrs at 30 °C.

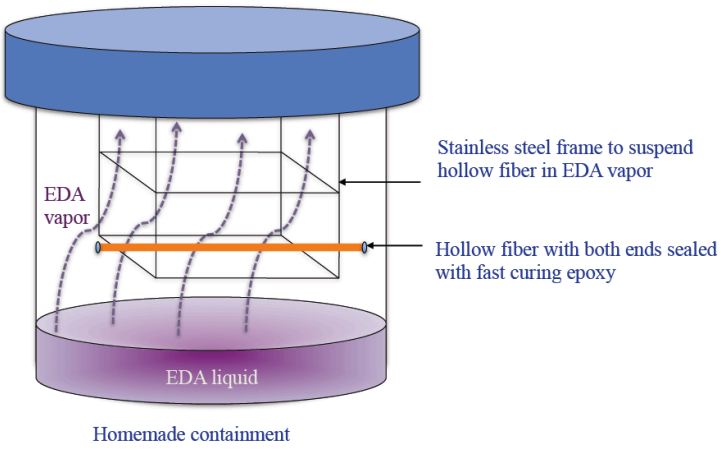

Figure 5.3 (a) Batch vapor-phase modification technique. The suspended hollow fibers are modified upon exposure to ethylenediamine (EDA) vapor.

5.2.3.2 Method B (continuous vapor-phase modification)

The set-up of Method B is shown in **Figure 5.3 (b)**. A steady stream of nitrogen (99.9995 % purity) purchased from Soxal Pte. Ltd. was channeled into the liquid EDA via polytetrafluroethylene (PTFE) fibers obtained from Markel Corporation, at a continuous flow rate of 10 std liters/min. An N_2-calibrated Aalborg GFC 17 mass flow controller was used to control the nitrogen flow rate into the liquid EDA. In Method B, fibers were assembled into a test module prior to surface modification. The ends of each fiber were sealed with fast curing epoxy to prevent chemical modification from the lumen side. The test module containing the fibers was attached to a silicone tubing that connected to the homemade containment. A stop-plug along the silicone tubing was used to control the EDA vapor exposure time. The main difference between Method A and Method B is the ability of the latter approach to specifically modify fibers that have been

assembled into modules, which is more attractive for the fabrication of commercial membranes for gas separation. After vapor-phase modification, the modules were removed from the silicone tubing and placed in a vacuum environment of 3 torr for 2 hrs at 30 °C.

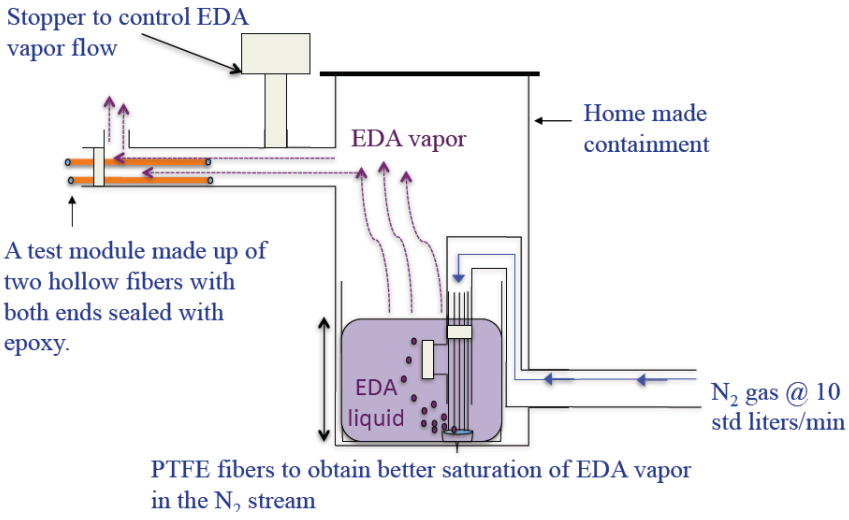

Figure 5.3 (b) Continuous vapor phase modification technique.

5.2.4 Membrane characterization

ATR-FTIR spectroscopy performed over 64 scans in the range of 400 to 4000 cm^{-1} was used to characterize the chemical modifications in the polyimide selective layers. The resolutions of the spectra were 4 cm^{-1}. The area of interest indicating the conversion of polyimide to polyamide lies in the region of 1400 – 1800 cm^{-1} [133]. The data was analyzed using Spectrum Version 5.3 (analytical software). XPS was used to validate the chemical modifications while FESEM was used to observe the morphological changes upon chemical structure modifications. The H_2 and CO_2 permeance of pristine and modified

hollow fibers were characterized using a variable-pressure constant-volume gas permeation cell. The detailed description of the permeation cell set-up was described previously [134]. Each module consisted of 2 fibers with an effective length of approximately 7.5 cm. The upstream pressure was 20 psig and the operating temperature was 35 °C. The permeance (P/L) of each fiber was determined using the technique described in Section 3.9.2. The ideal separation factor, $\alpha_{A/B}$, can be determined from the following equation:

Equation 5.1

$$\alpha_{A/B} = \frac{(P/L)_A}{(P/L)_B}$$

5.3 Results and discussion

5.3.1 Chemical characterizations of hollow fibers before and after modification

After vapor-phase modification using Method B, changes in chemical structure at the outermost region of hollow fibers can be observed. **Figure 5.4** describes the underlying chemical reaction between the 6FDA-NDA polyimide and EDA during vapor phase modification. Other reactions occurring during modification include grafting and etching i.e. main chain scission [57].

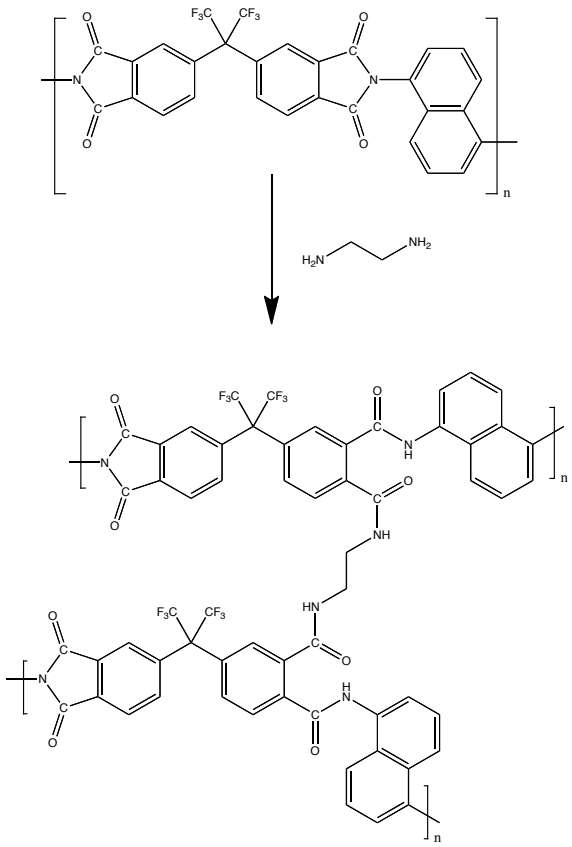

Figure 5.4 EDA induced vapor-phase modification of 6FDA-NDA.

The FTIR spectra in **Figure 5.5 (a)** shows the signatory peaks of imide groups in the pristine 6FDA-NDA polymer. The peaks at 1788 and 1720 cm^{-1} belong to the C=O group constituting the imide ring [133]. The peak denoting the C-F group in 6FDA appears at 1245 cm^{-1}. The peak at 1360 cm^{-1} is due to the C-N stretch of the imide group whilst the peak at 1069 cm^{-1} corresponds to the transverse C-N-C stretch of the imide group [133]. To add on, the naphthalene moiety of the NDA group contributes to the signatory peaks of the 6FDA-NDA polyimide. The C=C stretch of the naphthalene structure is signified by a weak peak at 1548 cm^{-1}; and a doublet at 1603 $cm^{-1}$and 1629 cm^{-1}; whilst the di-substituted naphthalene structure results in strong peaks at 783 cm^{-1} and 1419 cm^{-1} [133]. The amidization conversion process depicted in Figure 5.4 yields from the strong nucleophilicity of EDA [56]. From Figure 5.5 (a), the weakening or disappearance of imide signatory peaks alongside the formation of amide characteristic peaks at 1644 cm^{-1} (C=O stretch of amide group) and 1560 cm^{-1} (C-N stretch of amide group) validates the chemical reaction between polyimides and EDA. In Figures 5.5 (b) and (c), imide characteristic peaks at around 1788 cm^{-1} and 1720 cm^{-1} (C=O group), 1360 cm^{-1} (C-N stretch of the imide group) are observed for PBI-Matrimid®/PSf and Torlon®, respectively. In pristine Torlon®, characteristics peaks of amides are seen at 1644 cm^{-1} (C=O stretch of amide group) and 1520 cm^{-1} (C-N stretch of amide group). The conversion of imides in pristine PBI-Matrimid®/PSf and Torlon® into amides has occurred during the vapor phase modification. The FTIR spectra of vapor

modified PBI-Matrimid® and Torlon® fibers display weakened imide peaks and appearance or strengthening of amide peaks at 1644 cm^{-1} (C=O stretch of amide group) and 1520 cm^{-1} (C-N stretch of amide group). With longer vapor-phase modification durations, the intensity of the peaks representative of amide groups increases. This relationship between the greater extent of conversion from imide to amide groups and the increments in vapor phase modification timings can be similarly inferred from XPS analyses.

(a)

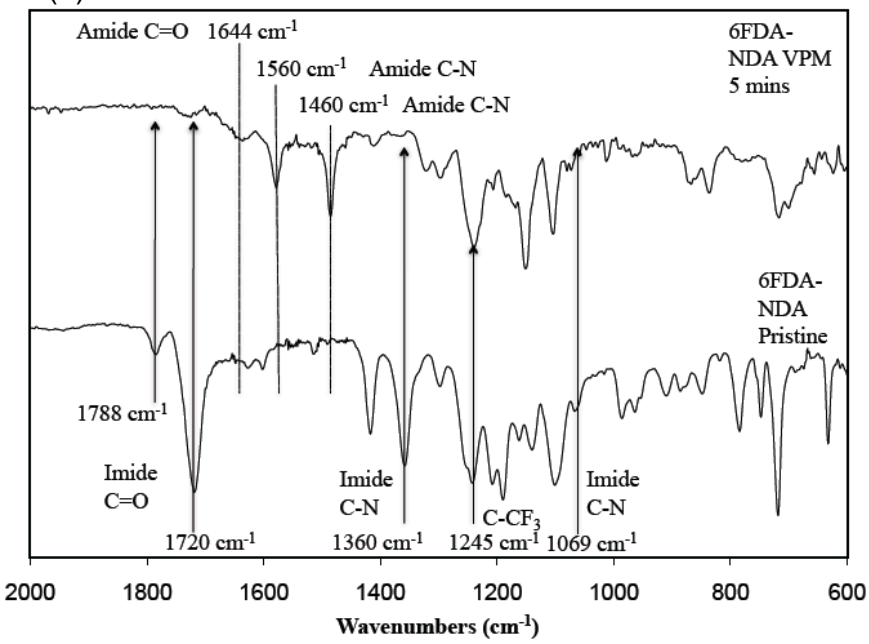

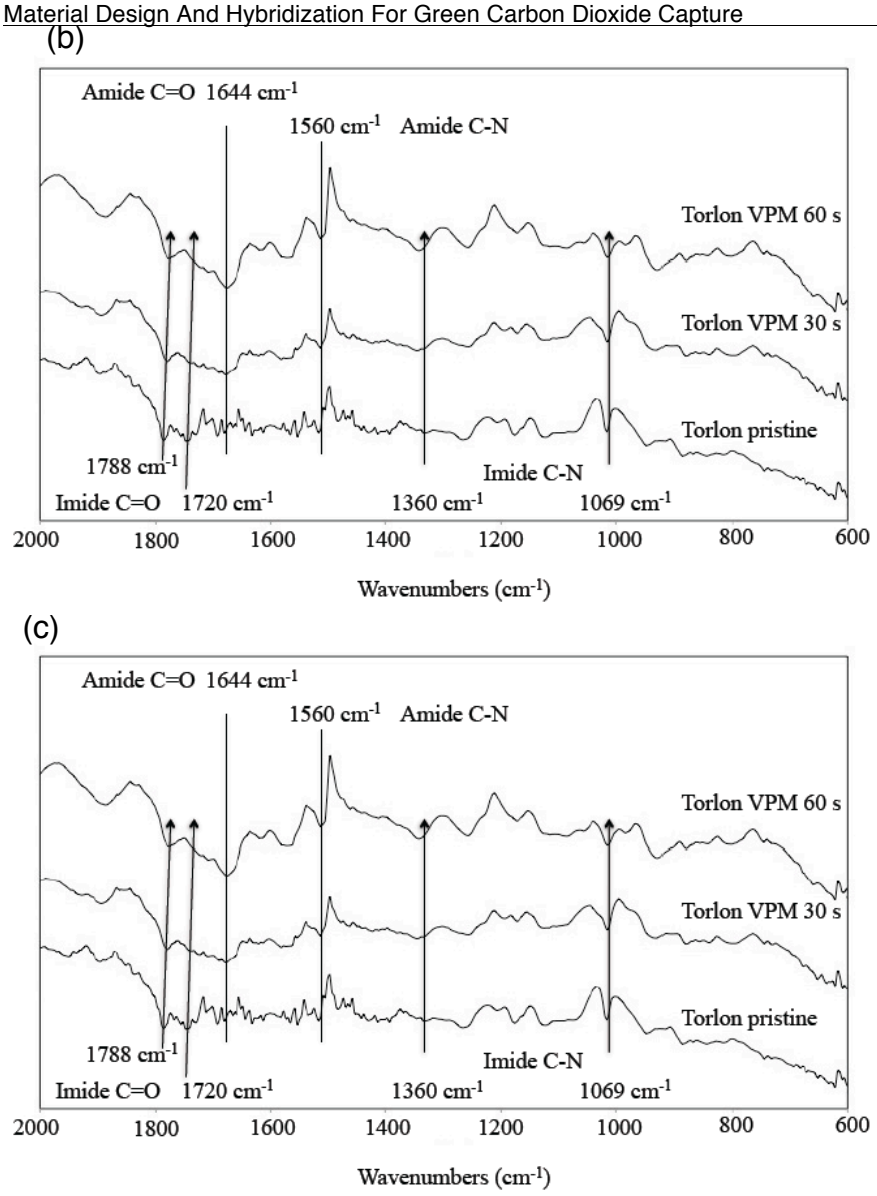

Figure 5.5 FTIR spectra of (a) 6FDA-NDA/PES dual layer hollow fiber, (b) PBI-Matrimid®/PSf dual layer hollow fibers, and (c) Torlon® single layer hollow fibers before and after vapor phase modification (VPM) using Method B.

The elemental compositions of nitrogen and fluorine were determined using XPS. With longer vapor-phase modification durations, the nitrogen content in these fibers increases with imide-to-amide conversion. Like 6FDA-durene, the fluorine content in 6FDA-NDA/PES hollow fibers remains unchanged during

vapor-phase modification. Hence, the N/F ratio is a good indication of imide-to-amide conversion. The theoretical N/F ratio for pristine 6FDA-NDA is 0.32. In this work, the N/F ratio of pristine 6FDA-NDA/PES hollow fibers is 0.52. The difference between experimental and theoretical values is possibly attributed to the presence of residual NMP solvent in the membranes [135]. After 2 and 5 minutes of vapor modification using method B, the N/F ratio increases to 1.71 and 3.95, respectively. For Torlon® fibers, the N/O ratio is used, as the concentration of oxygen remains unchanged after the vapor phase modification. The theoretical N/O ratio of Torlon fibers is 0.08. The N/O ratio in Torlon® fibers increases from 0.10 (pristine) to 0.11 (2 minutes) to 0.14 (5 minutes). Assuming that negligible amounts of unreacted diamine remained in the membranes, the increasing trend of nitrogen content alongside the results obtained from FTIR analysis supports the conversion of imides into amides.

5.3.2 Physical characterization of hollow fibers before and after modification

The intersegmental distance, d-space, between polymer chains before and after vapor-phase modification was determined using XRD. **Figure 5.6** shows that The XRD peak of the 6FDA-NDA/PES fibers is shifted to larger 2θ values after vapor phase modification. The 2θ value increased from 17.64° for the pristine fibers to 18.22° for the 5 minute modified fiber. Based on Bragg's Law ($n\lambda = 2d \sin\theta$), larger 2θ values lead to smaller d-spaces between the polymer chains

over longer vapor-phase modification durations. The d-space between the pristine 6FDA-NDA polymer chains is calculated to be 5.08 Å. Upon vapor-phase modification, the d-space decreases from 4.97 Å to 4.93 Å when vapor phase modification time increases from 2 to 5 minutes. This slight decrease in d-space can be attributed to the tightening of the 6FDA-NDA polymer chains via vapor-phase modification and the space filling effects of diamine molecules. Similar trends of decreasing d-space with increasing vapor phase modification time have been observed for hollow fibers fabricated from PBI-Matrimid®/PSf and Torlon®. The d-space in pristine PBI-Matrimid®/PSf hollow fibers is 5.17 Å. Upon vapor-phase modification for 2 and 5 minutes, the d-space values between the PBI-Matrimid® polymer chains become 5.13 Å and 5.07 Å, respectively. The d-space in pristine Torlon® hollow fibers is 4.35 Å. The d-space decreases to 4.32 Å and 4.30 Å after 30 and 60 seconds of the vapor-phase modification, respectively.

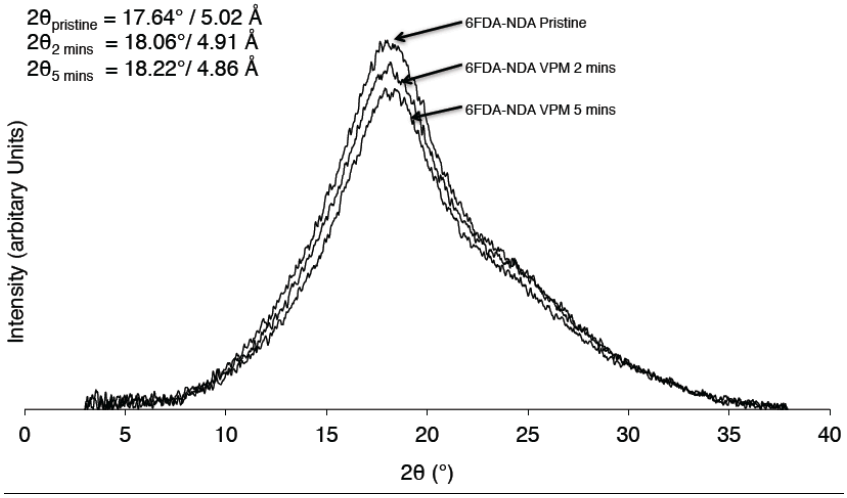

Figure 5.6 XRD spectra of 6FDA-NDA/PES dual layer hollow fibers before and after vapor phase modification (VPM) using Method B.

Figure 5.7 shows the morphology of hollow fibers before and after vapor-phase modification using Method B. In pristine hollow fibers, the polymeric structure of the outermost regions consists of overlapping nodules. After vapor-phase modification, the nodular structure of the outermost layers transforms into a continuous and uninterrupted dense layer. Further examination reveals that the thickness of the dense layer increases with an increase in vapor phase modification time. In 6FDA-NDA/PES hollow fibers modified using Method B, the dense layer thickness increases from 3.7 μm (2 minutes) to 4.7 μm (5 minutes). In 6FDA-NDA fibers modified using Method A, the dense layer thickness increases from 0.5 μm (2 minutes) to 2 μm (5 minutes). A thicker dense layer was formed on 6FDA-NDA hollow fibers modified using Method B. This observation can be ascribed to different amide conversion rates. The presence of an inert gas flow enhances the flow rate of the reactant (EDA), which will consequently increase product formation [136]. In Method B, the nitrogen gas flow increases the flow rate of EDA molecules. Consequently, enhancing amide conversion. Faster moving EDA molecules are able to penetrate further into the inner regions of the 6FDA-NDA polymers. On the other hand, in Method A, the flow rate of the EDA molecules is much slower. Slow moving EDA moieties tend to adsorb on the surface rather than penetrate into the inner regions of the 6FDA-NDA polymer. As a result, only the outer layers experience intense amine conversion; thus the dense layer in hollow

fibers modified by Method A appears to be denser than those observed in fibers modified by Method B. The smaller but denser layers in fibers modified by Method A appear to have a similar effect on gas permeance and selectivity when compared to fibers (modified by Method B) that possess larger but less dense regions. This is an effect of substrate resistance as mentioned in the previous chapter and in reference [127]. For PBI-Matrimid®/PES hollow fibers, the thickness of the dense layer increases from 2.4 μm (2 minutes) to 7.7 μm (5 minutes). In Torlon® fibers, the dense layer thickness increases from 2.3 μm (30 seconds) to 3.6 μm (60 seconds). From Figure 5.6, the formation of this dense layer appears to be in a radial mode, indicating that the vapor-phase modification method alters the surface of hollow fibers uniformly. Another observation made is the overall reduction in the outer layer thickness of dual layer hollow fiber membranes, which is possibly attributed to the densification process and etching i.e. main chain scission [57].

(a)

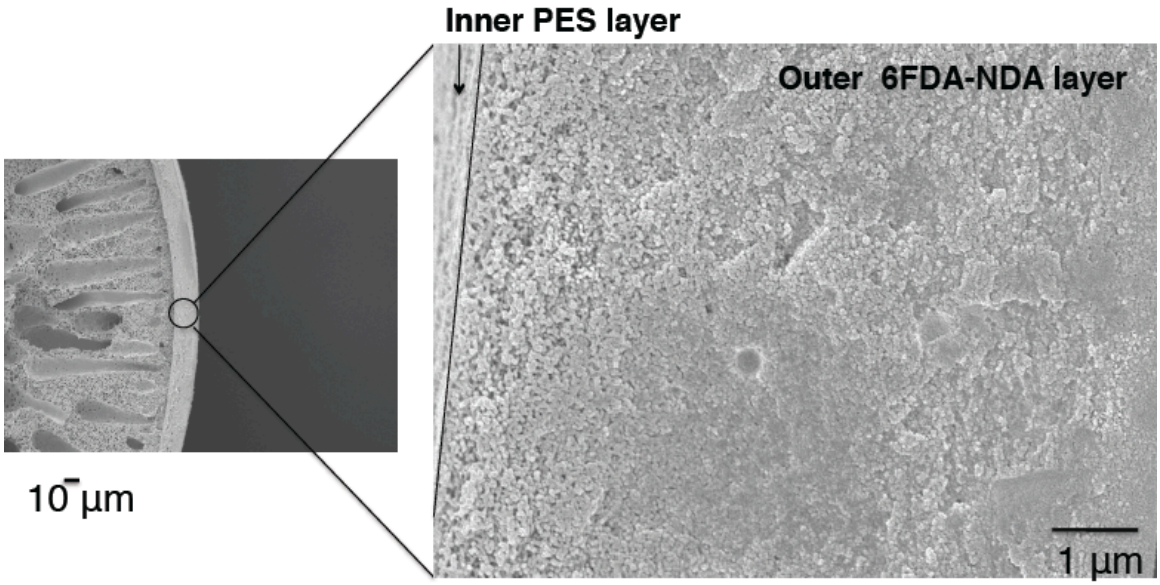

Figure 5.7 (a) FESEM images of 6FDA-NDA/PES before vapor-phase modification using Method B

(b)

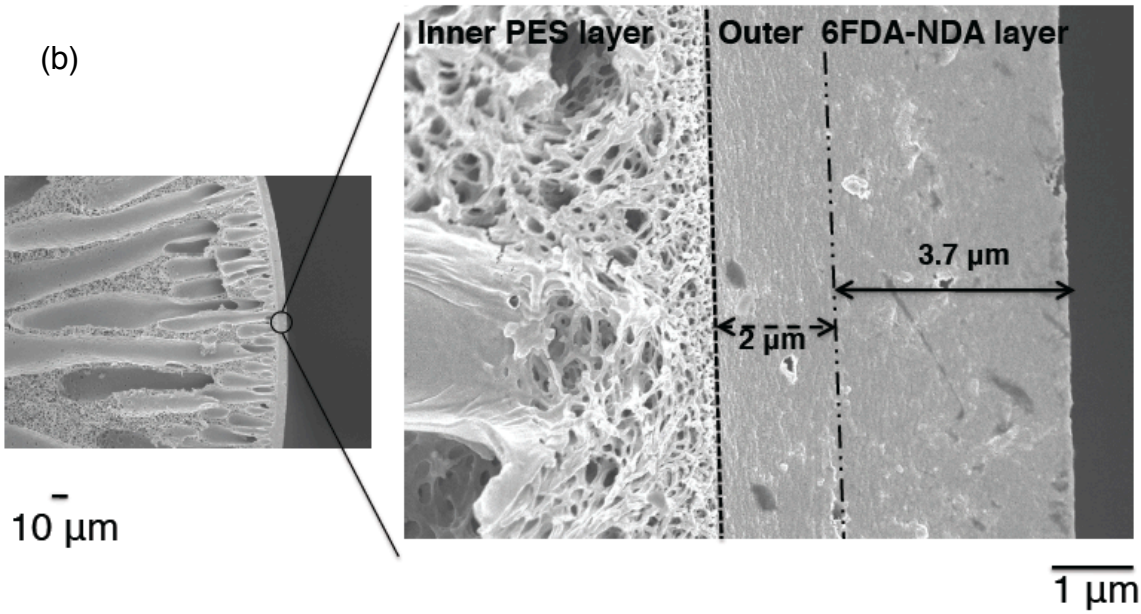

Figure 5.7 (b) FESEM images of 6FDA-NDA fibers after 2-min vapor-phase modification. Formation of a dense, uninterrupted layer of 3.7 µm at the outermost layer and a 2 µm layer of relatively un-densified area.

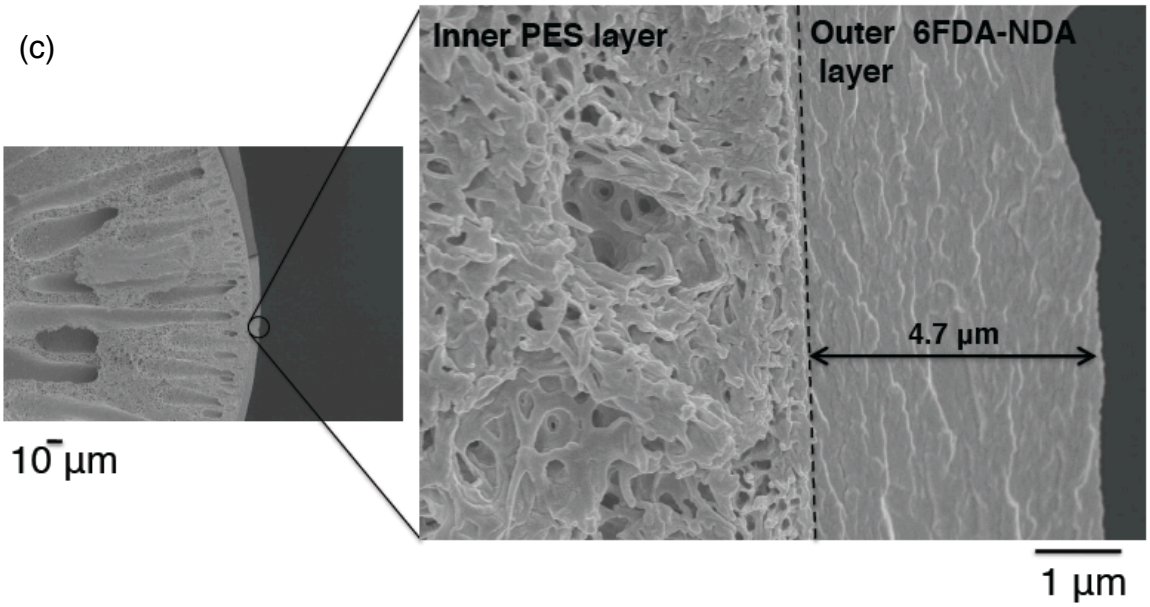

Figure 5.7 (c) FESEM images of 6FDA-NDA fibers after 2-min vapor-phase modification. Formation of a dense, uninterrupted layer of 4.7 µm. Only densified areas are seen in the outermost layer.

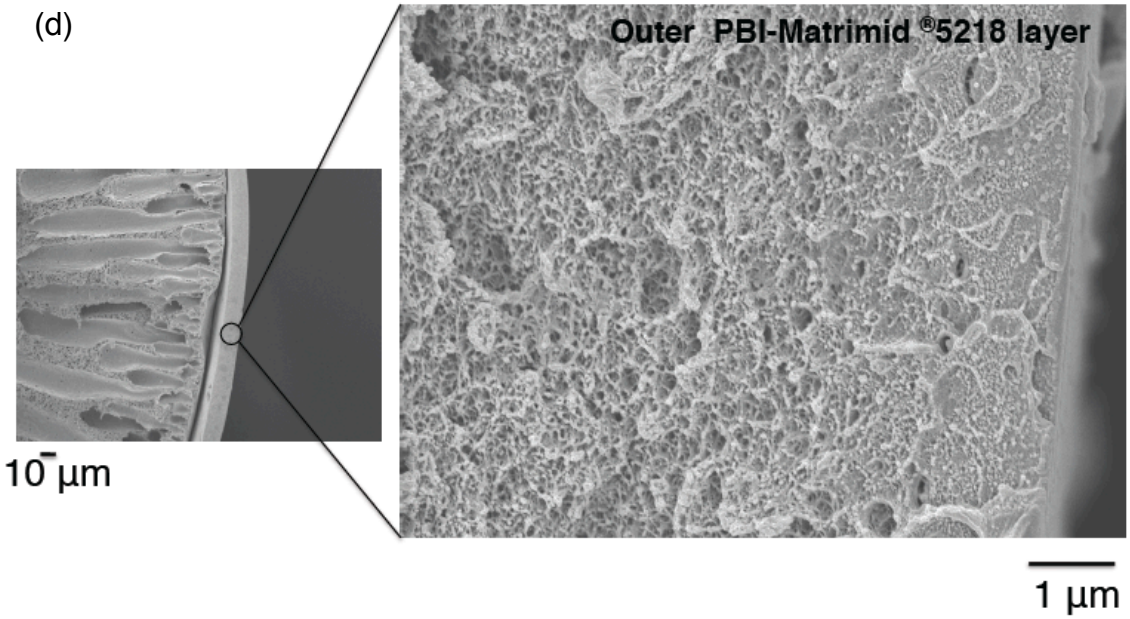

Figure 5.7 (d) FESEM images of PBI-Matrimid® 5218/PSf fibers before vapor-phase modification using Method B

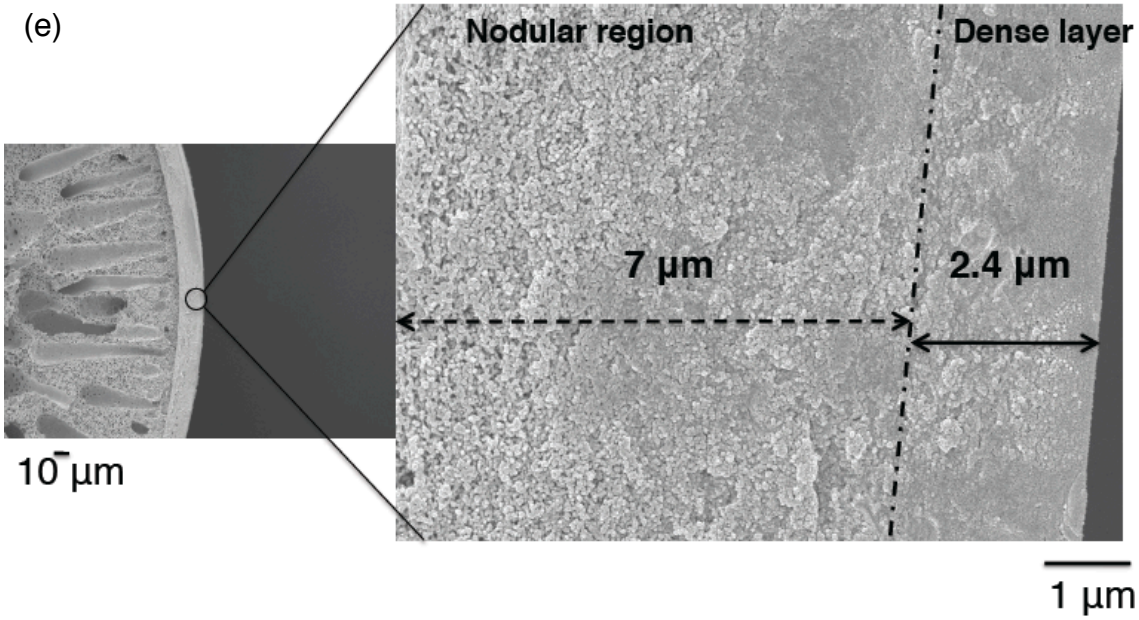

Figure 5.7 (e) FESEM images of PBI-Matrimid® 5218/PSf fibers after 2-min vapor-phase modification using Method B. Formation of a dense, uninterrupted layer of 2.4 µm at the outermost layer and a 7µm layer of relatively un-densified area remain.

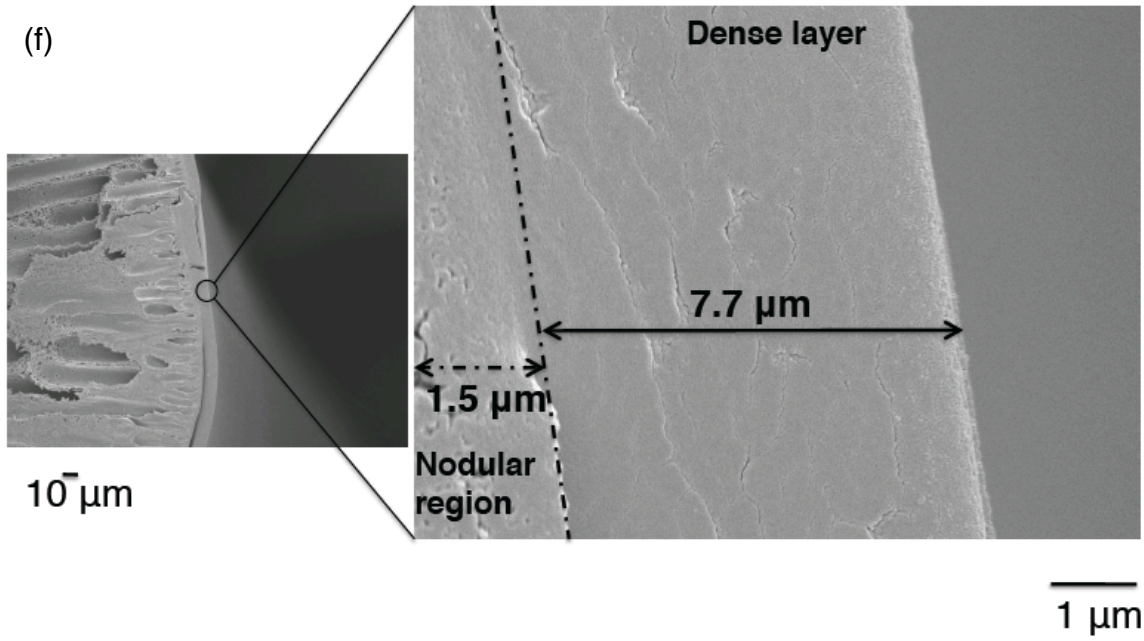

Figure 5.7 (f) FESEM images of PBI-Matrimid® 5218/PSf fibers after 5-min vapor-phase modification using Method B. Formation of a dense, uninterrupted layer of 1.5 µm at the outermost layer and a 7.7 µm layer of relatively un-densified area remain.

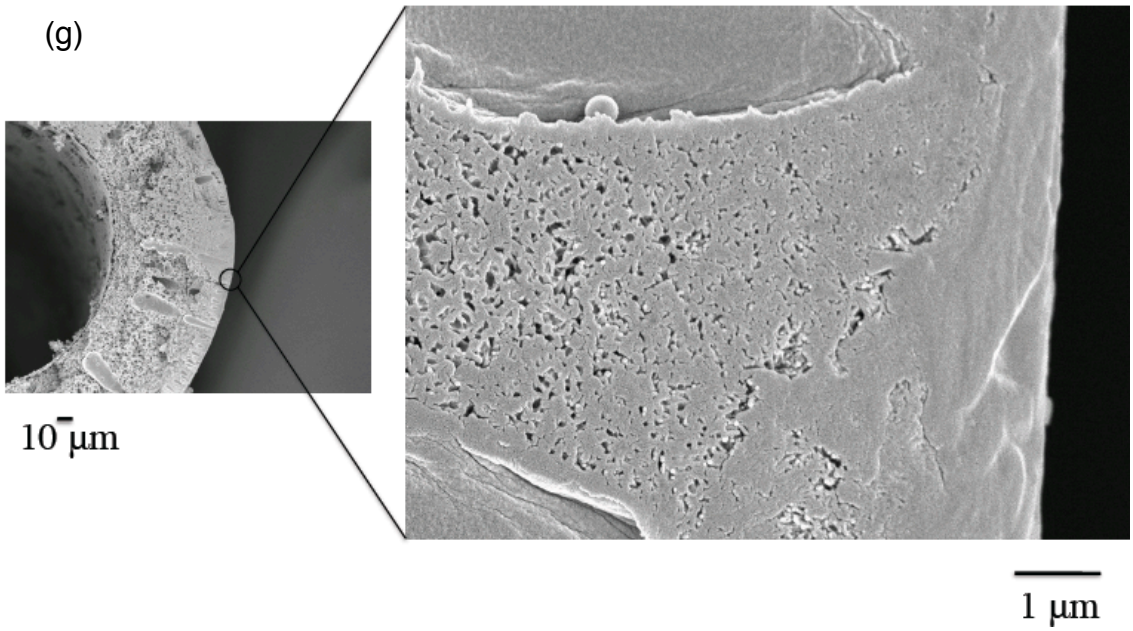

Figure 5.7 (g) FESEM images of Torlon® 4000T-MV fibers before vapor-phase modification.

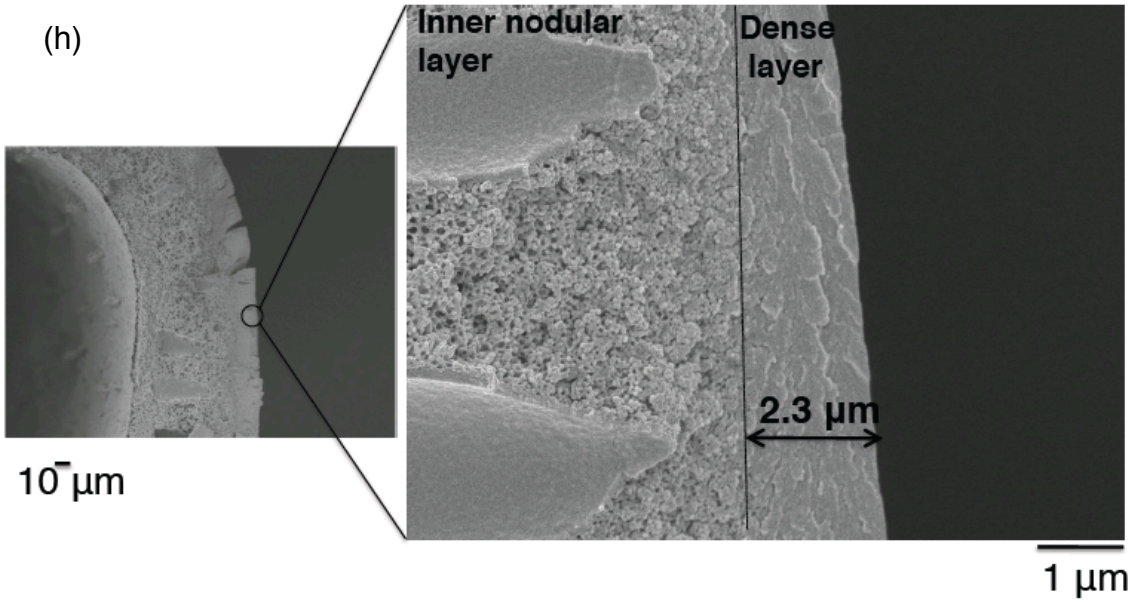

Figure 5.7 (h) FESEM images of Torlon® 4000T-MV fibers after 30 seconds of vapor-phase modification using Method B. Formation of a dense, uninterrupted layer of 2.3 µm at the outermost layer.

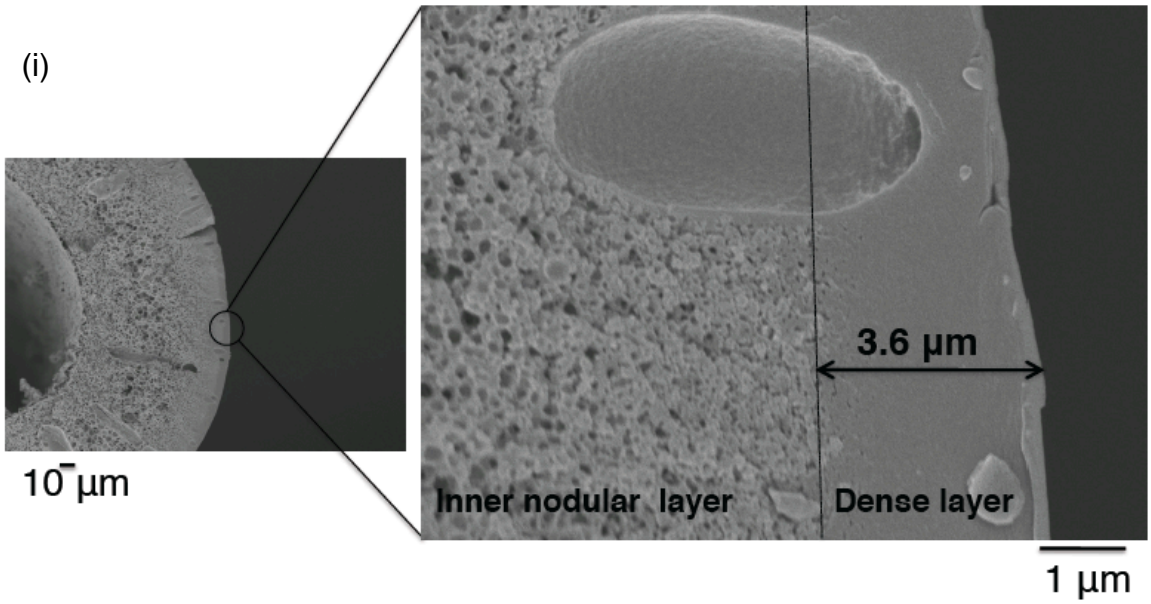

Figure 5.7 (i) FESEM images of Torlon® 4000T-MV fibers after 60 seconds of vapor-phase modification using Method B. Formation of a dense, uninterrupted layer of 3.6 µm at the outermost layer.

The 6FDA-NDA/PES and PBI-Matrimid®/PSf dual layer hollow fibers were subjected to vapor-phase modification for an optimal duration of 5 minutes, while Torlon® single layer fibers were vapor-phase modified for an optimal duration of 60 seconds. Vapor-phase modifications beyond the optimal duration were ineffective and detrimental to fiber structure. In dual layer hollow fibers, the densified outer selective layer apparently delaminates from the inner core when the vapor-phase modification time exceeds 5 minutes and after the vacuum drying process. This may be attributed to (1) the occurrence of "tensional stresses" [137, 138] induced within the spatial periphery of the pores in the fibers during the out-gassing of excessive unreacted EDA, (2) amidization and different isobaric expansivities [139] inducing evaporative stresses between the dense selective layer and inner core, and (3) contraction of the outer dense polymeric layer as a result of the vapor-phase modification process [140] as evidenced by the XRD and FESEM data. Meanwhile, in single layer Torlon® hollow fibers, when vapor-phase modification duration exceeds the optimal duration of 60 seconds, these fibers start to bend. As mentioned previously, the diamine modification causes the polymer structure to contract. As the imide-to-amide conversion propagates from the outmost layer to the inner regions, the polymer structure in the outmost regions contracts whilst the polymer structure in the inner regions remains the same. The inward propagating contraction forces act on the undisturbed inner regions and may cause the fiber to bend.

5.3.3 H_2 and CO_2 separation properties of vapor-phase modified hollow fibers

To evaluate the H_2/CO_2 selectivity of hollow fibers, pure gas tests were carried out. **Tables 5.2 and 5.3** summarize the gas permeance and selectivity of fibers modified using Method A and B, respectively. Resulting from the formation of a new dense layer and tightened polymer chains, both H_2 and CO_2 permeance decrease as a function of longer vapor-phase modification durations. As the inter-chain distance between the polymers decreases (evident from XRD data), the space for gases to pass through becomes constricted. The magnitude of decline in CO_2 permeance for 6FDA-NDA/PES fibers is more pronounced than the decrease in H_2 permeance. This is attributed to their difference in kinetic diameter. The kinetic diameter of CO_2 is 3.3 Å whereas the kinetic diameter of H_2 is 2.89 Å [41]. The tightened polymer chains create smaller transport channels that prevent larger gases like CO_2 from passing through. This accounts for the more drastic decline in CO_2 permeance and the corresponding higher H_2/CO_2 selectivity after vapor phase modification. In Tables 5.2 and 5.3, the H_2/CO_2 selectivity of 6FDA-NDA/PES dual layer hollow fibers increases with longer vapor-phase modification duration. Similar trends in gas permeance and H_2/CO_2 selectivity are also observed for PBI-Matrimid®/PSf and Torlon® fibers as the vapor modification duration increases.

Table 5.2 H_2 and CO_2 permeance and selectivity of 6FDA-NDA/PES, PBI-Matrimid® 5218 (blend)/PSf, Torlon® 4000T-MV hollow fibers before and after vapor phase modification using the batch method (Method A)

Sample Name	H_2 (GPU)	CO_2 (GPU)	α (H_2 /CO_2)
6FDA-NDA/PES (original)	72.6	43	1.69
6FDA-NDA/PES VPM 2 min	12.1	4.05	2.98
6FDA-NDA/PES VPM 5 min	3.41	0.098	34.80
PBI-Matrimid®/PSf original	27.7	6.88	4.02
PBI-Matrimid®/PSf VPM 2 min	18.6	3.42	5.44
PBI-Matrimid®/PSf VPM 5 min	11.9	1.56	7.62
Torlon® - original	7.07	1.03	6.86
Torlon® VPM 30 secs	1.64	0.158	10.4
Torlon® VPM 60 secs	0.135	0.028	4.82

Table 5.3 H_2 and CO_2 permeance and selectivity of 6FDA-NDA/PES, PBI-Matrimid® 5218 (blend)/PSf, Torlon® 4000T-MV hollow fibers before and after vapor phase modification using the continuous method (Method B).

Sample Name	H_2 (GPU)	CO_2 (GPU)	α (H_2 /CO_2)
6FDA-NDA/PES (original)	72.6	43	1.69
6FDA-NDA/PES VPM 2 min	15.4	4.13	3.74
6FDA-NDA/PES VPM 5 min	4.44	0.13	35.52
PBI-Matrimid®/PSf original	27.7	6.88	4.02
PBI-Matrimid®/PSf VPM 2 min	21.7	3.77	5.75

PBI-Matrimid®/PSf VPM 5 min	13.8	1.77	7.78
Torlon® - original	7.07	1.03	6.86
Torlon® VPM 30 secs	1.32	0.12	11
Torlon® VPM 60 secs	1.03	0.16	6.44

The formation of a dense layer with varying thickness can be attributed to the different amounts of imide groups present in the different materials used in this work. Comparing 6FDA-NDA with PBI/Matrimid® and Torlon®, the 6FDA-NDA polymers have more imide units. With more imide groups available for conversion, the extent of modification and amount of cross-linking activity are higher when compared to PBI/Matrimid® and Torlon®. With a greater degree of diamine modification, the magnitude of decline in the d-space becomes more pronounced. Therefore, the improvement in H_2/CO_2 selectivity of these fibers follows the trend of 6FDA-NDA/PES > PBI/Matrimid®/PSf > Torlon®.

Tables 5.2 and 5.3 also compare the gas separation performance of hollow fibers modified by these two methods. For each type of hollow fiber membranes, Method B produces hollow fibers with comparable or slightly better H_2/CO_2 selectivity than Method A. These minor differences in separation performance may be attributed to the different extent of amide conversion and modification thickness. Clearly, both methods are effective for diamine modification of hollow fiber membranes for hydrogen purification. However,

since the continuous process is more industrial and environmental friendly than the batch process, it has great potential for scale up and industrialization on polyimide membranes for H_2 and CO_2 separation.

5.4 Summary

The two vapor-phase modification techniques have been examined on various polyimide membranes for H_2 and CO_2 separation. During vapor-phase modification, imides were converted into amides alongside a decrease in polymer chain spacing. Resulting from such physiochemical changes, the H_2/CO_2 separation capabilities of these different hollow fibers are enhanced. Both batch and continuous modification methods are effective. Although the continuous vapor-phase modification method can simplify post-treatment process and reduce solvent wastage while significantly enhancing H_2/CO_2 selectivity, the gas permeance or permeability of glassy polymers like polyimides are inadequate for industrial applications.

Materials with high permeability and permselectivity are preferred for industrial gas separation membranes. Another approach to capture CO_2 from light gases using polymeric membranes is by using CO_2-philic materials and nanocomposites. The next few chapters will concentrate on the synthesis of CO_2-philic nanocomposites that are highly permeable with good CO_2/H_2 selectivity at near ambient operating conditions.

CHAPTER SIX:

ORGANIC-INORGANIC MEMBRANES FOR CO_2 CAPTURE FROM LIGHT GASES

6.1 Introduction to reverse-selective membranes

Gas permeability (P) in membranes is governed by the product of solubility (S) and diffusivity (D) coefficients, i.e. P = S x D. Gas separation membranes can be classified as conventional membranes that operate based on gas diffusivity selectivity, i.e., size selection, and reverse-selective membranes that rely on gas solubility selectivity. Conventional membranes (size selective) are typically fabricated using glassy materials while reverse-selective membranes are usually made up of rubbery materials. CO_2/H_2 separation is ideally achieved using reverse-selective membranes that preferentially allow larger CO_2 gas molecules to permeate to low pressures while retaining the smaller H_2 gas molecules in the retentate at high pressures [17, 24, 28, 29]. Most membranes are expected to have $S_{CO_2}/S_{H_2} > 1$ and $D_{CO_2}/D_{H_2} < 1$ based on size and thermodynamic differences between CO_2 and H_2; however, reverse-selective membranes have a sufficiently high solubility selectivity that overcomes the adverse diffusivity selectivity. An effective strategy to fabricate reverse selective membranes is to use high CO_2 affinity materials [24]. For instance, in amorphous PEO membranes, a CO_2/H_2 selectivity of 10 at 35 °C was achieved by enhancing S_{CO_2} via a dipole-quadrapole interaction between the acidic CO_2 and the polar ether oxygens [74, 77]. Industrial-scale CO_2/H_2 separation for green hydrogen production by membranes would be more practical if the CO_2 permeability of current state-of-the-art PEO-based membranes are significantly increased while maintaining similar or achieving higher selectivity.

Organic-inorganic membranes synthesized from simple fabrication processes have shown high CO_2 affinity that leads to good CO_2 permeability and CO_2/light gas separation [94]. Sforça et al. demonstrated that polyether-silicate organic-inorganic membranes synthesized using sol-gel processes possessed CO_2 permeability of 125 Barrer. The H_2 and N_2 permeability reached 18 and 2.1 Barrer, respectively. Acid-catalyzed sol-gel methods yield organic-inorganic materials that possess finely dispersed inorganic nanoparticles in the organic phase [141, 142]. Shao and Chung reported that organic-inorganic membranes fabricated using polyether diamines and silicate nanostructures [29] display comparable CO_2/H_2 separation properties to the membranes synthesized from cross-linked organic PEO-acrylate monomers [24]. At 35°C, the CO_2 permeability of this organic-inorganic membrane reaches 370 Barrer with a CO_2/H_2 selectivity of 9 [29]. At the expense of good mechanical properties, the CO_2 permeability of these organic-inorganic materials can be enhanced with more polyether diamines [29]. To enhance CO_2 permeability while inhibiting the side effects of excessive polyether content, short polyether side-chains can be grafted onto the main chains of the organic-inorganic material. The PEG side-chain grafts can minimize chain mobility in the main chains, thus, retaining mechanical strength while enhancing the interaction of the resultant nanohybrid material with highly condensable gas penetrants.

6.2 Materials and Experimental Methods

6.2.1 Starting materials for organic-inorganic materials

Jeffamine® ED-2003 (M_w = 2000 g/mole) was used in this part of the work; it is a commercially available water soluble polyether diamine derived from a propylene oxide end-capped polyethylene glycol i.e., the polyether segment structure is polypropylene oxide – polyethylene oxide – polypropylene oxide (PPO-PEO-PPO). Polyethylene glycol methacrylate (PEGMA: M_w = 360 g/mole), ethanol (HPLC grade) and 3-glycidyloxypropyltrimethoxysilane (GOTMS: M_w = 236 g/mole) were purchased from Sigma Aldrich, Singapore. Hydrochloric acid (HCl) was purchased from Fisher Scientific. All chemicals and solvents, except for PEGMA, were used as received. These chemicals were also used to fabricate the base materials that are described in Chapters 7, 8, and 9. The inhibitors in PEGMA were removed using activated carbon. For every 100 mL of PEGMA, 4 grams of activated carbon was added and stirred for 1 hour, after which, the activated carbon was filtered from this mixture. These procedures were repeated 3 times. The purified PEGMA was stored at 4 °C. **Figure 6.1** shows the monomers used for the work described in this chapter.

(a)

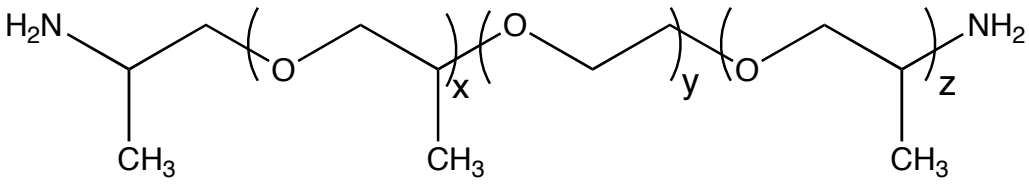

Jeffamine M_w 2000 g/mole

(b)

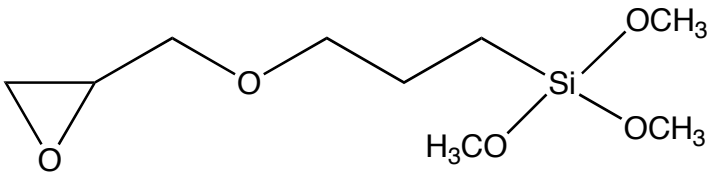

GOTMS M_w 236 g/mole

(c)

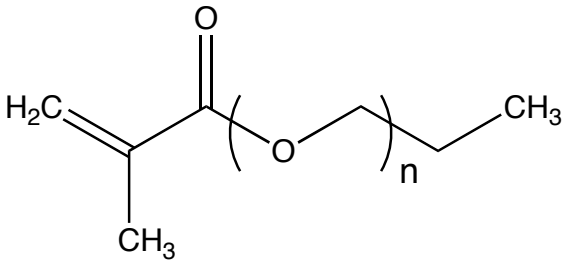

PEGMA M_w 360 g/mole

Figure 6.1 Chemical structures of the monomers used in this work. (a) Jeffamine ED-2003 – a commercially available PPO-PEO-PPO diamine, (b) 3-glycidyloxypropyltrimethoxysilane (GOTMS), and (c) polyethylene glycol methacrylate (PEGMA).

6.2.2 Synthesis of organic-inorganic and nanohybrid material

A catalyzing aqueous solution containing 37.5 wt.% HCl was used to hydrolyze GOTMS. After 30 minutes of hydrolysis at room temperature, the alkoxysilane solution was immediately added to a solution consisting of 2 wt.% polyether diamine dissolved in 70 wt.% ethanol and 30 wt.% distilled water. An epoxy-amine reaction was facilitated by stirring the resultant mixture at 750 rpm at 60

°C for one hour. The solution consisted of the organic-inorganic polyether diamine-silicate (PEDS) material was allowed to cool to room temperature prior to 60 seconds of wet ozonolysis. The synthesis procedure of the PEDS base material is shown in **Figure 6.2**. Wet ozonolysis was carried out using an AC Faradayozone – high concentration ozone generator (L10G). 10 psi of high purity oxygen (contained in a 10 L cylinder) obtained from SOXAL, Singapore was converted into ozone (ozone flow was limited to 0.5 litres per minute). After wet ozonolysis, PEGMA was added to the ozonolyzed mixture and stirred at 70 °C for 24 hours to facilitate PEGMA grafting.

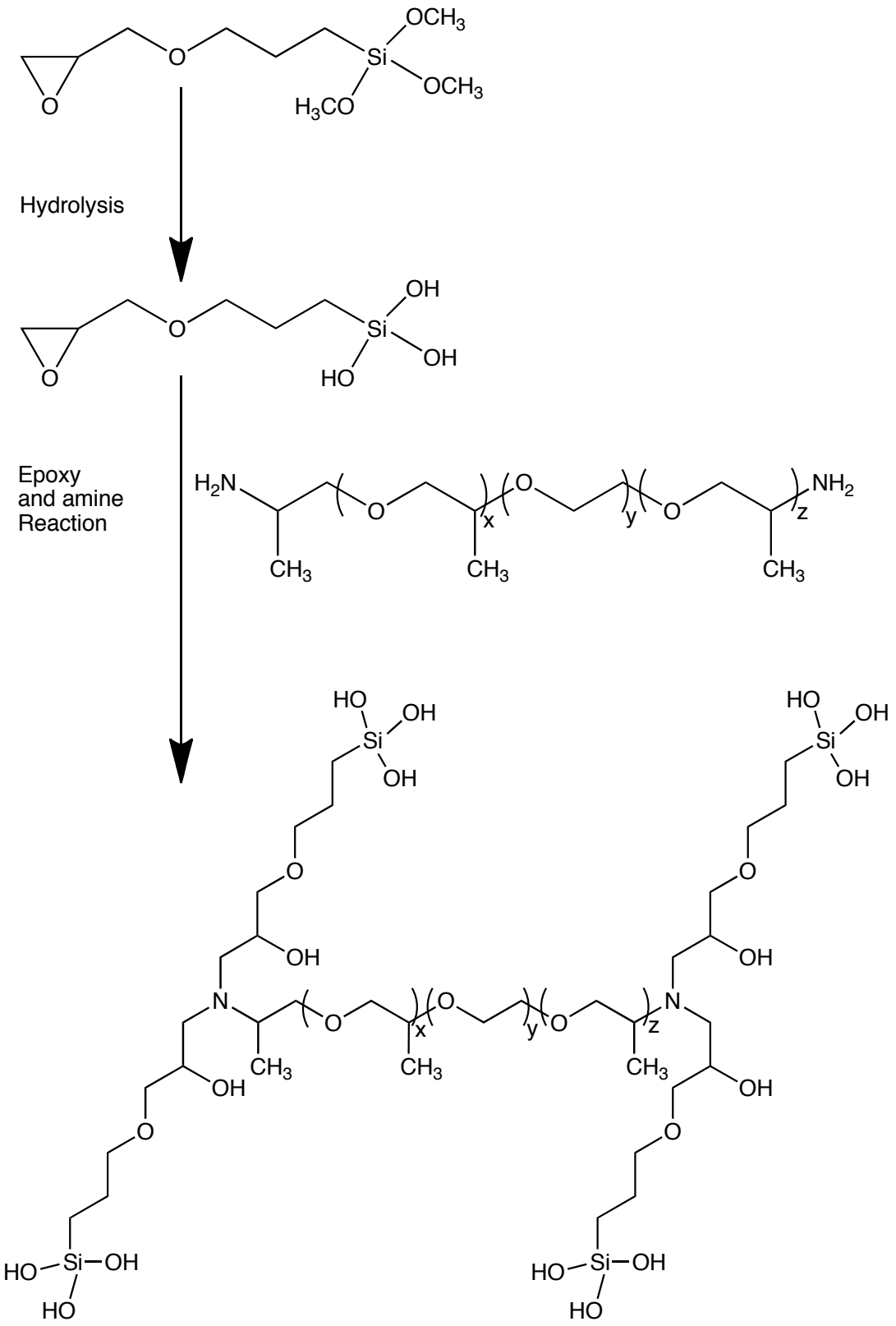

Figure 6.2 Synthesis route of the polyether diamine-silica (PEDS) base material

6.2.3 Fabrication of organic-inorganic and nanohybrid membranes

The nanohybrid PEDS-PEGMA membranes were fabricated using a slow casting method. After transferring the solution into a Teflon dish, the solvent was evaporated at 30 °C for 24 hours. Subsequently, the temperature was raised to 40 °C for further evaporation. Nascent films were peeled off and dried at 70 °C for 24 hours to remove residual solvent whilst undergoing full condensation. Prior to characterization, all membranes were immersed in deionized water for 5 days to remove unreacted monomers. The deionized water was changed everyday. These nanohybrid membranes were stored in a dry box with 27 % humidity at 25 °C prior to testing and characterization.

6.2.4 Characterization of organic-inorganic and nanohybrid materials

The chemical structures of the organic-inorganic and nanohybrid membranes were characterized using solid-state ^{29}Si and ^{13}C NMR. HRTEM and STEM were used to observe the morphology and dispersion of the inorganic nanostructures in the membrane materials. EDX analysis was carried out to determine the elemental composition of the inorganic nanostructures. Bulk PALS at different CO_2 pressures and temperatures were used to characterize the relative fraction free volume (FFV) content in the organic-inorganic and nanohybrid materials.

The pure gas (H_2 and CO_2) permeability was determined by the constant volume-variable pressure method discussed in Section 3.9.1. Additionally, water vapor-saturated pure gas permeation tests were also conducted to observe the effects of water vapor on gas permeation. In this part, the gas bubbles through water prior to feeding. The relative humidity of the permeating gas is detected using a Vaisala HMT330 transmitter and calculated using the Vaisala Veriteg vLog software. Relative gas humidity is about 90 %. For mixed gas permeability tests (as detailed in Section 3.9.2), a mixed gas mixture containing x-mol. % of H_2 in CO_2 was used as the feed gas mixtures and the measurements were conducted at 35 °C with a CO_2 partial pressure of 3.5 atm. The molar concentrations of H_2 tested in this work were 50 mol.%, 40 mol.%, and 10 mol.%. Carbon dioxide sorption tests were conducted using a Cahn D200 microbalance sorption cell at 35 °C over a pressure range of 0-250 psi (0-17.24 bar). Subsequently, CO_2 diffusivity coefficients were calculated using Equation 3.2.

6.3 Results and Discussion

6.3.1 Chemical structures of working materials

Following detailed procedures from Shao and Chungs' work [29], together with wet ozonolysis, CH_x sites in the base PEDS organic-inorganic material can be converted into peroxide moieties [143]. Subsequently, PEGMA is grafted onto the ozone-modified base PEDS organic-inorganic material via free radicals, produced by the thermal decomposition of the peroxide moieties, initiating a propagation reaction that increases the side-chain length as shown in **Figure 6.3**. Unreacted PEGMA is leached from the resultant product that is subsequently dried at 70 °C under vacuum for 24 hours. The PEGMA graft content is determined by comparing the weight of the membranes before and after washing. Results indicate that 11, 15, and 20 wt.% of PEGMA is grafted onto the base materials when 27, 33 and 43 wt.% of PEGMA is initially added to the solution mixture consisting of 80 wt.% PPO-PEO-PPO diamine and 20 wt.% epoxysilane. Throughout this chapter, the terminology "PEDS-PXX" refers to organic-inorganic materials comprising XX wt.% of PEGMA (with respect to the total amount of the base material) grafted onto a PEDS base material comprising 80 wt.% PPO-PEO-PPO diamine and 20 wt.% GOTMS.

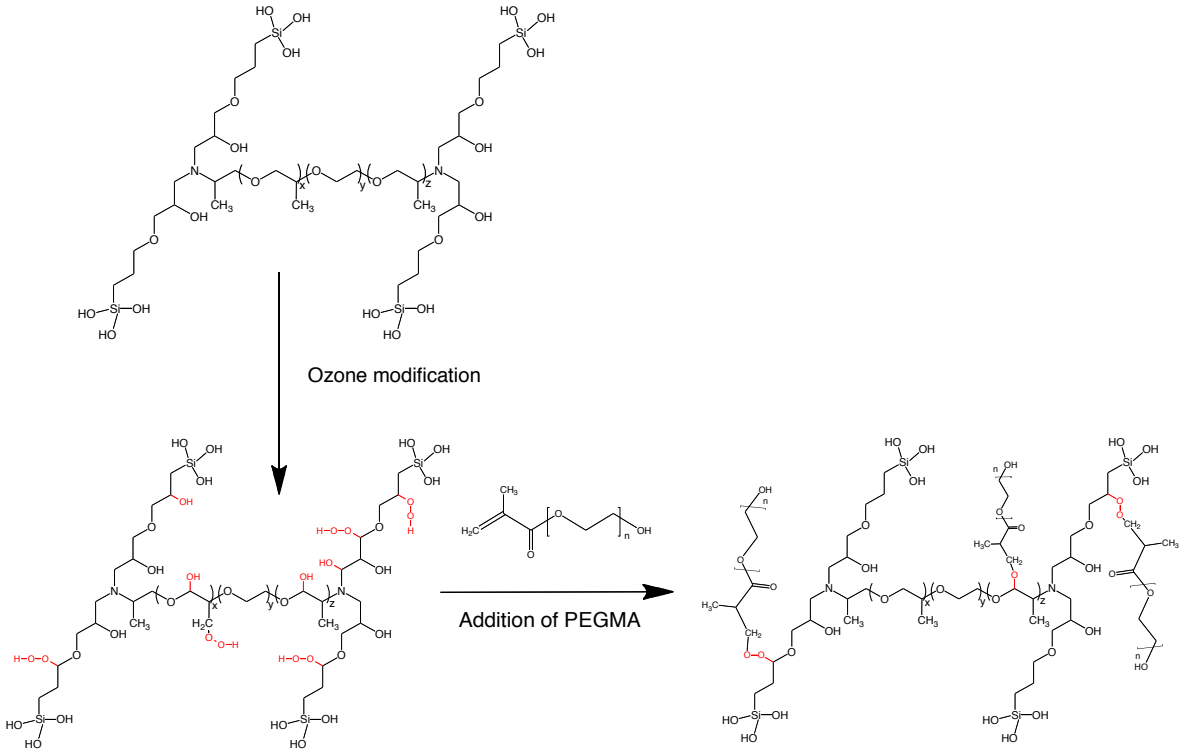

Figure 6.3 Chemical reaction scheme for grafting PEGMA side chains onto the main PEDS chains.

The ^{13}C NMR spectra in **Figure 6.4** validate the presence of PEGMA grafts in these nanohybrid membranes. By comparing the ^{13}C NMR spectra of PEDS-P00 (Figure 6.4(a)) and PEDS-P20 (Figure 6.4(b)), peaks belonging to the CH (δ = 55.05 ppm) and CH_3 (δ = 9.58 ppm) moiety of PPO [117] resonate to lower δ values at δ = 54.49 ppm and 8.92 ppm upon ozonolysis and the addition of PEGMA. Additionally, a peak (δ = 51 ppm) correlating to an OCOR terminal group is observed in the ^{13}C NMR spectrum of PEDS-P20 [117]. This ascertains the grafting of PEGMA onto the main PEDS chains. The absence of

peaks corresponding to C=C (between δ = 115 - 140 ppm) [117] indicates that unreacted PEGMA is successfully removed from the nanohybrid membranes.

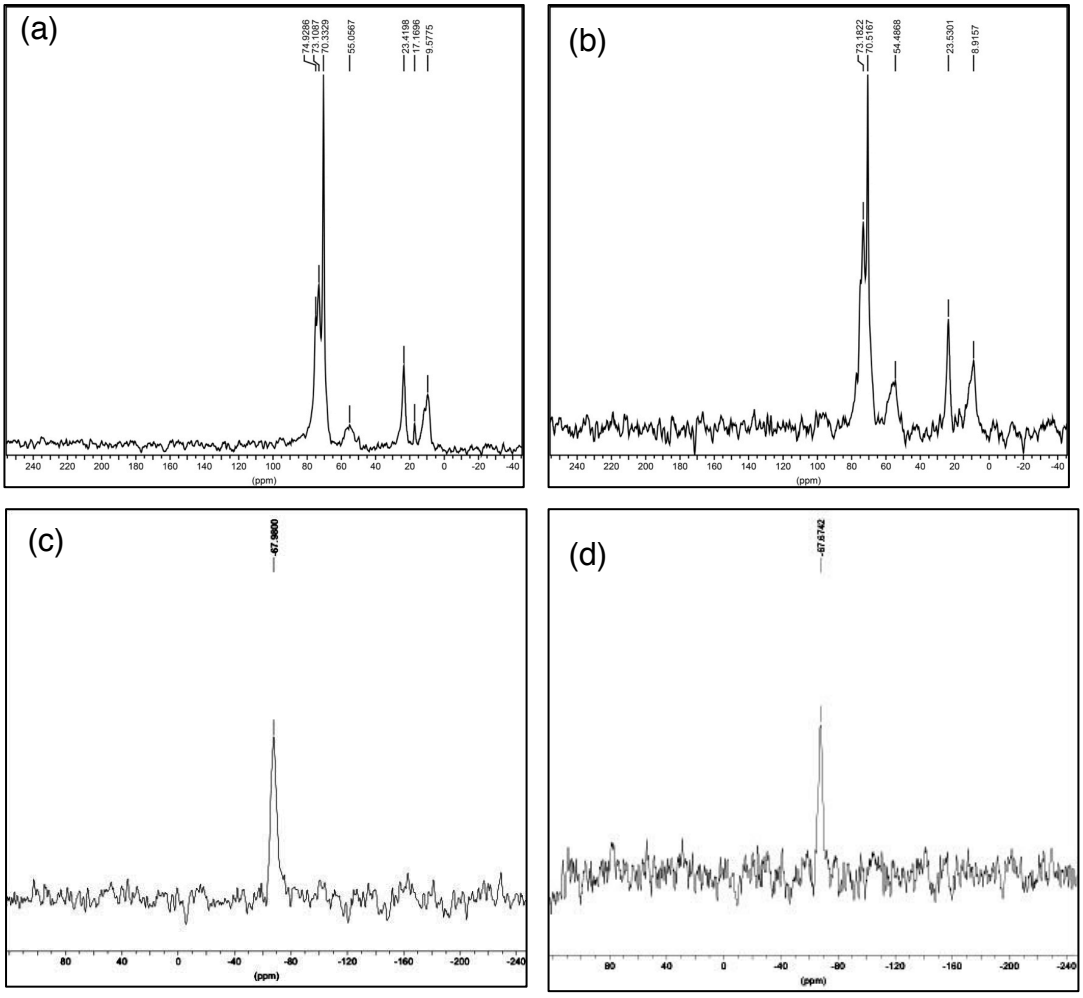

Figure 6.4 Solid-state ^{13}C NMR spectra of (a) PEDS-P00, (b) PEDS-P20, and ^{29}Si NMR spectra of (c) PEDS-P00, (d) PEDS-P20.

The inorganic networks in the PEDS-based organic-inorganic and nanohybrid materials have the same chemical composition as confirmed by ^{29}Si solid-state NMR. The ^{29}Si NMR spectra of PEDS-P00 and PEDS-P20 show a peak (δ = -

67 ppm) that correlates to T^3 resonances arising from fully condensed silicons (**Figure 6.5**), indicating complete condensation of GOTMS [94, 141].

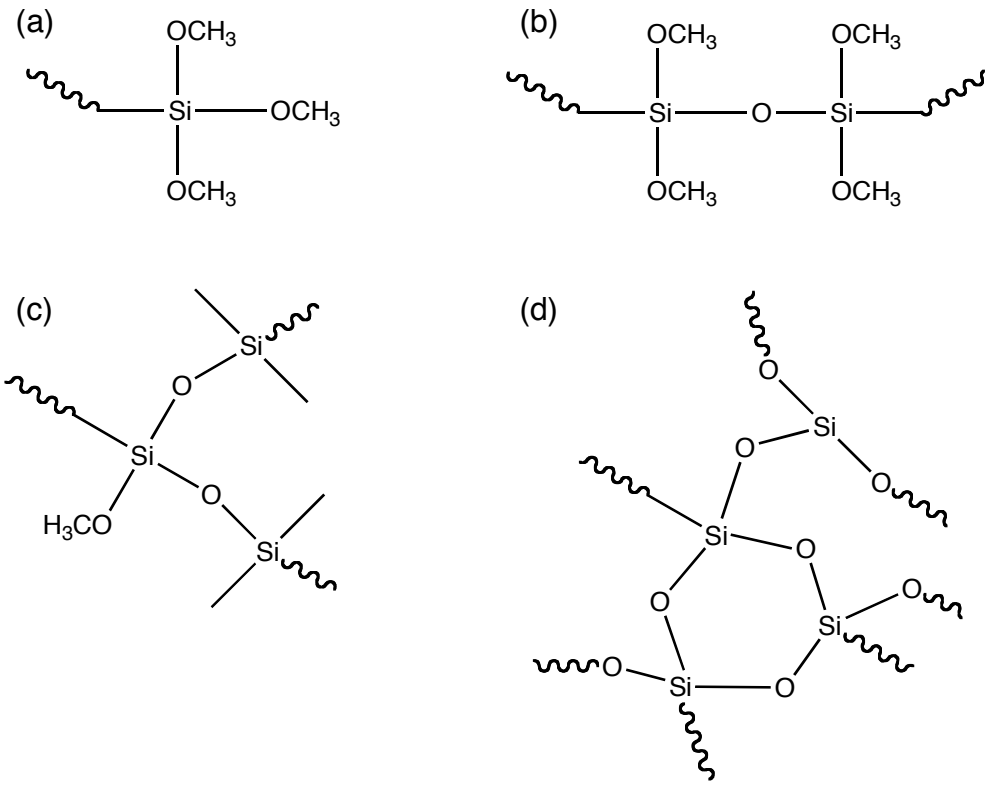

Figure 6.5 Different condensation states of silicon atoms (a) T^0 – no siloxane bonds (peaks of resonance ~ - 42 ppm), (b) T^1- 1 siloxane bond with 2 ethoxy or methoxy groups (peaks of resonance ~ - 53 ppm), (c) T^2 – 2 siloxane bonds with 1 ethoxy or methoxy group (peaks of resonance ~ - 59 ppm), (d) T^3 – 3 siloxane bonds (peaks of resonance ~ - 67 ppm) [94, 144].

6.3.2 Fractional free volume content of working materials

The free volume (V_f) and relative fractional free volume (FFV) contents of PEDS-PXX materials are elucidated using bulk PALS. The V_f radii size distribution correlates to the lifetime (τ_3 in ns) of ortho-positroniums (*o*-Ps) while

o-Ps intensity (I_3 in %) correlates to *o*-Ps formation i.e. V_f content [44, 75, 145]. The V_f radii distributions of PEDS-P00, PEDS-P15, and PEDS-P20 nanohybrid membranes at 35 ºC are shown in **Figure 6.6**. Compared to PEDS-P00 membranes, all PEGMA-grafted nanohybrid membranes display higher FFV content. PEGMA grafts of up to 15 wt.% increase I_3 and τ_3 values of PEDS materials while 20 wt.% of PEGMA grafts slightly reduce I_3 and τ_3 values of PEDS-materials. These observations are similar to the work of Dlubek et al. [146], whereby the hole content and hole size in an alkyl-branched polypropylene material are dependent on branch length and concentration. In the case of PEDS-P15 materials (short branches at multiple sites), the increments in I_3 and τ_3 values denote enhanced hole content, which are slightly bigger in size [146]. The PEGMA side chains may sterically hinder effective packing between the main PEDS chains resulting in higher hole content [146]. Meanwhile in the case of PEDS-P20 materials, we may assume that the branches are longer due to the reaction scheme shown in Figure 6.3. Longer branches may improve the molecular packing of the main chains, thus potentially reducing hole content and size [146].

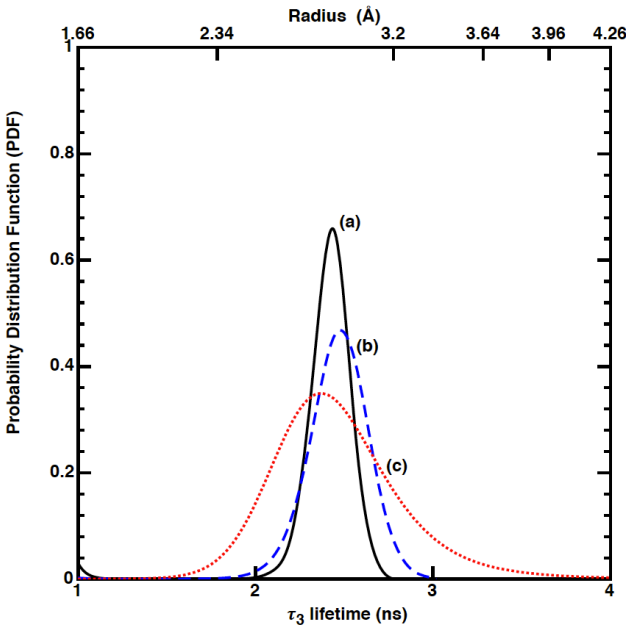

Figure 6.6 Distribution of free volume radius in PEDS-Pxx nanohybrid materials. (a) PEDS-P00 (black), (b) PEDS-P15 (blue), and (c) PEDS-P20 (red).

In **Figure 6.7**, the lower hole content at temperatures ranging from - 100 ºC to - 20 ºC is ascribed to severe inhibitions on polymer chain mobility; while the higher hole content at higher temperatures between 0 ºC to 80 ºC is attributed to enhanced chain mobility [145]. A glass transition temperature (T_g) characterized by the intersection point of the high and low temperature regions is also observed in Figure 6.7. The low T_gs of these materials indicate that these materials are amorphous at room temperature. Compared to Shao and Chung's DSC data [29], T_g measured using PALS in the current work is significantly lower. Longer measurement times (approximately tens of minutes) in PALS allowed polymer chains to further relax during measurement when compared to the shorter measurement times in DSC, thus the T_g measured by PALS is lower.

The hole content and V_f size at different temperatures is important as these data could be used to predict the gas transport and separation performance of these nanohybrid membranes. Lower hole content and smaller V_f size at lower temperatures would yield low gas permeability but high gas permselectivity; whereas at higher temperatures, higher hole content alongside larger V_f sizes yield high gas permeability with low gas permselectivity. Using the I_3 and τ_3 values, the relative free fractional volume (FFV) content of these materials are estimated by $AV_f I_3$, whereby A is an empirical constant and $V_f = 4\pi R^3/3$ [145].

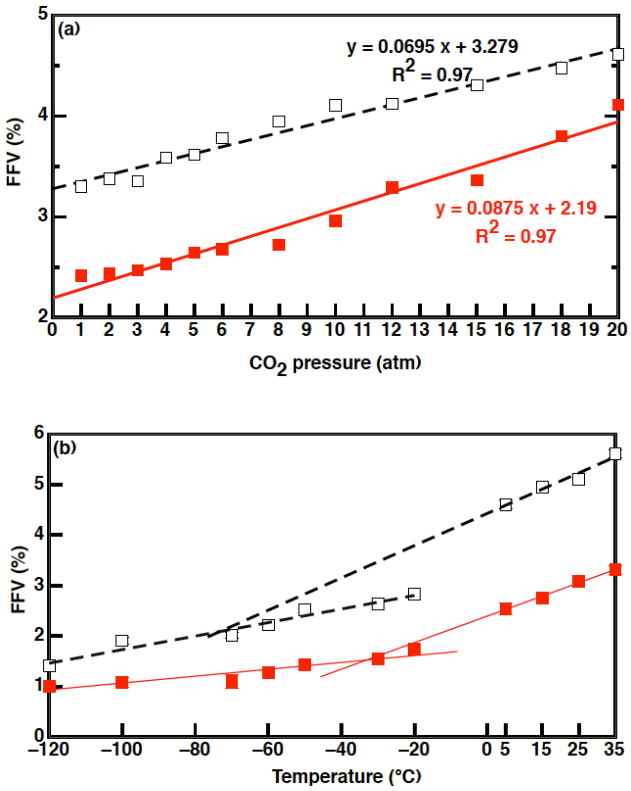

Figure 6.7 FFV content of PEDS-P00 (solid) and PEDS-P20 (empty) materials at (a) different CO_2 pressures and (b) different temperatures.

The penetrant diffusion coefficient of a material increases as a function of relative FFV content. A linear relationship between CO_2 pressure (up to 20 atm) and relative FFV content indicate that CO_2 sorption in PEDS-P00 and PEDS-P20 materials obey Henry's law, whereby CO_2 sorption occurs via the swelling of existing free volume or the creation of new CO_2 sorption sites. The trends observed in I_3 and τ_3 values as a function of PEGMA content are also observed in PEDS-P00 and PEDS-P20 materials. In PEDS-P20, longer hydroxyl (OH)-terminated PEGMA chains increase the tendency to form hydrogen bonds with neighboring ether moieties in PEDS main-chains or PEGMA side-chains, thus further reducing chain mobility that consequently reduces free volume content [75]. Another reason that could attribute to lower FFV content in PEDS-P20 materials is the reduced hole content and V_f size, resulting from improved main chain packing [146]. Although FFV content in PEDS-P20 membranes is lower than that of PEDS-P15 membranes, the CO_2 permeability of a PEDS-P20 membrane is the highest amongst other PEGMA-grafted PEDS membranes.

6.3.3 Dispersion of inorganic silicates in polyether matrix

HRTEM images in **Figure 6.8** reveal crystalline nanostructures within an amorphous matrix. EDX analyses indicate that these nanostructures are primarily made up of silicon and oxygen.

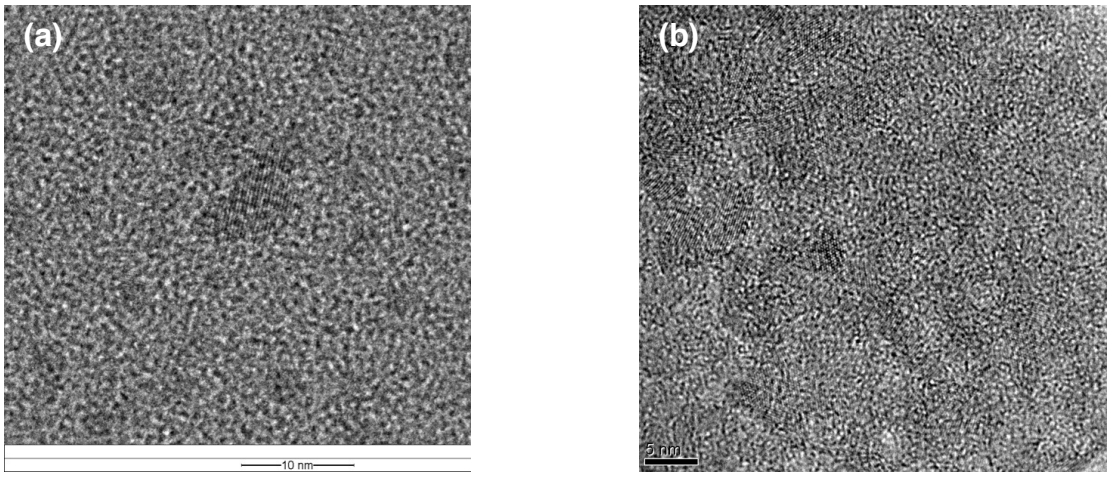

Figure 6.8 HRTEM images of (a) PEDS-P00 material and (b) PEDS-P20 material

STEM images in **Figure 6.9** provide clearer images of the distribution of these silicate nanostructures. The well-defined silicate nanostructures in PEDS-P00 organic-inorganic material range from 5 - 10 nm in diameter sizes while bigger silicate nanostructures ranging from 40 - 100 nm are observed in PEDS-P20 nanohybrid materials. The size increment in silicate nanostructures can be ascribed to the change in H_2O/Si ratio (R-ratio) in the sol-gel process during synthesis [96]. Unreacted PEGMA additives in the synthesis solution of PEDS-P20 can form hydrogen bonds with water, thus reducing the R-ratio value that subsequently induces roughness in the larger inorganic nanoparticles [96]. It is important to note that additional PEGMA causes only structural changes to the inorganic network while maintaining chemical composition integrity, as evidenced by ^{29}Si solid-state NMR.

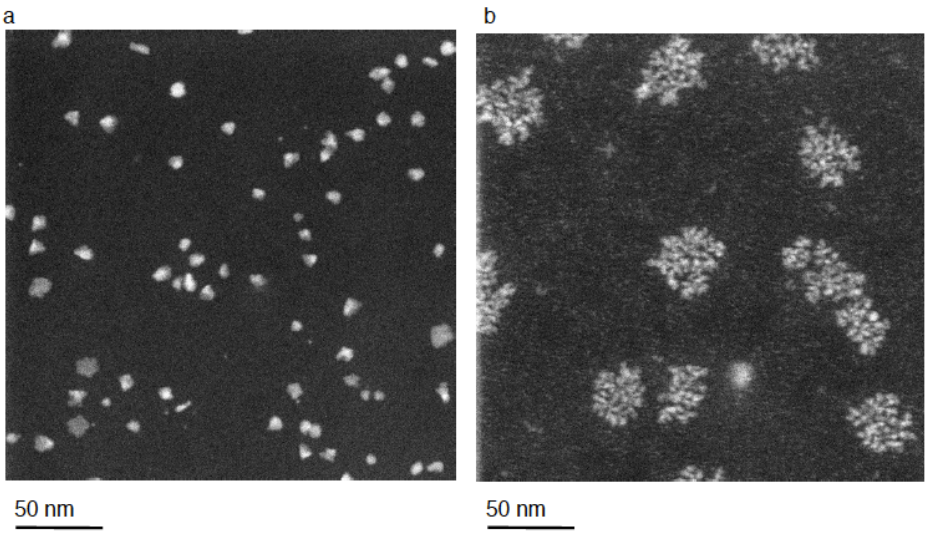

Figure 6.9 HAADF-STEM images of (a) PEDS-P00 and (b) PEDS-P20 membranes.

6.3.4 Gas permeability and permselectivity of nanohybrid membranes

Figure 6.10 shows that the ideal CO_2 and H_2 permeabilities of the PEDS-P20 nanohybrid membrane can reach 1,950 Barrer and 185 Barrer, respectively, with an ideal CO_2/H_2 selectivity of 11. Compared to PEDS-P00 membranes, ideal CO_2 and H_2 permeability coefficients are augmented by 5.2 and 4.7 fold, respectively. The larger increment in ideal CO_2 permeability causes the CO_2/H_2 selectivity to increase from 9 to 11. Compared to highly amorphous PEO-based CO_2 selective membranes [24, 81, 86, 147], the nanohybrid membranes studied in this thesis possess better CO_2 transport properties with lower EO content. This indicates that contributions from the inorganic silicate phase are more significant than the organic polyether phase. Ideal CO_2 permeability subtly increases with increasing CO_2 pressure (from 2 to 20 atm). At 3.5 atm, the effects of plasticization are negligible in these nanohybrid membranes. The

mixed gas permeation properties of these nanohybrid membranes are determined using different mixed gases comprising 50 mol.% CO_2: 50 mol.% H_2, 60 mol.% CO_2: 40 mol.% H_2, and 90 mol.% CO_2: 10 mol.% H_2. The CO_2 permeability of a PEDS-P20 nanohybrid membrane can reach 1990 Barrer with a CO_2/H_2 selectivity of 11. The mixed and ideal gas permeation tests results are identical.

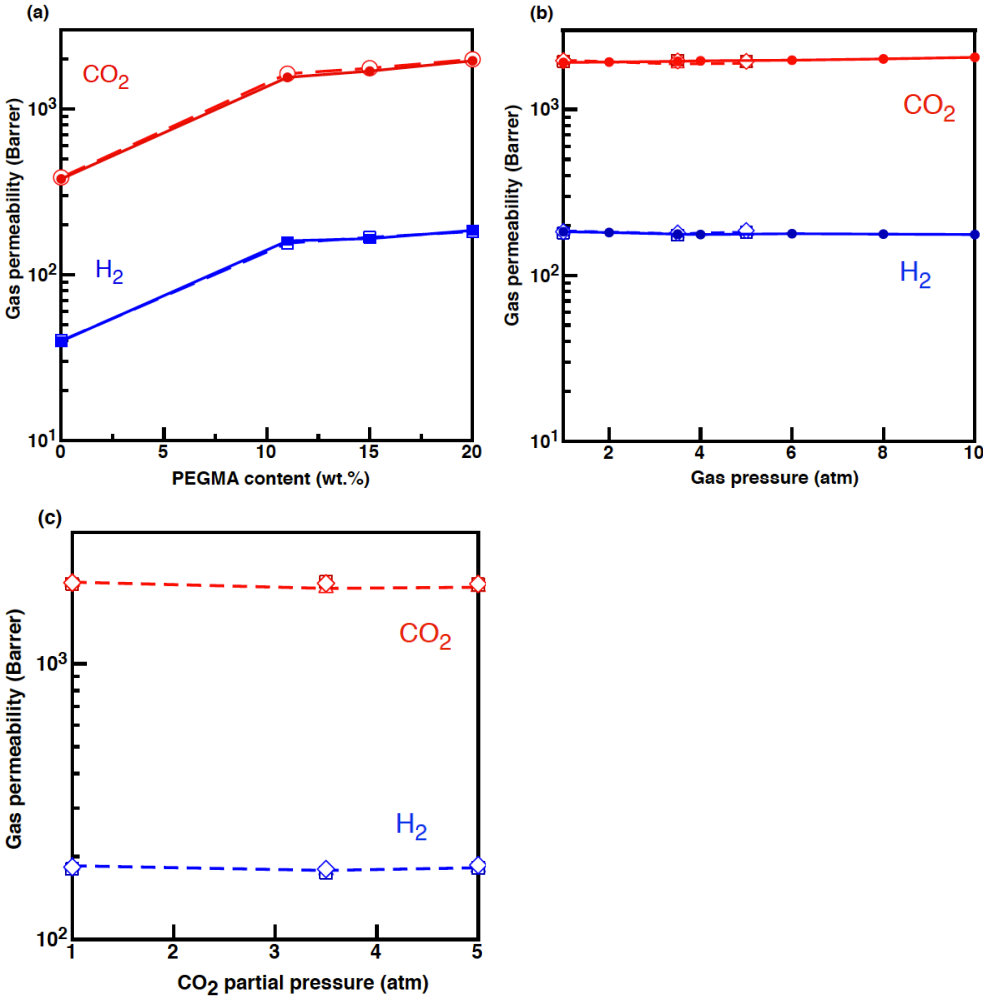

Figure 6.10 (a) Comparison between pure gas permeability(● - CO_2, ■ - H_2) and mixed gas permeability (○- CO_2, □ - H_2) of PEGMA-grafted PEDS membranes with different PEGMA graft content. All gas permeation tests are tested at 35 °C, while ideal gas pressures and CO_2 partial pressures are maintained at 3.5 atm. (b) Comparison of pure gas permeability and mixed gas permeability of

PEDS-P20 nanohybrid membrane at different total gas pressures. (c) The effects of 1, 3.5 and 5 atm of CO_2 partial pressures using mixed gases with different feed compositions on a PEDS-P20 membrane. Mixed gas feed compositions (CO_2 mol.%: H_2 mol.%) are represented by □(50:50), △(60:40), and ♢(90:10). Uncertainty in permeability measurements is ± 10%. The lines are provided to guide the eye.

6.3.5 Effects of water vapor on gas permeation

To mimic industrial CO_2/H_2 separation (whereby water vapor is present), primary studies on the effects of water vapor on pure CO_2 and H_2 permeation and CO_2/H_2 separation reveal that H_2 permeation is reduced (**Figure 6.11**), resulting an increase in CO_2/H_2 selectivity. Although Brands et al. attributed the decrease in H_2 permeability to water vapor-induced densification of silica in silica-coated membranes [148], the actual reason behind this phenomenon remains unknown. While the CO_2 transport and separation properties in PEDS-based nanohybrid membranes have not surpassed the upper bound limit for CO_2/H_2 separation [123], these nanohybrid membranes represent a tremendous improvement from current state-of-the-art membranes. Besides larger FFV content, the significant gas separation performance observed in alkyl methacrylate grafted PEDS materials can be ascribed to the crucial enhancement in CO_2 solubility coefficients caused by the CO_2- affinity of the inorganic silicate phases.

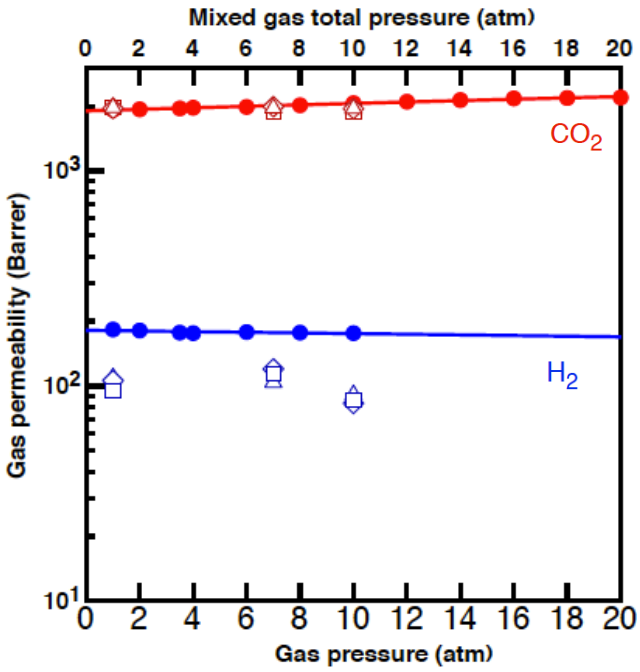

Figure 6.11 A comparison of pure gas permeabilities and mixed gas permeabilities of PEDS-P20 nanohybrid membrane at different gas pressures in the presence of water vapor**.** Red symbols represent CO_2 permeability while blue symbols represent H_2 permeability. Mixed gas feed compositions (CO_2 mol.%: H_2 mol.%) are represented by □(50:50), △(60:40), and ♢(90:10).

6.3.6 Sorption isotherms of working materials

The concentration of alkyl methacrylate added during synthesis strongly influences the CO_2 solubility (S_{CO_2}) and diffusivity (D_{CO_2}) coefficients of these nanohybrid membranes. CO_2 solubility coefficients calculated from sorption isotherms of PEDS-based membranes shown in **Figure 6.12** indicate that S_{CO_2} increases as a function of PEGMA content. **Table 6.1** shows that the activation energy of CO_2 permeation $(E_P)_{CO_2}$ decreases as the content of PEGMA increases. It can be argued as follows that the trends in S_{CO_2} and in $(E_P)_{CO_2}$ are related. The activation energy for permeation is the sum of the activation

energy of diffusion and the enthalpy of sorption of the gas in the polymer; the latter consists of the enthalpy of condensation of the gas plus the enthalpy of mixing gas and polymer. Increasing the content of units with good CO_2 affinity i.e. EO units and siloxane units enhances the interaction of CO_2 with the polymer; this means a more negative heat of mixing of CO_2 with the polymer and, thus, a lower activation energy of permeation for CO_2.

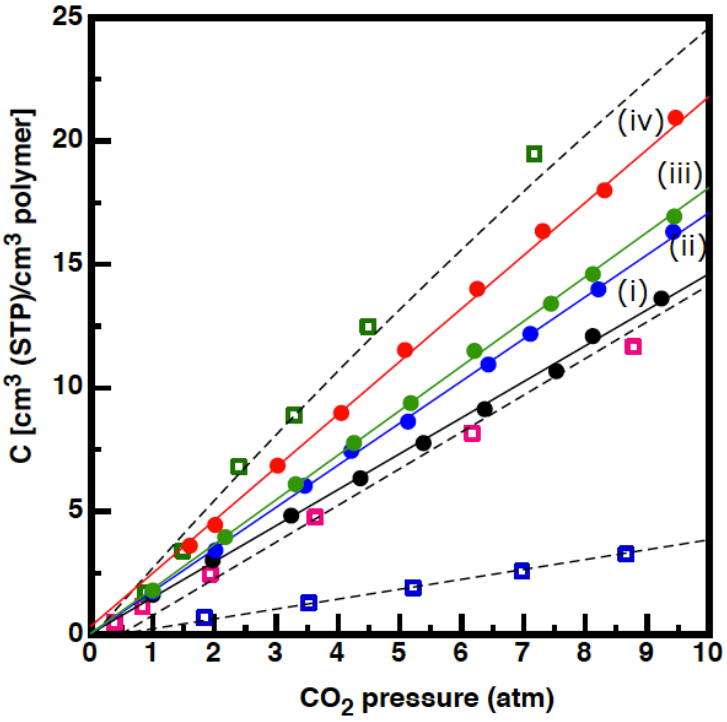

Figure 6.12 CO_2 sorption isotherms of (i) PEDS-P00, (ii) PEDS-P11, (iii) PEDS-P15, and (iv) PEDS-P20. The solid dots represent experimental data while the empty squares refer to theoretical S_{CO_2} coefficients of □ - semi-crystalline PEO [77, 149], □ – PDMS [38], and □ – PTMSP [150]. Solubility coefficients are measured in cm^3(STP)/cm^3 polymer atm.

Table 6.1 Ideal CO_2 permeability, solubility and diffusivity coefficients of PEDS-based nanohybrid membranes, semi-crystalline cross-linked PEO [77, 149], PDMS [38], and – PTMSP [150]. Diffusivity coefficients are measured in cm^2/s.

	P_{CO_2} (Barrer)	S_{CO_2} (cm^3STP/ cm^3. atm)	D_{CO_2} (10^{-6} cm^2/s)	$E_{P\,CO_2}$ (kJ/mol)	α_{CO_2/H_2}
PEDS-P00	378	1.5	1.92	22.4 ± 0.28	9.5
PEDS-P11	1550	1.7	6.92	13.4 ± 0.45	9.69
PEDS-P15	1690	1.8	7.14	11.9 ± 0.32	10.24
PEDS-P20	1950	2.3	6.44	10.5 ± 0.22	10.54
Semi-crystalline PEO [77, 149]	300	1.6	1.43	21 - 23.45	9.4
PDMS [38]	3800	1.3	22.21	-	3.1
PTMSP [150]	28000	3.9	54.56	-	1.3

Interestingly, the sorption isotherms of PEDS-P00 and PEDS-P20 membranes closely resemble the sorption isotherms of polydimethylsiloxane (PDMS) and poly (1-trimethylsilyl-1-propyne) (PTMSP), respectively. The solubility coefficients of PEDS-based membranes can be described as a summation of all the contributions of individual components; namely, the amorphous polyether (organic phase), the silicate inorganic network, and the amorphous PEGMA

grafts. Based on the composition of PPO-PEO-PPO diamines (80 wt.%) and epoxysilanes (20 wt.%) in PEDS-P00 membranes, the theoretical S_{CO_2} coefficient may be calculated using the solubility coefficients of amorphous PEO (A-PEO) [149], PDMS [38], PTMSP [150], and the following equation:

S_{CO_2} of PEDS-PXX = (1-x) [0.8 (S_{CO_2} A-PEO) + 0.2 (S_{CO_2} PDMS or PTMSP)] + x (S_{CO_2} A-PEO) whereby x = amount of grafted PEGMA **Equation 6.1**

The theoretical (1.54 cm^3.STP/ cm^3.atm) and experimental S_{CO_2} coefficients of the PEDS-P00 organic-inorganic membrane (1.5 cm^3.STP/ cm^3.atm) are very close when the S_{CO_2} coefficient of PDMS is used. The inorganic phase of a PEDS-P00 nanohybrid membrane behaves like a PDMS network that consists of Si-O bonds. The high CO_2 affinity of Si-O bonds [151] that are present in PEDS-P00 nanohybrid membranes yields a higher S_{CO_2} coefficient when compared to amorphous, cross-linked PEO rubbers [75]. In the case of PEDS-P11 and PEDS-P15 nanohybrid membranes, the identical experimental and theoretical S_{CO_2} coefficients also indicate that inorganic networks in these nanohybrid membranes possess PDMS-like CO_2 sorption capabilities. For a PEDS-P20 nanohybrid membrane, the calculated theoretical S_{CO_2} coefficient is very close to the experimental value when the CO_2 solubility coefficient of PTMSP [150] is used. The difference in solubility contributions is due to

structural differences (caused by different R-ratios in the sol-gel processes) in the silicate-based networks that affect the interaction between CO_2 penetrant and CO_2-philic moieties like Si-O moieties and ether oxygen units.

6.4 Summary

CO_2 permeability and CO_2/H_2 selectivity enhancements in PEGMA-grafted PEDS materials can be ascribed to markedly improved D_{CO_2} and S_{CO_2} coefficients. The presence of non-reactive additives in the pre-synthesis mixture solutions induced structural changes in the inorganic phases. The ultra-high CO_2 permeability and gas selectivity of these nanohybrid membranes render this material exceptionally effective in facilitating a low-cost, clean technique for industrial-scale H_2 purification while performing CO_2 capture. Moreover, preliminary studies indicate that the CO_2/H_2 selectivity of these nanohybrid membranes is further enhanced in the presence of water vapor. Large-scale utilization of this material for CO_2/H_2 separation can positively contribute huge economical savings based on the elimination of H_2 recompression. Moreover, these materials are able to effectively purify H_2 from syngas feeds that contain up to 50% CO_2. These materials can also be used for CO_2 removal in flue gas.

Although a superior membrane material has been fabricated, the effects of different synthesis conditions and parameters on the CO_2 transport and gas separation performance of this material remain unknown. It is of interest to

elucidate the factors that determine the gas separation properties of this membrane material. The next chapter will focus on tuning the gas separation performance of this membrane material by varying the organic-inorganic ratio, the graft type, and the nature of material modification.

CHAPTER SEVEN:

EFFECT OF SILICATE AGGLOMERATIONS ON THE GAS TRANSPORT AND SEPARATION PROPERTIES OF ORGANIC-INORGANIC MATERIALS

7.1 Introduction to material hybridization

The inherent gas transportation and separation capabilities of polymeric membranes can be attuned via material designing. Chen et al. designed block copolymers consisting of polyimides and polyethylene oxide (PEO) [152]. This combination harnesses the advantages of both materials, namely, mechanical strength of polyimides and high CO_2 affinity of PEO resulting from dipole-quadrupole interactions between acidic CO_2 and polar ether oxygen units. The gas transportation and separation capabilities of these block copolymers depend on the interaction between the PEO and polyimide content. Alternative to PEO-based block copolymers, Patel et al. cross-linked a series of low molecular weight polyether-acrylate monomers to form CO_2-philic gas separation membranes [25]. The CO_2 permeability of Patel's membranes reached 83 Barrer with a CO_2/H_2 selectivity of 11. Meanwhile, Lin et al. reported the cross-linking of low M_w PEO-methacrylates that forms a rubbery membrane material with a CO_2 permeability of 400 Barrer and a CO_2/H_2 selectivity of 10 [24]. The methyl moiety enhanced the FFV content in Lin's rubbery membranes, thus the increased CO_2 permeability when compared to Patel's membranes.

In these cases, higher FFV content and enhanced interaction between membrane material and gas penetrant i.e. CO_2, significantly enhance gas penetrant permeability i.e. enhancements in both diffusivity and solubility

coefficients are required to increase CO_2 permeability. Incorporating nanoparticles into an organic polymer matrix to form nanocomposites can enhance diffusivity coefficients. Merkel et al. and Patel el al. incorporated fumed silica (FS) nanoparticles into poly (4-methyl-2-pentyne) (PMP) [28] and cross-linked diacrylate-terminated PEG [153], respectively. In Merkel's work, PALS and pulse field gradient NMR data show that silica nanoparticles improve the inter-connectivity between larger concentrations of large free-volume elements. Hill's quantitative theoretical model captures the correct dependence of gas permeability of polymeric nanocomposites on nanoparticle size and free volume content that explains the reverse-selectivity observed in Merkel's work [154].

In Patel's work, the enhanced free volume content is attributed to pore size increments in the inorganic nanoparticles [155] and extra free volume content at the polymer-nanoparticle interface [154]. Nanoparticles also strengthen the mechanical properties of membranes and suppress polymer crystallinity. The CO_2 transportation and separation capability of Merkel and Patel's membranes and the validity of Hill's theory rely on the fine dispersion of nanoparticles in the polymeric matrix i.e. nanoparticle agglomeration is detrimental for gas permeability and separation. The *in situ* synthesis of inorganic nanoparticles in a polymeric matrix can overcome agglomeration imparted by the incorporation of ready-made nanoparticles.

Organic-inorganic materials can be synthesized using an acid-catalyzed sol-gel process [29, 94, 96]. In such processes, the dispersion and growth of the inorganic nanostructures are controlled by the reaction kinetics of the sol-gel process. The pioneering works by Sforça et al. [94] and Shao and Chung [29] did not investigate the relationship between the dispersion of inorganic nanostructures and CO_2 transport in these nanohybrid materials. However, Shao and Chung primarily attributed the mechanical stability in their membranes to the inorganic nanostructures [29]. Meanwhile, findings from Chapter 6 of this dissertation clearly demonstrate that the inorganic phase enhances the CO_2 sorption capability of nanohybrid membranes and consequently increases CO_2 permeability. Little work has been done to elucidate the relationship between the dispersion and morphology of the silicate nanostructures and CO_2 permeability and permselectivity.

In this chapter, silicate growth and dispersion, and CO_2 permeability is studied as a function of organic-inorganic ratio (that also affects water/silicon ratio) and modification type. PEDS base materials were modified via short alkyl side chain grafts and physical blending. The size and morphology of the silicate nanostructures determine the CO_2 solubility coefficients of the resulting nanohybrid membrane. Size heterogeneity in the silicate nanostructures correlates to synthesis conditions, presence of additives in the synthesis solutions, and the thermal properties of the resultant nanohybrid membranes.

7.2 Materials and Experimental Methods

7.2.1 Materials

The base PEDS organic-inorganic material was synthesized using the same monomers described in Chapter 6. In this part of the work, butyl methacrylate (BuMA: M_w = 142 g/mole), and PEGMA (M_w = 360 g/mol) were grafted onto the main PEDS chains. The chemical structure of butyl methacrylate (purchased from Sigma Aldrich, Singapore) is shown in **Figure 7.1**. The inhibitors in these alkyl methacrylates were removed using activated carbon and the procedure mentioned in Section 6.2.1.

Butyl methacrylate (BuMA M_w 236 g/mol)

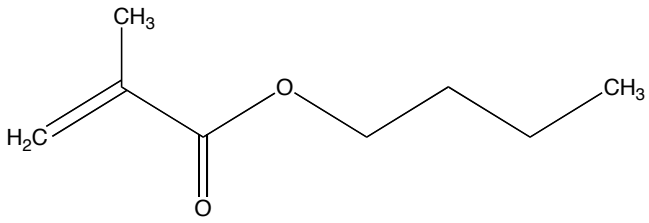

Figure 7.1 Chemical structure of butyl methacrylate

7.2.2 Membrane fabrication

The base organic-inorganic PEDS materials were synthesized using the same method detailed in Section 6.2.2. In this chapter, the organic-inorganic ratios in PEDS base materials were also attuned to 50:50 and 75:25, respectively. This facilitates the investigation of the effects of organic-inorganic ratio on CO_2 permeability and CO_2/H_2 separation. These base materials are coded after their

organic-inorganic ratio, namely, $PED_{75}S_{25}$ and $PED_{50}S_{50}$.

To determine the effects of side-chain functionality on CO_2 permeability, 20 wt.% of BuMA was grafted onto $PED_{50}S_{50}$ and $PED_{75}S_{25}$ materials. The gas transport and separation properties of PEDS membranes containing BuMa grafts were compared to PEGMA-grafted PEDS materials. The organic-inorganic materials with PEGMA (M_w 360) and BuMA grafts are known as $PED_{XX}S_{XX}$-P_{YY}, and $PED_{XX}S_{XX}$-B_{YY}, respectively. YY refers to the wt.% of grafts. The graft concentrations were determined by comparing the weight of the membranes before and after washing. The difference in weight measurements infer to unreacted PEGMA present in the membranes.

7.2.3 Membrane characterization

The chemical structures of the organic-inorganic and nanohybrid membranes were characterized using solid-state ^{29}Si and ^{13}C NMR. STEM was used to observe the morphology and dispersion of the inorganic nanostructures in the membrane materials. EDX analysis was carried out to determine the elemental composition of the inorganic nanostructures. Bulk PALS at different CO_2 pressures and temperatures were used to characterize the relative FFV content in the organic-inorganic and nanohybrid materials. The pure gas permeabilities were determined by the constant volume-variable pressure method discussed in Section 3.9.1. For mixed gas permeability tests (as detailed in Section 3.9.2), a

mixed gas mixture containing x-mol. % of H_2 in CO_2 was used as the feed gas mixtures and the measurements were conducted at 35 °C with a CO_2 partial pressure of 3.5 atm. The molar concentrations of H_2 tested in this part of the dissertation were 50 mol.%, 40 mol.%, and 10 mol.%. Carbon dioxide sorption tests were conducted using a Cahn D200 microbalance sorption cell at 35 °C over a pressure range of 0-250 psi (0-17.24 bar). The CO_2 solubility coefficients were determined from the CO_2 sorption isotherms of these materials. Subsequently, CO_2 diffusivity coefficients were calculated using Equation 3.2 i.e. $D = P/S$.

7.3 Results and discussion

7.3.1 Characterization of Organic-Inorganic Material Structure.

The ideal molar ratio of the base PEDS material is 1:4 whereby each polyether diamine molecule reacts with four molecules of alkoxysilanes i.e. the ideal wt.% ratio is 68 wt.% of polyether to 32 wt.% of alkoxysilanes. The non-stoichiometric molar ratio between the organic polyether diamines and the inorganic alkoxysilanes in a $PED_{75}S_{25}$ membrane results in excess polyether diamines. Hence, in the ^{13}C NMR spectrum of a $PED_{75}S_{25}$ membrane (**Figure 7.2(a)**), the peak at δ = 43.9 ppm correlates to C-N bonds found in $-CH_2NH_2$ moieties [117]. In the case of a $PED_{50}S_{50}$ membrane, the non-ideal molar ratio yields excess inorganic alkoxysilanes. Thus, in the ^{13}C NMR spectrum of a $PED_{50}S_{50}$ membrane, the peak corresponding to a C-Si bond at δ = 79 ppm is more obvious in the ^{13}C NMR spectrum of a $PED_{50}S_{50}$ membrane, indicating the presence of excess alkoxysilanes.

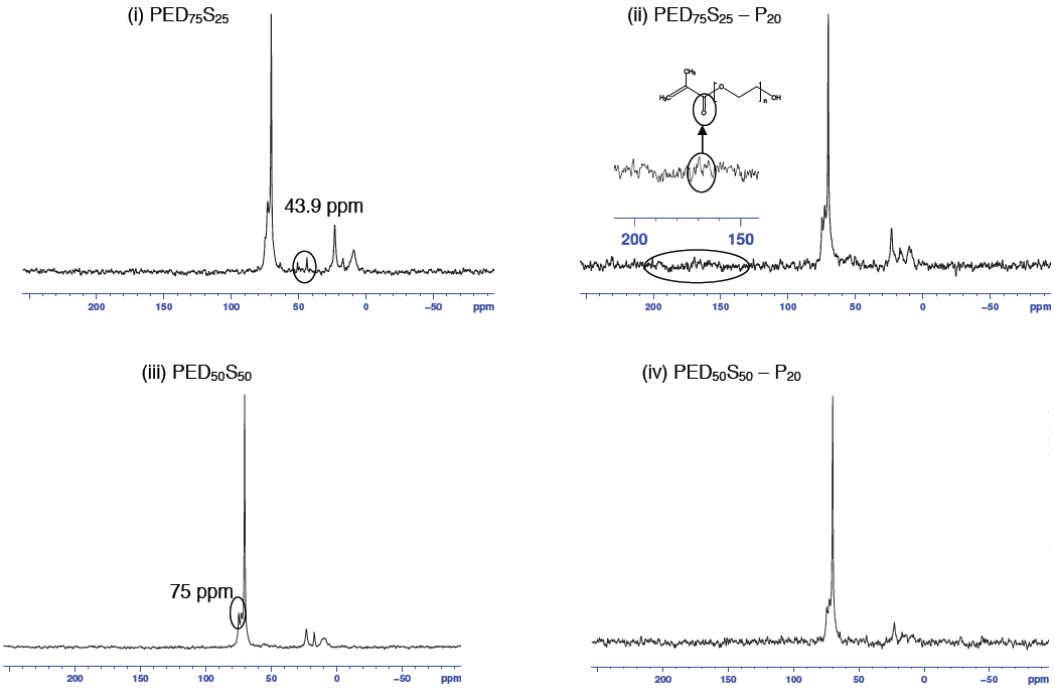

Figure 7.2 (a) ^{13}C solid state NMR spectra of (i) $PED_{75}S_{25}$, (ii) $PED_{75}S_{25}$-P_{20}, (iii) $PED_{50}S_{50}$, and (iv) $PED_{50}S_{50}$-P_{20}

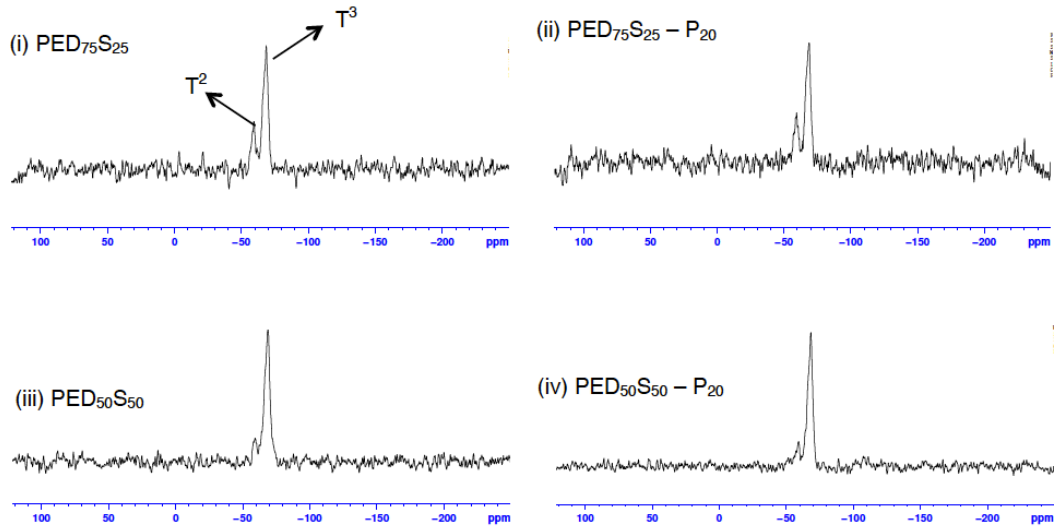

Figure 7.2 (b) ^{29}Si solid state NMR spectra of (i) $PED_{75}S_{25}$, (ii) $PED_{75}S_{25}$-P_{20}, (iii) $PED_{50}S_{50}$, and (iv) $PED_{50}S_{50}$ -P_{20} membrane

In the ^{13}C NMR spectrum of a $PED_{75}S_{25}$-P_{20} membrane, the peak at δ = 170 ppm corresponding to a C=O terminal group [117], validates the presence of PEGMA grafts on the PEDS main chains. Peaks corresponding to C=C (between δ = 115 - 140 ppm) are absent in the PEGMA-grafted nanohybrid membranes i.e. unreacted PEGMA is successfully removed from the nanohybrid membranes after washing. The T^2 and T^3 resonance peaks (δ = -59 ppm and - 67 ppm) in the ^{29} Si solid-state NMR spectra indicate that the inorganic networks in the PEDS-based organic-inorganic materials consist a mixture of silicons that consist of two siloxane and one ethoxy or hydroxyl bonds (T^2) or are fully condensed with three siloxane bonds (T^3) [93, 94] (Refer to Figure 6.5 for graphical depiction).

The C 1s peak at ~ 287 eV corresponds to the carbon atoms in an epoxy ring [156]. This peak is prominent only in the XPS spectra of $PED_{50}S_{50}$ membranes (**Figure 7.3**), validating the presence of excessive epoxysilanes. The excessive epoxysilanes are completely hydrolyzed and condensed into silicons with two or three siloxane bonds. This is evidenced by the absence of T^0, and T^1 peaks in the solid-state ^{29}Si NMR spectra. In the case of $PED_{75}S_{25}$ membranes, all epoxysilanes reacted with polyether diamines hence the C 1s peak that belongs to the C 1s atom of an epoxy ring at 287 eV is not obvious. The peaks between 287 – 288 eV in the XPS spectra of $PED_{50}S_{50}$–P_{20} and $PED_{75}S_{25}$–P_{20} membranes indicate the presence of C=O moieties (present in PEGMA). As

these $PED_{50}S_{50}$–P_{20} and $PED_{75}S_{25}$–P_{20} membranes are characterized after the removal of unreacted PEGMA, the presence of C=O moieties result from the PEGMA grafts in the materials.

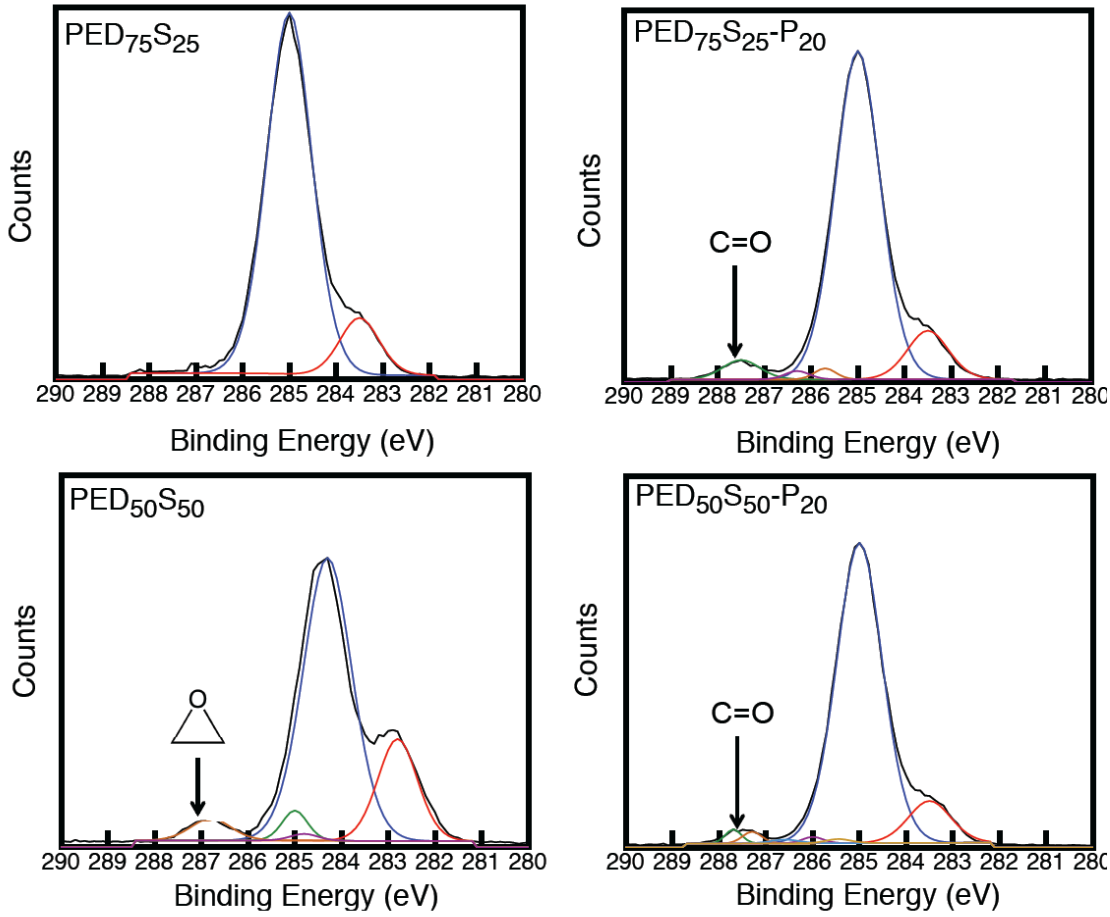

Figure 7.3 XPS spectra of PEDS-based nanohybrid membranes

7.3.2 Morphology of PEDS and PEDS-P_{xx} Organic-Inorganic Materials

The morphology and dispersion of the inorganic phase in organic-inorganic materials synthesized via an acid-catalyzed sol-gel process [29, 94, 96] are controlled by sol-gel reaction kinetics. The sol-gel process involves two

reactions involving the silicon atom as follows [96]:

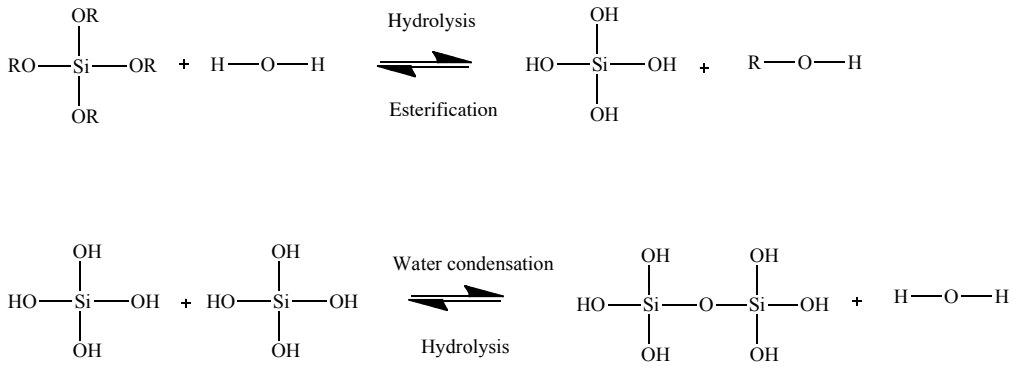

Hydrolysis occurs over a nucleophilic attack by the oxygen in water on the silicon atom. As an acid-catalyzed hydrolysis promotes the protonation of alkoxides in alkoxysilanes, the withdrawal of electron density in the silicon atom makes it more electrophilic and more susceptible to an attack by water. With increased electrophilicity, the water molecule attacks and imparts a positive partial charge to the protonated alkoxides [157]. A subsequent reduction of this partial charge facilitates an alcohol departure from the silicon tetrahedron. Water condensation removes water from the system and minimizes depolymerization, thus resulting in an insoluble three-dimensional siloxane network. When depolymerization is least likely to re-occur, condensation becomes irreversible and the hydrolysis of siloxane bonds after formation is impossible.

Condensation involves a nucleophilic attack on the deprotonated silanol in a

neutral silicate species and is essential for siloxane network development [158]. The siloxane network formation is a sequential product of hydrolysis, condensation, and the reverse reactions and is therefore dependent on the H_2O/Si ratio [96], the organic/inorganic ratio, and the glass transition temperature (T_g) of the organic phase [141].

7.3.3 Effects of different organic/inorganic ratio on gas transport properties of organic-inorganic membranes

In **Table 7.1,** the CO_2 and H_2 permeability, and the S_{CO_2} and D_{CO_2} coefficients of the base organic-inorganic materials increase somewhat with higher polyether content. The CO_2 affinity of the organic-inorganic material is enhanced with higher polyether content as well [149]. The similarities between the S_{CO_2} coefficients of these organic-inorganic membranes and PDMS [159, 160] indicate that the silicate nanostructures also contribute to the high CO_2 affinity in the organic-inorganic materials. However, if the size of the silicate nanostructure becomes too large, CO_2 permeability will be reduced. Hence, it is important to obtain an optimal silicate nanostructure size. Larger CO_2 diffusion coefficients are attributed to higher relative FFV content that is a consequence of higher polyether content and larger silicate nanostructures. The extra methyl group in PPO increases the relative fractional free volume (FFV) content of resultant membranes [161], while the growth mechanism of the inorganic silicate nanostructure, steric and kinetic constraints circumvent

the interpenetration and condensation of inorganic silicon-based nanostructure, leaving spaces in between the clusters of silicate nanostructures [96]. Larger S_{CO_2} and D_{CO_2} coefficients enhance the CO_2 permeability. H_2 permeability enhancements are solely attributed to the increase in relative FFV content.

Table 7.1 Gas permeability, CO_2 diffusivity and solubility coefficients, and gas permselectivity of base organic-inorganic membranes studied in this work.

Sample Code	P_{CO_2} (Barrer)	S_{CO_2} (cm^3.STP/ cm^3. atm)	D_{CO_2} (10^{-6} cm^2/s)	P_{H_2} (Barrer)	CO_2/H_2
$PED_{50}S_{50}$-P_{00}	193	1.43	1.02	26	7.4
$PED_{75}S_{25}$-P_{00}	241	1.48	1.24	27	8.9
$PED_{80}S_{20}$-P_{00}	378	1.5	1.9	40	9.5

7.3.4 Effects of water/silicon (H_2O/Si) and organic-inorganic ratio on the morphology of organic-inorganic materials

STEM images in **Figure 7.4** indicate that the inorganic phase exists as nanostructures in the organic-inorganic materials. EDX analysis has shown that these inorganic nanostructures are primarily made up of silicon and oxygen. With reference to Figure 6.5, the silicon atoms in these nanohybrid materials are fully condensed with three siloxane (Si-O-Si) bonds or partially condensed with two siloxane bonds and an ethoxy or methoxy moiety. Hence, these nanoparticle-lookalike structures can be classified as silicate agglomerations.

The acid-catalyzed, two-step sol-gel process leads to the formation of silicate structures in a polyether matrix.

a) $PED_{50}S_{50}$ b) $PED_{50}S_{50}$ –P_{20}

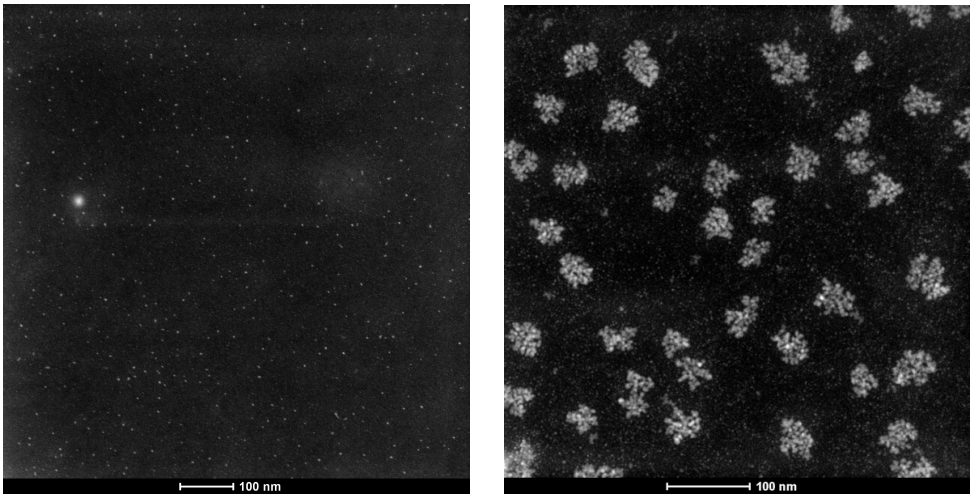

c) $PED_{75}S_{25}$ d) $PED_{75}S_{25}$ –P_{20}

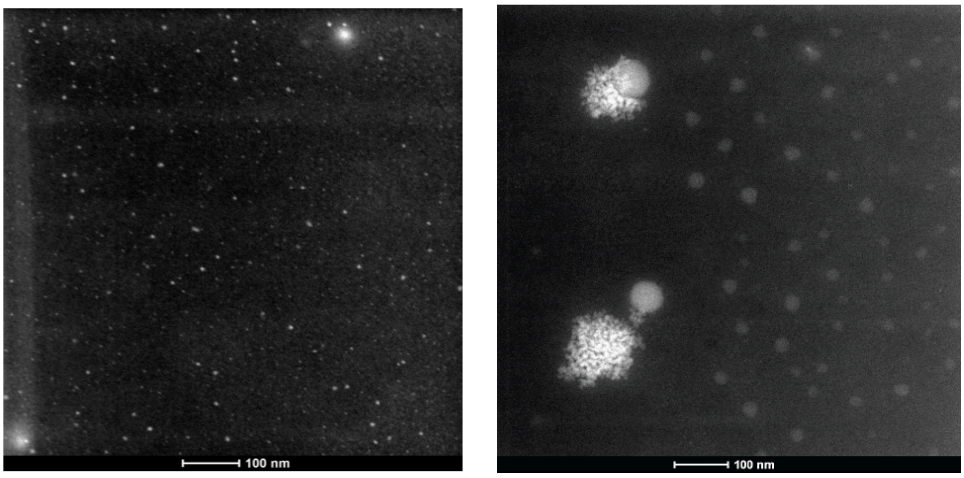

Figure 7.4 HAADF-STEM images of PEDS nanohybrid membranes

In the initial hydrolysis step of this approach, complete hydrolysis ensued as the H_2O/Si ratio < 4 i.e. hydrolysis and condensation are rate limiting and depolymerization rates are low [96]. The relatively low depolymerization rate

results in rate limiting cluster-cluster aggregation that forms weakly branched, rough-edged silicate nanostructures [97]. In the second synthesis step, the hydrolysis solution is mixed with a solution of polyether diamine dissolved in ethanol/water (70 wt.% / 30 wt.%) i.e. H_2O/Si ratio >> 4. With a large H_2O/Si ratio, condensation and reconstruction proceeds concurrently at comparable rates. The silicate network growth process becomes similar to a nucleation and growth process i.e. a monomer-cluster aggregation and results in smooth looking silicate nanostructures when water is absent from the system [96]. Smooth-looking silicate nanostructures are observed in $PED_{50}S_{50}$ and $PED_{75}S_{25}$ nanohybrid membranes. Unreacted short alkyl chains e.g. PEGMA and BuMA can also decrease the H_2O/Si ratio and increase hydrolysis rates during depolymerization. As polyethers form hydrogen bonds with water easily, the reduction in the concentration of “free” water molecules that engage in siloxane network development lowers the H_2O/Si ratio. With lower a H_2O/Si ratio, the silicate nanostructures evolve from a smooth-looking nanostructure (in PEDS nanohybrid membranes) to rough clusters (in PEGMA-grafted PEDS nanohybrid membranes) [96]. The siloxane network growth at a low H_2O/Si ratio is governed by the cluster-cluster aggregation mechanism. Additionally, the presence of unreacted PEGMA also increases the organic/inorganic ratio.

Silicate nanostructure sizes increase as a function of increasing polyether content i.e. when organic-inorganic ratio increases by the incorporation of more

polyether diamines or by grafting short alkyl chains. In $PED_{50}S_{50}$ organic-inorganic membranes, the average silicate size is 5 nm while in $PED_{75}S_{25}$ organic-inorganic membranes; the average silicate size is 7 nm. When PEGMA is grafted onto the PEDS main chains, silicate agglomerations become larger and more obvious. With 20 wt.% PEGMA grafts, silicate agglomerations increase from ~ 5 nm to 140 nm in $PED_{50}S_{50}$–P_{20} membranes, while silicate agglomerations increase from ~ 7 nm to 190 nm in $PED_{75}S_{25}$–P_{20} membranes. In this chapter, the increase in organic/inorganic ratio is facilitated with the engagement of more polyethers during synthesis and reducing epoxysilane content. This dilution effect affects silicate network dispersion in the polymer matrix. In the $PED_{75}S_{25}$ series, all the diamines and epoxy undergo the epoxy-diamine reaction in the presence of excess diamines. Consequently, the excess diamines result in a reduced water/silicon ratio and promote reaction-limited cluster-cluster agglomeration. Thus, forming bigger silicate agglomerations.

7.3.5 Effects of Ostwald ripening and organic phase T_g

Ostwald ripening is the effect of nanostructure agglomeration in which small nanostructures form a few large clusters with lower surface energy that is thermodynamically favored and is prevalent when depolymerization takes place [93]. As depolymerization is widespread in the process of water removal, Ostwald ripening in these organic-inorganic materials can be common, hence

leading to the larger silicate networks observed in Figures 7.4 (c) and (d). Another factor that may contribute to silicate agglomeration is the vitrification of the sol-gel reaction. Sol-gel vitrification is dependent on the glass-transition temperature (T_g) of the organic phase that governs the morphology growth mechanism in organic-inorganic materials. Lower T_gs attribute to a larger condensation extent that consequently leads to bigger silicate nanostructures [141], as seen in Figure 7.4. From **Figure 7.5**, it is evident that higher PEGMA graft contents reduce the T_g of these nanohybrid membranes. The combination of lower H_2O/Si ratios, higher organic-inorganic ratios, and Ostwald ripening leads to the agglomeration of siloxane networks that may also affect the relative fractional free volume content in the membrane material.

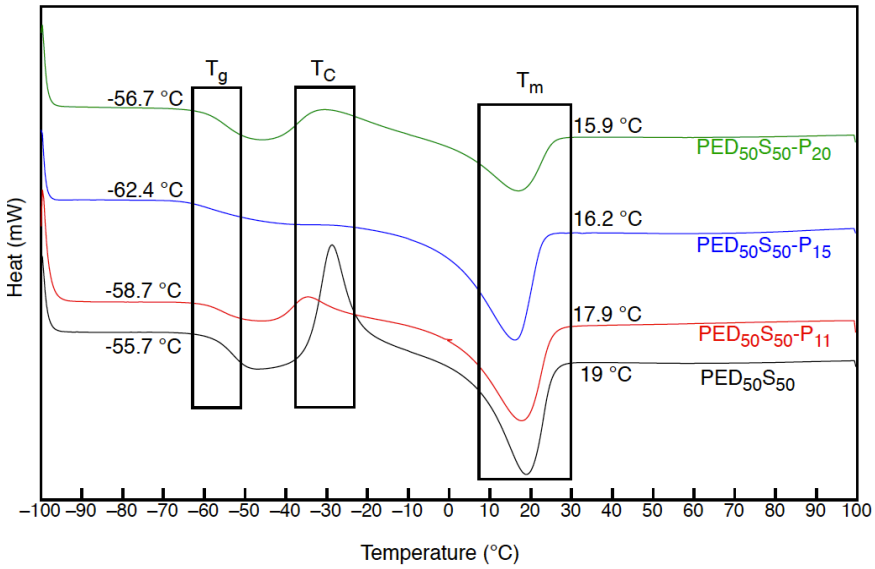

Figure 7.5 DSC spectra of $PED_{50}S_{50}$, $PED_{50}S_{50}$-P_{11}, $PED_{50}S_{50}$-P_{15} and $PED_{50}S_{50}$-P_{20} nanohybrid membranes.

7.3.6 Relative Fractional Free Volume Content in Nanohybrid Membranes

Figure 7.6(a) shows that the relative FFV content determined using bulk PALS in $PED_{50}S_{50}$ materials is lower when compared to $PED_{75}S_{25}$ materials. In $PED_{50}S_{50}$ membranes, excess alkoxysilanes may result in some mobile silicate nanostructures that are not immobilized by the polyether chains. Hence, when silicate agglomeration takes place in $PED_{50}S_{50}$ materials, main chain contortion may be less severe when compared to the main chain contortion in $PED_{75}S_{25}$ materials. In $PED_{75}S_{25}$ membranes, all alkoxysilanes are involved in the epoxy-diamine reaction with polyether diamines and the silanes are immobilized in fixed positions by the polyethers. When the silanes are condensed into silicate nanostructures, main chain contortions in $PED_{75}S_{25}$ membranes become more pronounced when compared to those in $PED_{50}S_{50}$ membranes. Ascribing to more pronounced main chain contortions and possible steric and kinetic constraints that inhibit silicate interpenetration and condensation; the spaces in between silicate nanostructures in $PED_{75}S_{25}$ materials are not as filled up as those in $PED_{50}S_{50}$ materials i.e. higher relative FFV in $PED_{75}S_{25}$ materials. According to Equation 2.10, a lower relative FFV content leads to lower diffusivity coefficients. Consequently, gas diffusivities and permeabilities of $PED_{50}S_{50}$ membranes are predicted to be lower when compared to $PED_{75}S_{25}$ membranes that possess a higher relative FFV content.

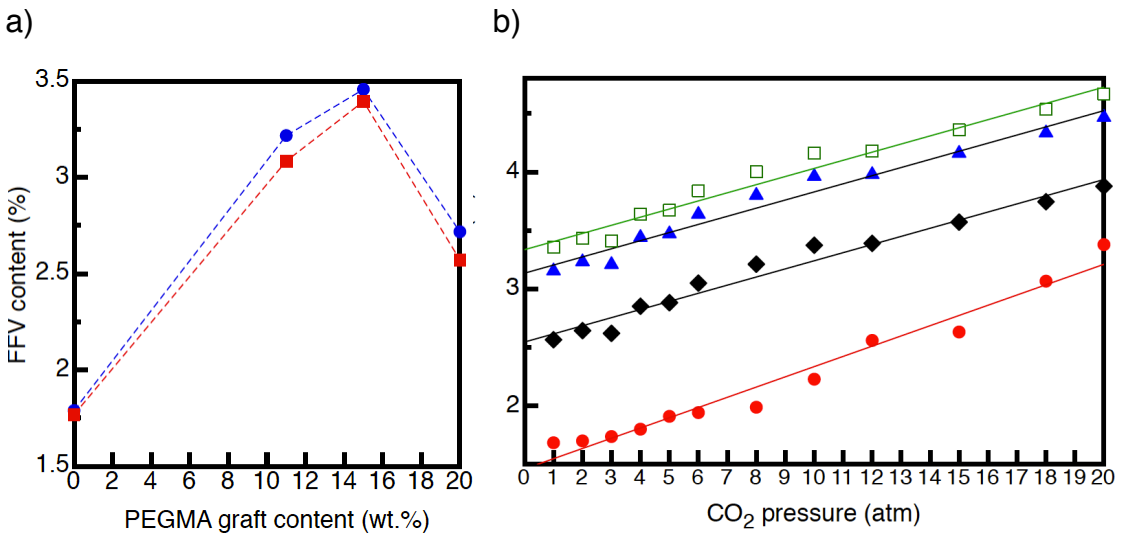

Figure 7.6 (a) Relative FFV content of $PED_{75}S_{25}$ (solid circle) and $PED_{50}S_{50}$ (empty square) nanohybrid membranes as a function of PEGMA graft content (wt. %). b) Relative FFV content of $PED_{75}S_{25}$ (circle), $PED_{75}S_{25}$-P_{11} (triangle), $PED_{75}S_{25}$-P_{15} (square) and $PED_{75}S_{25}$-P_{20} (diamond) as a function of CO_2 pressure.

The linear relationships between relative FFV in both $PED_{75}S_{25}$ and $PED_{75}S_{25}$ – P_{20} nanohybrid materials and CO_2 pressure in Figure 7.9(b) indicate that Henry's law dominates CO_2 sorption below 20 atm in these nanohybrid membranes i.e. CO_2 sorption is achieved via the swelling of existing free volume or the creation of new CO_2 sorption sites [145]. Additionally, the relative FFV content increases as PEGMA graft content increases from 0 wt.% to 15 wt.%. The relative FFV content in $PED_{75}S_{25}$-P_{15} membranes is higher than that in $PED_{75}S_{25}$-P_{20} membranes. With higher PEGMA graft content in $PED_{75}S_{25}$-P_{20} membranes, the PEGMA side chains are possibly longer. Longer PEGMA side chains can form hydrogen bonds with neighboring PEDS main chains or

PEGMA side chains. This inhibits chain mobility and thus reduces relative FFV content. Another reason that may lead to the observed trends in relative FFV content is the reduced main chain packing efficiency in grafted materials with large number of side chain grafts or longer side chains [146]. Coupled with the morphology of the inorganic phase, the relative FFV content plays an important role in determining the gas permeation and separation properties of the organic-inorganic materials.

7.3.7 Gas permeability measurements of the organic-inorganic materials

The ideal CO_2 (200 Barrer) and H_2 (28 Barrer) permeabilities of $PED_{50}S_{50}$ membranes are similar to membranes with the same chemical composition in Shao and Chung's work [29]. Compared to the P_{CO_2} and P_{H_2} of $PED_{50}S_{50}$ in **Figure 7.7**, P_{CO_2} and P_{H_2} of $PED_{50}S_{50}$ -P_{20} increase by 5.3 and 4.4 fold. In the $PED_{75}S_{25}$–P_{20} nanohybrid membrane series, P_{CO_2} and P_{H_2} increase by 7.5 and 5.7 fold, respectively. The mixed gas permeabilities of $PED_{75}S_{25}$-P_{xx} membranes are similar to ideal gas permeabilities. The CO_2/H_2 permselectivity data is shown in **Table 7.2**. The larger increment in P_{CO_2} permeability of the PED_{75}-S_{25}-P_{20} can be ascribed to higher polyether content and higher relative FFV content, while the higher relative FFV content also enhances P_{H_2} permeability. Nanohybrid membranes with alkyl methacrylate grafts comprising 5-10 EO units (PEGMA) display higher P_{CO_2} and P_{H_2} compared with

membranes with alkyl methacrylates consisting of one EO unit (BuMA). Congruent with other works [29, 94, 159], the observed larger P_{CO_2} jumps in $PED_{75}S_{25}$–P_{xx} nanohybrid membranes correlates to higher ethylene oxide content and more importantly, morphological changes in silicate nanostructures.

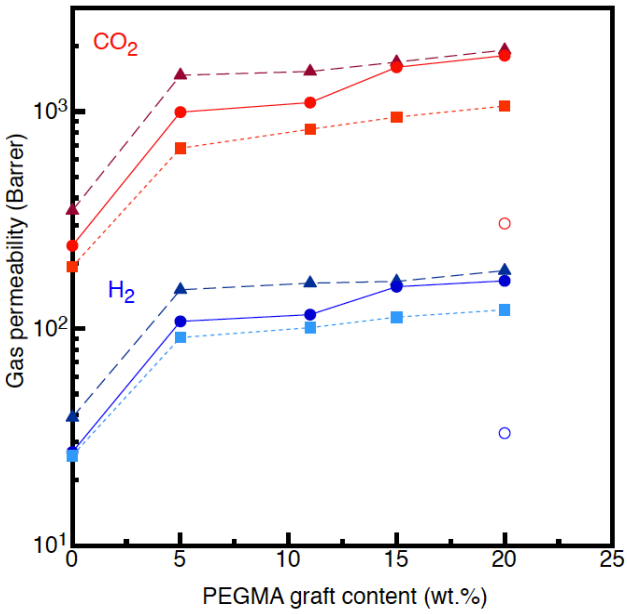

Figure 7.7 Pure gas permeabilities of $PED_{50}S_{50}$(squares), $PED_{75}S_{25}$(circles), $PED_{80}S_{20}$(triangles) [159] nanohybrid membranes with different PEGMA graft content and $PED_{75}S_{25}$- $BuMA_{20}$(empty circles). The solid and empty symbols represent CO_2 and H_2 permeability, respectively. The lines are drawn to provide a guide to the eye. Uncertainty in gas permeabilities is around ± 10 %.

Table 7.2 Gas permeability and selectivity of $PED_{50}S_{50}$-P_{xx} and $PED_{75}S_{25}$-P_{xx} membranes studied in this work

Sample Code	P_{CO_2} (Barrer)	P_{H_2} (Barrer)	CO_2/H_2
$PED_{50}S_{50}$-P_{00}	193	26	7.4
$PED_{50}S_{50}$-P_{05}	678	91	7.5
$PED_{50}S_{50}$-P_{11}	829	101	8.2

$PED_{50}S_{50}$-P_{15}	943	113	8.4
$PED_{50}S_{50}$-P_{20}	1060	122	8.7
$PED_{75}S_{25}$-P_{00}	241	27	8.9
$PED_{75}S_{25}$-P_{05}	994	108	9.2
$PED_{75}S_{25}$-P_{11}	1100	116	9.5
$PED_{75}S_{25}$-P_{15}	1600	156	10.3
$PED_{75}S_{25}$-P_{20}	1810	166	10.9
$PED_{75}S_{25}$-$BuMA_{20}$	305	33	9.5

Compared with base PEDS membranes i.e. without PEGMA grafts, the S_{CO_2} coefficients of PEGMA-grafted nanohybrid membranes are enhanced by approximately 1.4 fold. As ethylene oxide moieties preferentially interacts with CO_2 penetrants, the higher EO content in $PED_{75}S_{25}$–P_{xx} nanohybrid membranes results in larger S_{CO_2} coefficients when compared to $PED_{50}S_{50}$–P_{xx} nanohybrid membranes. Additionally, the morphology of the silicate networks also contributes to enhanced S_{CO_2} and P_{CO_2} coefficients. Ostwald ripening and changes in organic-inorganic ratio cause the agglomeration of silicate networks (5 – 10 nm) into well-dispersed bigger siloxane networks (140 – 190 nm). As Si-O bonds possess good CO_2 affinity [162], the silicate nanostructures can significantly contribute to CO_2 sorption. In **Figure 7.8**, the CO_2 sorption isotherms of $PED_{75}S_{25}$–P_{xx} and $PED_{50}S_{50}$–P_{xx} membranes resemble the CO_2

sorption of polydimethylsiloxane (PDMS) and the S_{CO_2}coefficients increase as a function of PEGMA-graft content (from 0 wt.% to 20 wt.%). These signify that the inorganic phase is fundamental for enhanced CO_2 permeabilities in these nanohybrid membranes. Interestingly, CO_2 permeability and solubility increases as a function of silicate nanostructure size. The 1.4-fold increase in S_{CO_2} coefficients of $PED_{75}S_{25}$–P_{xx} membranes is insufficient to register a 7.5-fold increase in P_{CO_2} coefficients. It is evident that increments in D_{CO_2} coefficients lead to the significant jumps observed in P_{CO_2}.

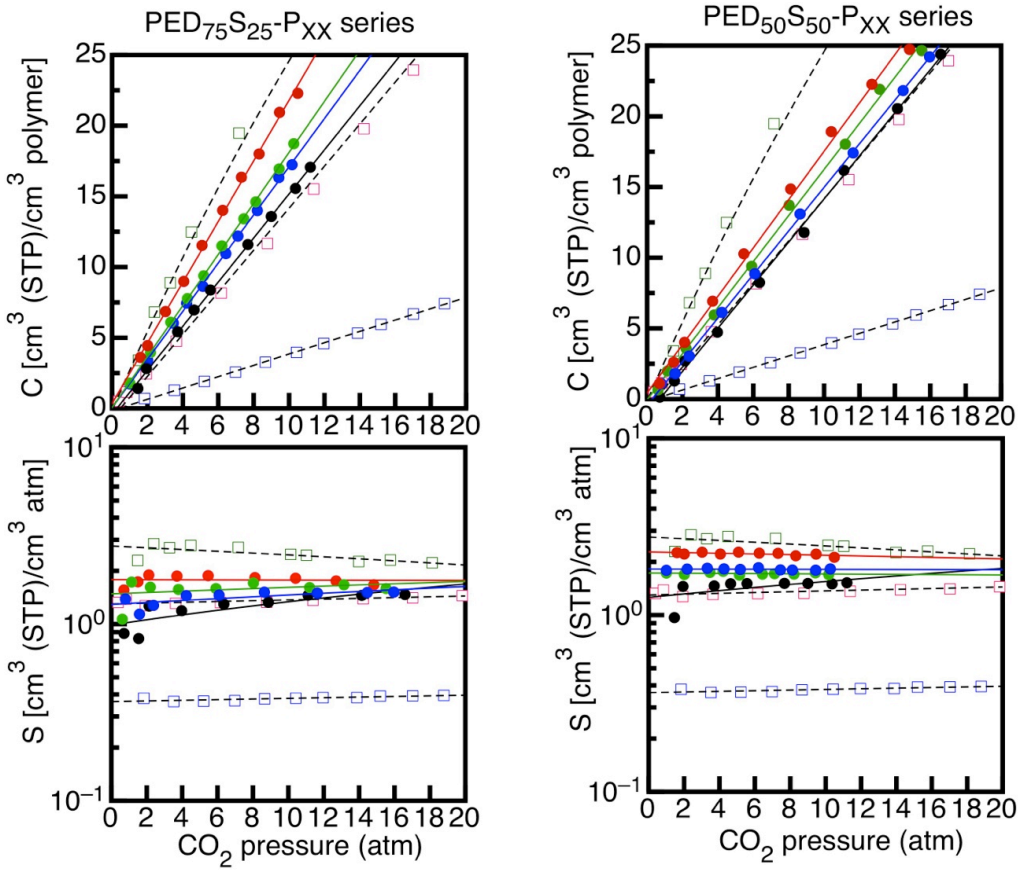

Figure 7.8 Sorption isotherms and solubility coefficients of PEDS nanohybrid membranes. The colored squares denote the sorption isotherms and solubility coefficients of semi-crystalline PEO (blue), PDMS (pink), PTMSP (green). The

empty colored circles represent nanohybrid membranes containing 0 wt.% (black), 11 wt.% (green), 15 wt.% (blue), and 20 wt.%(red) PEGMA grafts.

D_{CO_2} coefficients are determined using Equation 2.4 i.e. D = P / S and are shown in **Figure 7.9**. Similar to S_{CO_2} coefficients, D_{CO_2} coefficients increase as a function of PEGMA content (from 0 wt.% to 20 wt.%). *In situ* fabrication of organic-inorganic materials usually yields a morphology that is similar to a polymeric phase filling up the open pores of a silica aerogel [96]. In these nanohybrid membranes, the opposite polarity between the organic and inorganic phases prohibits complete filling up of the open pores [79]. Moreover, the agglomeration of the silicate nanostructures prohibits interpenetration and condensation that can fill up the space between the silicate nanostructures. These lead to open-porosity that consequently enhances relative FFV content across all PEGMA-grafted nanohybrid membranes. In nanohybrid membranes with 20 wt.% PEGMA grafts, D_{CO_2} coefficients are lower than the D_{CO_2} coefficients of nanohybrid membranes with 10 and 15 wt.% PEGMA grafts. Higher PEGMA content i.e. 20 wt.% of PEGMA grafts leads to larger or longer PEGMA side chains that are more susceptible to form hydrogen bonds (via –OH moieties) with neighbouring PEDS main chains or other PEGMA side chains; resulting in reduced chain mobility that decreases FFV content. As diffusivity coefficients are inversely related to FFV content, enhanced relative FFV content increases diffusivity coefficients i.e. gas transport channels for gas diffusion. D_{CO_2} coefficients increase by 5.2 times and by 3.5 times in $PED_{75}S_{25}$–

P_{xx} and $PED_{50}S_{50}$–P_{xx} membranes, respectively. As the working materials have good CO_2 affinity, H_2 permeability increments can be ascribed to the increase in relative FFV content and diffusivity coefficients.

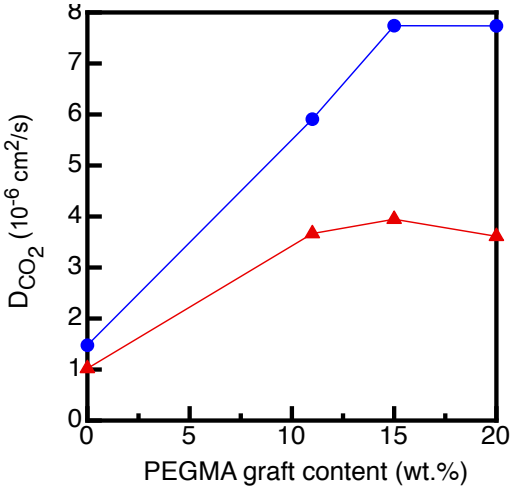

Figure 7.9 Diffusivity coefficients of PEDS nanohybrid membranes. Solid circles and triangles represent $PED_{75}S_{25}$ and $PED_{50}S_{50}$ nanohybrid membranes, respectively.

7.4 Summary

The incorporation of ethylene oxide-based side chains reduces the overall concentration of moieties with good CO_2 affinity in relation to those without CO_2 affinity. This highlights the influence of inorganic phase morphologies on gas permeability, in particular CO_2 permeability. The underlying reason behind the observed significant jumps in CO_2 permeability is the increase in both solubility and diffusivity coefficients. Larger silicate nanostructures lead to higher CO_2 solubility while significantly enhancing free volume content in the nanohybrid membranes. The CO_2 permeability values of nanohybrid membranes studied in this work are in the same magnitude as the CO_2 permeability values of PDMS,

the most permeable rubbery polymer, while H_2 permeability of these nanohybrid membranes is much lower than that of PDMS. This marks an improvement in CO_2/H_2 selectivity. The remarkable CO_2 transportation capabilities of these nanohybrid membranes facilitate possible large-scale nanohybrid membrane applications.

CHAPTER EIGHT:

MOLECULAR DESIGN OF NANOHYBRID MEMBRANES FOR OPTIMAL CO_2 CAPTURE

8.1 Introduction

At near ambient operating conditions, organic-inorganic materials derived from polyethylene oxide (PEO), polypropylene oxide (PPO) and silicate nanostructures comprise high CO_2 affinity components and possess high CO_2 permeability with good CO_2/H_2 separation capabilities [29, 93, 94, 159] that are comparable to pure polymeric rubbery membranes [24]. In these organic-inorganic membranes, the polyether matrix influences the Si-O-Si network connectivity, while building up an alternative polyether network via polymerization or polycondensation that enhances CO_2/light gas selectivity. Additionally, the polar ether oxygens in PEO interact favorably with acidic CO_2 penetrants via a dipole-quadrapole interaction [149], while the pendant methyl group in PPO enhances CO_2 permeability by increasing the relative fractional free volume [161].

These organic-inorganic materials are synthesized via an acid-catalyzed sol-gel process that involves the hydrolysis of $Si\text{-}OCH_3$ moieties to Si-OH bonds, followed by condensation of the Si-OH bonds to form irreversible Si-O-Si cross-links [96, 163]. The Si-O-Si networks increase the mechanical stability of these organic-inorganic materials [29] and impart higher CO_2 affinity to the organic-inorganic materials [159]. The grafting of short alkyl chains onto the main chains of these organic-inorganic materials yield nanohybrid materials with CO_2 permeability comparable to the CO_2 permeability of PDMS (same order of

magnitude), while obtaining a CO_2/H_2 selectivity value that is ~ 5 times larger than that of PDMS [159]. The distribution of the inorganic nanostructures is the key to ultrahigh CO_2 permeability and high CO_2/H_2 selectivity.

To determine the actual mechanisms behind the significant improvements in membrane properties, the morphology of the inorganic phase in this nanohybrid material must be more extensively characterized. This chapter addresses the relationship between the synthesis conditions and the inorganic phase morphology and consequently, the CO_2 permeability and CO_2/H_2 separation of these nanohybrid materials and will focus on the effects of synthesis parameters for e.g. hydrolysis durations, condensation durations, and modification durations on gas permeability and gas separation properties of nanohybrid membranes.

8.2 Materials and Experimental details

8.2.1 Materials

The materials used for the work detailed in this chapter were the same as those used in Chapter 6. Briefly, the base organic-inorganic material was synthesized using a propylene oxide end-capped polyethylene glycol that is commercially known as Jeffamine® ED-2003 (M_w = 2000 g/mole). Poly ethylene glycol methacrylate (PEGMA: M_w = 360 g/mole), ethanol (HPLC grade) and 3-glycidyloxypropyltrimethoxysilane (GOTMS: M_w = 236 g/mole) and hydrochloric acid (HCl) were used. All chemicals and solvents, except for PEGMA, were used as received. Inhibitors in PEGMA were removed according to the procedure detailed in Chapter 6.

8.2.2 Synthesis and modification of organic-inorganic membranes

First, the hydrolysis times were varied from 30 minutes to 1440 minutes. The ratio between the polyether diamine and epoxysilane was maintained at 80 wt.%: 20 wt.%. GOTMS was first hydrolyzed for a stipulated time (30 to 1440 minutes) at room temperature using a catalyzing aqueous solution containing 37.5 wt.% HCl. Subsequently, the hydrolyzed alkoxysilane solution was added to a solution consisting of PPO-PEO-PPO diamine dissolved in 70 wt.% ethanol and 30 wt.% deionized water. The epoxy-amine reaction and preliminary condensation occurred during magnetic stirring at 750 rpm at 70 °C for 1 hour.

These organic-inorganic materials are coded $PED_{80}S_{20}$-H^x, whereby H represents the hydrolysis process; the superscript denotes the hydrolysis duration ranging from 30 to 1440 minutes.

In the second part, the effects of condensation duration on gas permeation in organic-inorganic materials were studied using $PED_{80}S_{20}$-H^{30} nanohybrid materials. $PED_{80}S_{20}$ solutions were synthesized using the aforementioned protocol (in Chapter 6) for different condensation durations, ranging from 1 to 24 hours. These materials are coded $PED_{80}S_{20}$-Cxh, whereby "xh" denotes the condensation duration in hours.

In the third part, the effects of ozone pre-treatment times on gas permeation were studied for organic-inorganic materials with optimal CO_2/H_2 selectivity i.e. $PED_{80}S_{20}$-C1h materials with 30 minutes of hydrolysis. $PED_{80}S_{20}$-C1h solutions were first synthesized and allowed to cool to room temperature prior to 30, 60, 180 and 300 seconds of ozone pre-treatment. Ozone pre-treatment was carried out using an AC Faradayozone – high concentration ozone generator (L10G). High purity oxygen contained in a 10L bottle was obtained from SOXAL, Singapore and was converted into ozone (ozone flow was limited to 0.5 liters per minute). Upon ozone pre-treatment, 43 wt.% of PEGMA were added to the ozone pre-treated mixture and the resultant solution was stirred at 70 °C for 24 hours to facilitate PEGMA grafting onto the PEDS main chains.

The ozone modified $PED_{80}S_{20}$-C1h materials are coded $PED_{80}S_{20}$-oXs, whereby "o" represents the ozonolysis process and "Xs" stands for the pre-treatment duration in seconds.

8.2.3 Membrane fabrication

Protocol details for membrane fabrication can be found in Chapter 6. In brief, organic-inorganic membranes were fabricated using a slow casting method in a Teflon dish via an initial solvent evaporation process and a subsequent evaporation process. Residual solvent was removed via vacuum drying. Unreacted monomers were removed by immersing these membranes in deionized water for 5 days and dried. The deionized water was changed everyday. These nanohybrid membranes were stored in a dry box at 27 % humidity and 25 °C prior to testing and characterization.

8.2.4 Membrane characterization

ATR-FTIR was used to characterize the chemical structures of the working materials. The data were analysed using Spectrum Version 5.3 (analytical software). The presence of Si-O-Si networks in the working membrane materials were validated using solid-state ^{29}Si. Prior to solid-state NMR analysis, the organic-inorganic materials were ground via freeze milling. To determine the crystallinity, glass transition (T_g) and melting (T_m) temperatures of the organic-inorganic membranes, differential scanning calorimetry (DSC) was

performed using a DSC822^e (Mettler Toledo) calorimeter. HAADF-STEM was used to observe inorganic phase morphology and dispersion. EDX was used to verify the elemental composition of the inorganic nanostructures in the organic-inorganic membranes.

8.2.5 Gas permeation and sorption measurements

The pure gas permeabilities were determined using the constant volume-variable pressure method discussed in Section 3.9.1. For mixed gas permeability tests (as detailed in Section 3.9.2), a mixed gas mixture containing x-mol. % of H_2 in CO_2 was used as the feed gas mixtures and the measurements were conducted at 35 °C with a CO_2 partial pressure of 3.5 atm. The molar concentrations of H_2 tested in this work were 50 mol.%, 40 mol.%, and 10 mol.%. Carbon dioxide sorption tests were conducted using a Cahn D200 microbalance sorption cell at 35 °C over a pressure range of 0-250 psig (0-17.24 bar). Subsequently, CO_2 diffusivity coefficients were calculated using Equation 3.2.

8.3 Results and Discussions

8.3.1 Chemical structure of working materials

Figure 8.1 shows the chemical structure of a base material fabricated via an epoxy-diamine reaction in aqueous solutions and the modification of this base material using ozone pre-treatments. The chemical structure of this organic-inorganic material has been confirmed using ATR-FTIR.

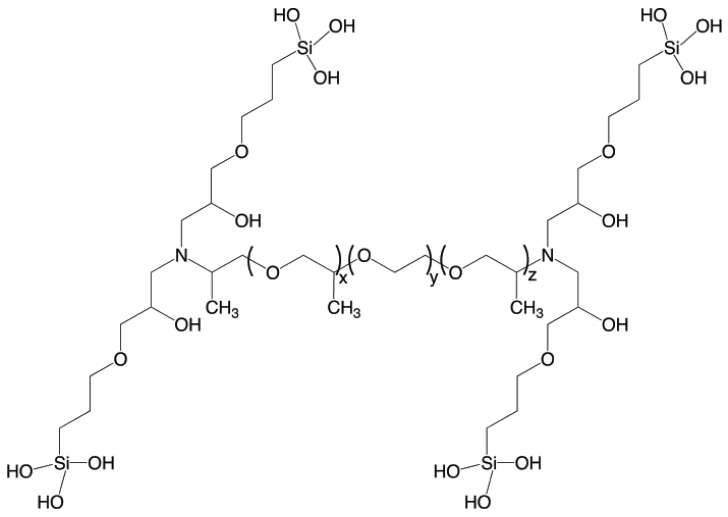

Figure 8.1 Chemical structure of PEDS base material

Ether segments from the 165-atom PPO-PEO-PPO backbone, and Si-O-Si networks dominate the spectra shown in **Figure 8.2**. In the FTIR spectrum of a $PED_{80}S_{20}$-C3h material, the signature bands are the ether C-O-C stretching band at 1105 cm^{-1} and the CH_2 scissoring and stretching bands at 1465 and 2868 cm^{-1}, respectively [164]. Other peaks in the fingerprint region at 1248, 1283, 1345 cm^{-1} correspond to the CH_2-CH_2 anti-symmetric twisting, CH_2-CH_2

quasi-symmetric twisting, and CH_2-CH_2 asymmetric wagging, respectively [133]. At 848 cm^{-1}, the peak corresponds to a coupled quasi-antisymmetric CH_2 rocking and quasi-symmetric C-O stretching mode, while the peak at 945 cm^{-1} correlates to a C-C stretching. Additionally, the non-stoichiometric ratio of polyether diamine and alkoxysilane used in this work leads to the strong peak at 1656 cm^{-1} resulting from the N-H scissoring vibration of unreacted diamines [117]. Compared to the ATR-FTIR spectrum of the neat polyether diamine, the peak at 1100 cm^{-1} in the FTIR spectrum of $PED_{80}S_{20}$-C3h is more asymmetrical. This indicates that overlapping bands are present in the FTIR spectrum of $PED_{80}S_{20}$-3h. The asymmetrical band at 1100 cm^{-1} can be attributed to a combination of the antisymmetric stretching mode Si-O-Si [165] and the characteristic ether C-O-C stretching band. The presence of a Si-O-Si network is evidenced by the presence of the shoulder peak at 1258 cm^{-1} that signifies the asymmetric stretching vibrations of the Si-O-Si bridging sequence [165]. The peak at 1038 cm^{-1} corresponds to the propyl chain attached to the silicon [165]. Weak shoulder peaks at 1088 cm^{-1} and the peak at 886 cm^{-1} relates to stretching vibrations of $SiOCH_3$ and the stretching mode of SiOH [165], indicating that hydrolysis is nearly complete. The solid-state ^{29}Si NMR analysis that will be discussed later confirms this observation. The absence of a strong, obvious peak at 910 cm^{-1} indicates that all epoxy rings are opened up and partake in the cross-linking process between polyether diamines and alkoxysilanes [165].

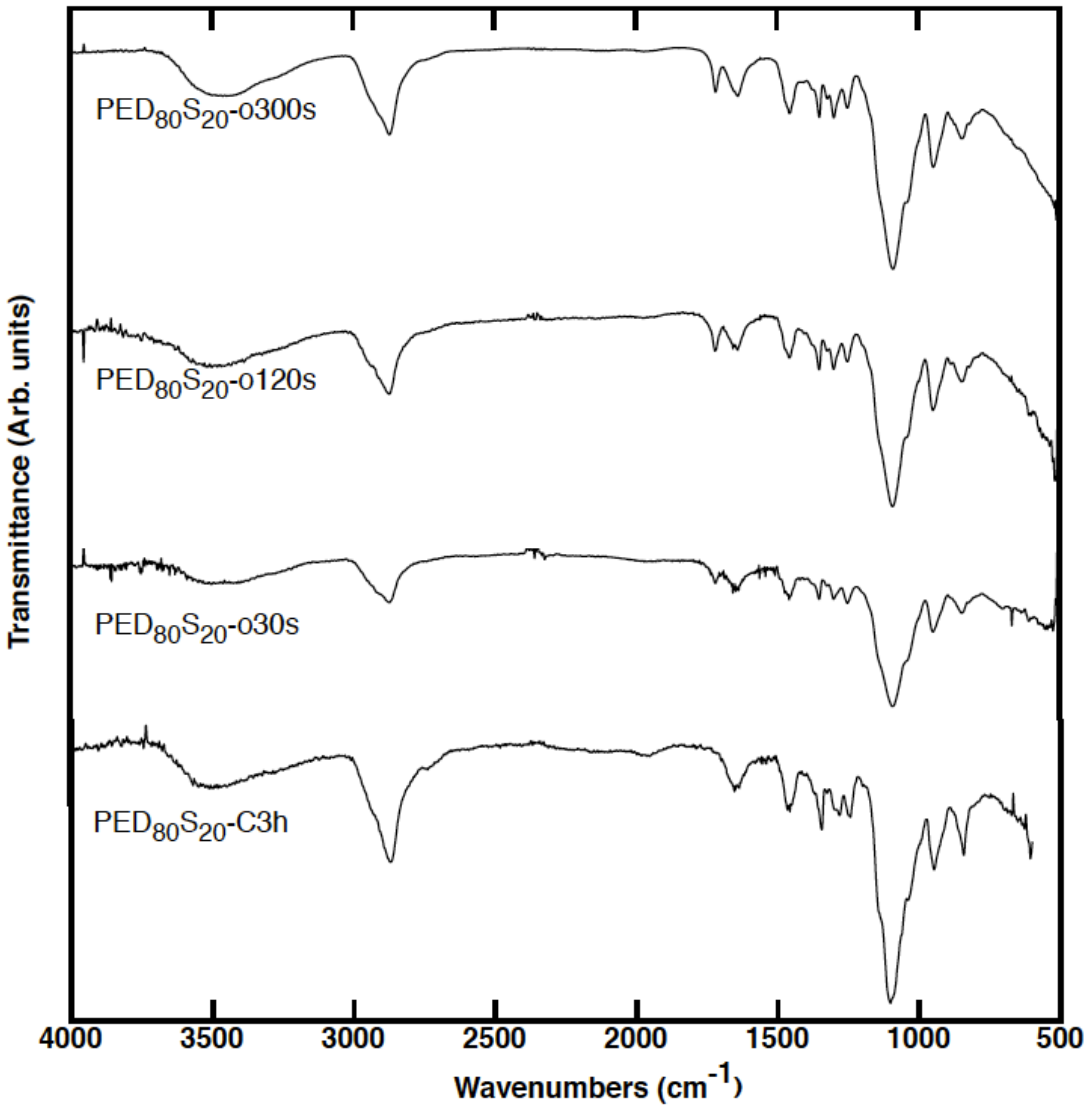

Figure 8.2 ATR-FTIR spectra of $PED_{80}S_{20}$ materials that were synthesized using 3 hours of condensation ($PED_{80}S_{20}$-3h), and $PED_{80}S_{20}$ materials that were synthesized using 1 hour of condensation and different ozone pre-treatment durations ranging from 30 to 300 seconds ($PED_{80}S_{20}$-oXs with "o" indicating that these $PED_{80}S_{20}$ materials were modified with ozone pre-treatment while "X" denotes the ozone pre-treatment duration).

In the FTIR spectra of $PED_{80}S_{20}$–C1h nanohybrid membranes that were modified with different ozone pre-treatment times, the peak at 1708 cm^{-1} correlates to the O-C=O ester stretch of PEGMA [166]. The intensity of this

peak increases when ozone pre-treatment time increase from 30 seconds to 300 seconds, indicating that more PEGMA is grafted onto the PEDS main chains. The intensity and shape of the N-H peaks at ~ 1646 and 1633 cm^{-1} remain intact. The absence of peaks ranging from 1658 – 1648 cm^{-1} indicate the absence of C=C bonds in these ozone-modified $PED_{80}S_{20}$–C1h nanohybrid membranes i.e. PEGMA is successfully grafted onto the PEDS main chains. Additionally, the occurrence of two new peaks at 2917 and 2851 cm^{-1} correspond to the asymmetrical and symmetrical stretching modes of a methyl (CH_3) group [117]. These peaks are more obvious in PEGMA-grafted PEDS materials that contain higher contents of CH_3.

In **Figure 8.3**, the presence of only T^2 (-59 ppm) and T^3 (-67 ppm) peaks in the ^{29}Si solid-state NMR of $PED_{80}S_{20}$ synthesized from different condensation and ozone pre-treatment durations indicate Si atoms that are fully condensed with siloxane bonds as well as some partially condensed Si atoms with one ethoxy or methoxy bonds and two siloxane bonds. This validates the ATR-FTIR analysis on the hydrolysis state of the alkoxysilanes. Additionally, EDX analyses in **Figure 8.4** show that the elemental composition of these bright inorganic nanostructures consists of silicon and oxygen. The evidence yielded by EDX, ATR-FTIR and ^{29}Si NMR concur that the inorganic nanostructures are primarily made up of silicates.

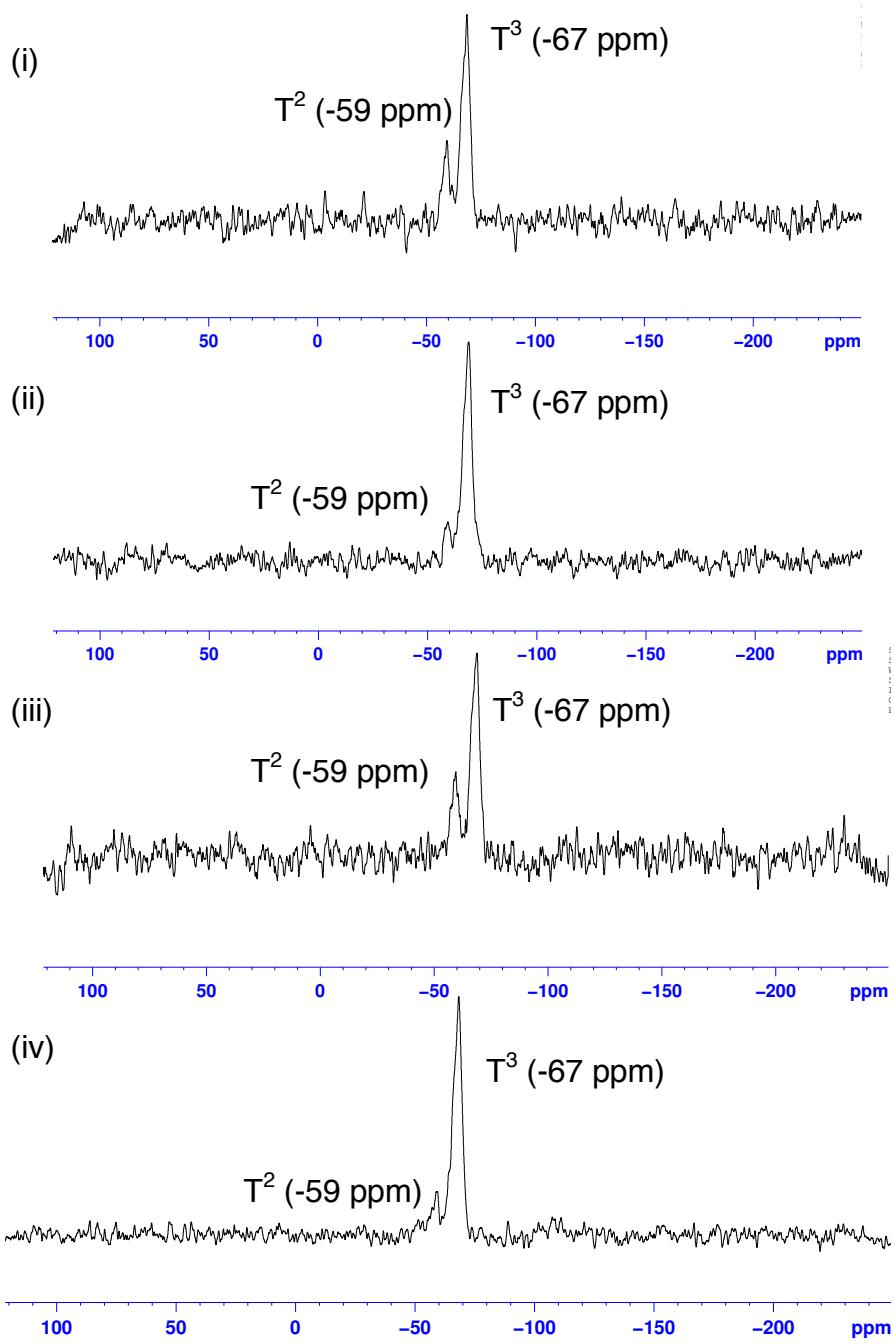

Figure 8.3 Solid-state ^{29}Si NMR of (i) $PED_{80}S_{20}$-C3h, (ii) $PED_{80}S_{20}$-C24h, (iii) $PED_{80}S_{20}$-o30s, and (iv) $PED_{80}S_{20}$-o300s organic-inorganic membranes. T^2 peaks represent partially condensed Si atoms that consist of 2 siloxane bonds and a methoxy or an ethoxy bond; while T^3 peaks represent fully condensed Si atoms with 3 siloxane bonds.

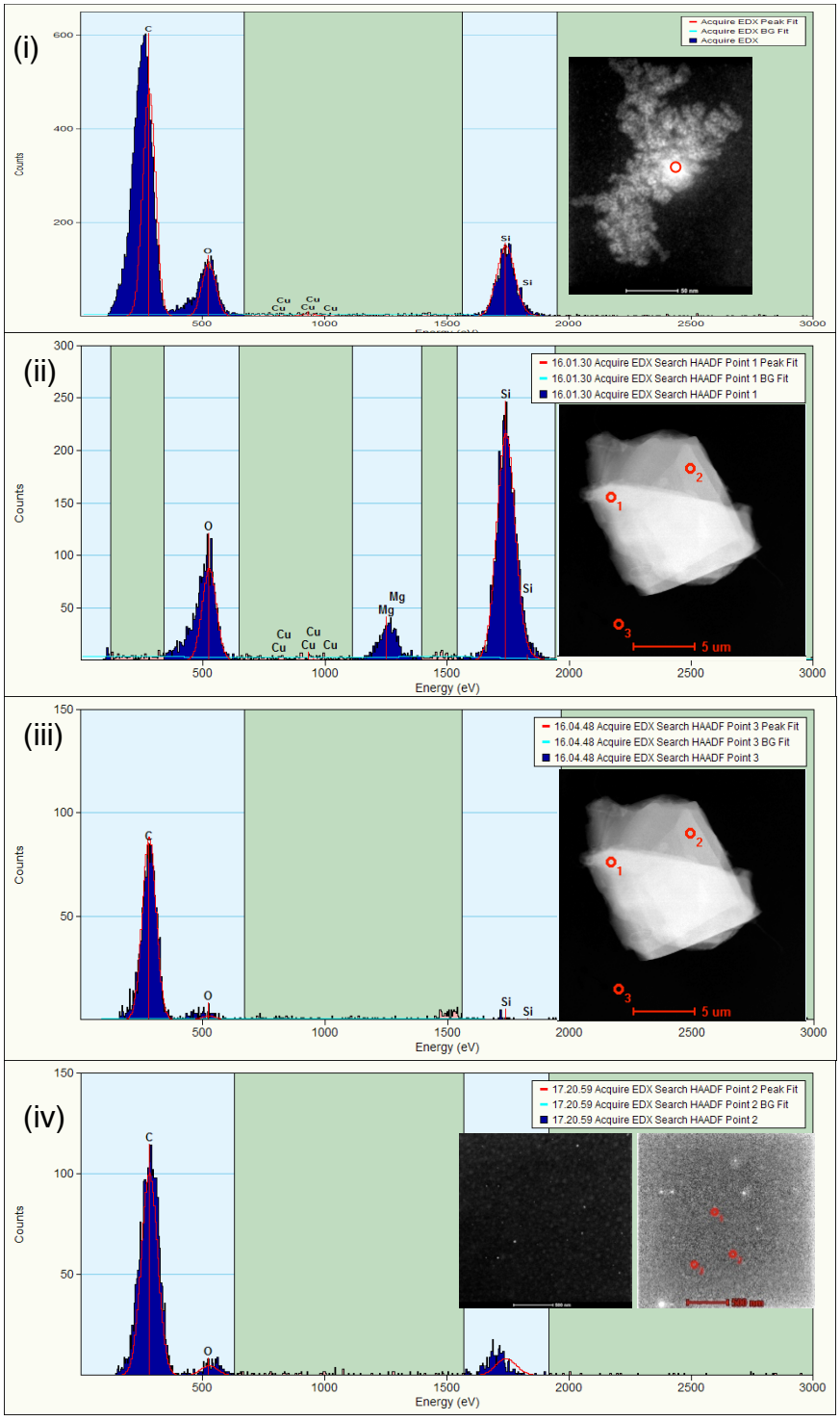

C = 80.65 wt.%
O = 10.24 wt.%
Si = 8.9 wt.%

O = 30.89 wt.%
Si = 55.33 wt.%
Cu = 13.77

C = 98.86 wt.%
O = 1.11 wt.%
Si = 0.01 wt.%

C = 95.09 wt.%
O = 2.37 wt.%
Si = 2.53 wt.%

Figure 8.4 EDX analyses of (i) $PED_{80}S_{20}$-1h, (ii) inorganic phase of the $PED_{80}S_{20}$-24h material, (iii) organic phase of the PEDS-24h material, (iv) $PED_{80}S_{20}$-o300s

8.3.2 Effects of hydrolysis duration on gas permeation properties of organic-inorganic membranes

As hydrolysis duration increases from 30 minutes to 1440 minutes, the acidic aqueous solution (sol) comprising of GOTMS gradually evolves into a gel that is undissolvable in solvents. The gelation process is indicative of an extensive network formed by interconnected discrete colloids in the solvent [167]. **Figure 8.5** shows a pictorial depiction of the colloidal gel formation. This extensive network contributes to the non-dissolvability of the gel in common synthesis solvents like ethanol, acidic aqueous medium, THF, dimethylformamide (DMF), NMP and DMAc. The gelation process can also be viewed as the formation of particles that are big enough to overcome mutual repulsion i.e. Ostwald ripening effects [96]. Gas adsorption is stronger in smaller particles that possess larger surface areas [168, 169]. Hence, it can be hypothesized that with longer hydrolysis durations, larger silicate nanoparticles are formed; and CO_2 adsorption in larger silicate nanoparticles is weaker. The lower CO_2 adsorption i.e. lower CO_2 solubility of larger silicate nanoparticles consequently leads to lower CO_2 permeability.

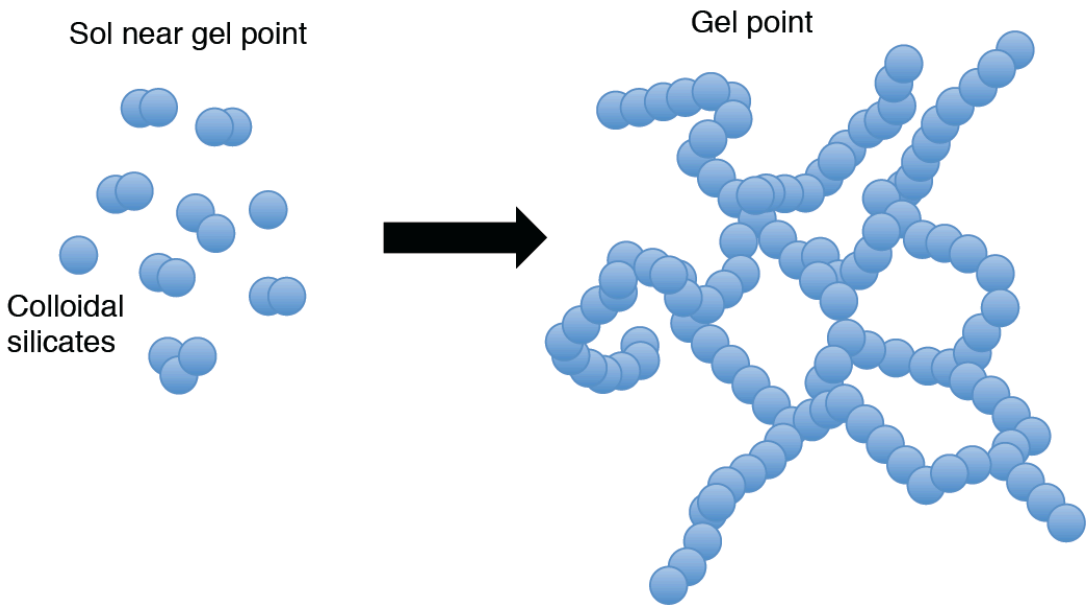

Figure 8.5 The gelation process involves the agglomeration of colloidal silicates during hydrolysis.

Figure 8.6 shows the CO_2 permeability $PED_{80}S_{20}$-C1h organic-inorganic membranes synthesized from different hydrolysis durations. The CO_2 permeability of these organic-inorganic membranes decreases as hydrolysis duration increases from 30 minutes to 720 minutes. Although these observations support the aforementioned hypothesis, more characterization work is required to validate this hypothesis.

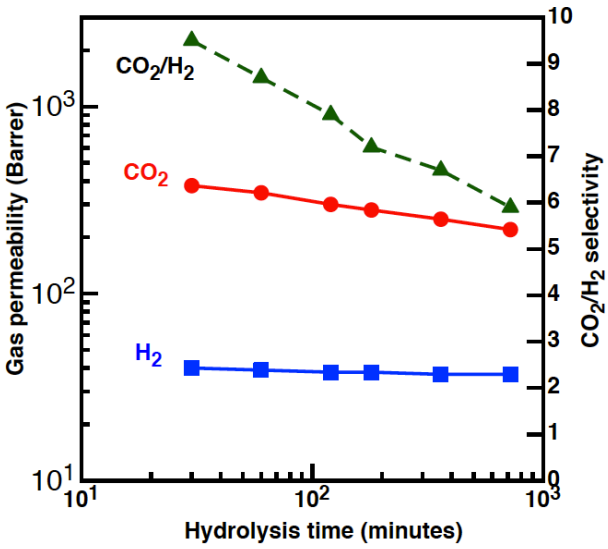

Figure 8.6 Pure gas permeabilities of $PED_{80}S_{20}$ membranes synthesized with different hydrolysis durations from 30 to 720 minutes and 1 hour of condensation. Circles represent CO_2 permeability, H_2 permeability is represented by squares, and while CO_2/H_2 selectivity is represented by triangles.

8.3.3 Effects of condensation duration on gas permeation properties of organic-inorganic membranes

Figure 8.7 compares the effects of the condensation duration from 1 hour to 24 hours on the morphology of the inorganic networks of $PED_{80}S_{20}$ materials. During the first 1 to 6 hours of condensation, loose clusters of silicate nanostructures grow from 15 nm to 500 nm. The solid looking 15 nm silicate nanostructures randomly agglomerate to form 500 nm loosely clustered, irregular-shaped silicate nanostructures. As condensation duration increases to 12 and 24 hours, the 500 nm loosely clustered, irregular shaped silicate nanostructures evidently transform into small, compact (~ 60 nm) polyhedral silicate nanostructures surrounded by small silicate nanostructures (5 - 15 nm).

At lower magnifications, silicate structures with sizes up to 1 – 2 μm can be observed in $PED_{80}S_{20}$-C24h samples (refer to STEM image in Figure 8.5).

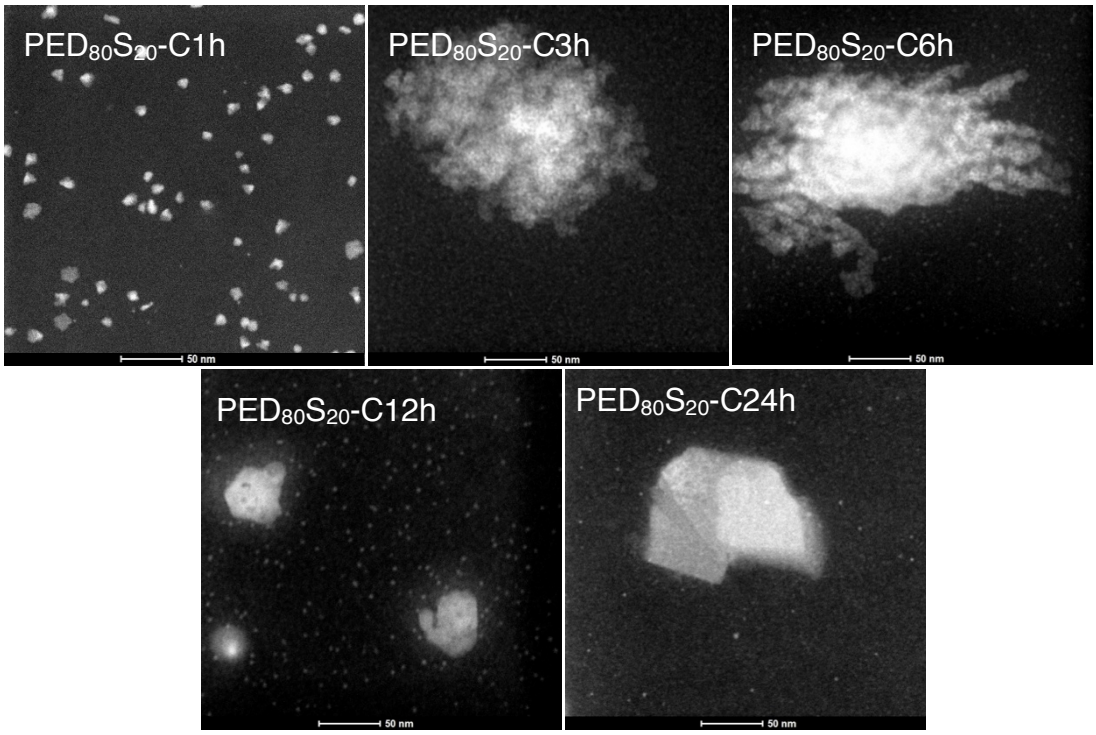

Figure 8.7 STEM images of $PED_{80}S_{20}$ materials synthesized using condensation durations ranging from 1 to 24 hours with no ozone modification. The sizes of the silicate nanostructures grow from 15 nm (1h) to a network of 220 nm (3h) to 500 nm (6h). Subsequently, after 12 hours of condensation, silicon-based structure sizes decrease to 60 nm. Meanwhile, there are 5 nm silicate nanostructures surrounding the 60 nm nanostructure. After 24 hours of condensation, the silicate nanostructure size doubles to 150 nm.

Figure 8.8 shows that CO_2 and H_2 permeability increase as the condensation duration is increased from 1 to 3 hours; however, after this maximum, there is a steady decline out to 24 hours of condensation. The highest CO_2 and H_2 permeability values are achieved at 3 hours of condensation, while the highest CO_2/H_2 selectivity is obtained at 1 hour of condensation; selectivity steadily declines with condensation time out to 24 hours. As FTIR and NMR analyses

have indicated that there are no chemical structure changes in these nanohybrid materials over different condensation durations, the only variable among these organic-inorganic materials is the morphology and distribution of the silicate nanostructures. The inorganic phase morphology in $PED_{80}S_{20}$-C3h consists of loosely clustered silicate (size ~ 300 nm) surrounded by smaller silicates (size ~ 5 nm). High concentrations of these small silicates appear to be essential for high CO_2 permeability. The materials formed using longer periods of condensation have fewer of these small nanostructures and lower CO_2 permeability. It appears that the larger silicate nanostructures also affect CO_2 permeability. Loose clusters of silicate nanostructures in $PED_{80}S_{20}$-C3h materials yield the highest CO_2 permeability while polyhedral silicate nanostructures that appear to possess some sort of crystallinity lead to lower CO_2 permeability.

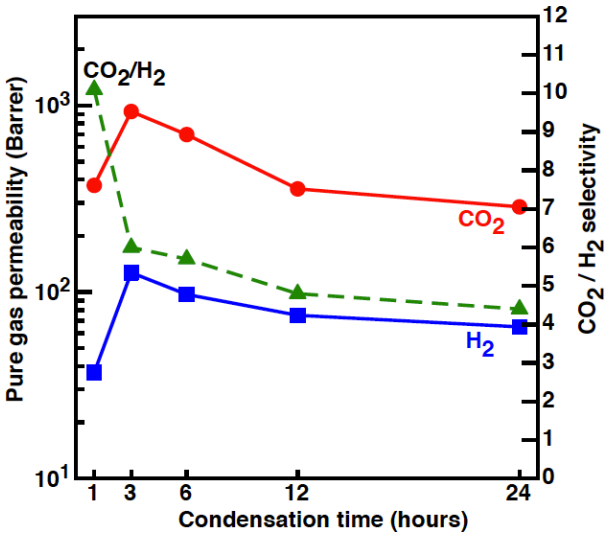

Figure 8.8 Pure gas permeability of $PED_{80}S_{20}$ materials synthesized with 1 – 24 hours of condensation and no ozone pre-treatment modification. The solid circles and squares represent CO_2 and H_2 permeability, respectively. The

triangles represent the CO_2/H_2 gas selectivity of these materials. The lines provide a guide to the eye. Uncertainty in permeability measurements is ± 10%.

EDX analyses in Figure 8.4 indicate that the vicinity of silicate microstructures contain negligible amounts of Si in the polyether matrix. This correlates to a lack of silicate nanostructures that can disrupt polyether chain packing that consequently leads to higher polyether crystallinity that are observed in **Table 8.1**. Hence, the lowest gas permeability is seen for the $PED_{80}S_{20}$-C24h material. Meanwhile, the inorganic phase in the $PED_{80}S_{20}$-C1h material only consists of well-distributed small clusters of silicate nanostructures (~ 15 nm). Hence, a fine balance in size heterogeneity in silicate nanostructures is important in enhancing CO_2 permeability while achieving good CO_2/H_2 selectivity in these organic-inorganic materials that are effectively amorphous at 35 ˚C. Permeation activation energies, E_p, were calculated using the Arrhenius equation $P = P_0 e^{\frac{-Ep}{RT}}$, where P_0 is a pre-exponential factor gas [29, 170], from gas permeability data obtained over the limited temperature range of 30 ˚C to 45 ˚C. The apparent activation energy, E_p, is the sum of the activation energy required for diffusion and the heat of sorption. The E_p values in these organic-inorganic materials are 31– 62 kJ/mol for H_2 and 41 – 51 kJ/mol for CO_2, which are smaller than those of semi-crystalline PEO [77].

Table 8.1 T_g, T_m, crystallinity values (%) of working materials studied in this work. Crystallinity values were calculated with the STAR^e Excellence software

and using an equation $Crystallinity(\%) = \Delta H_f / (\chi_P \times \Delta H_f^0) \times 100\%$, whereby ΔH_f is the apparent heat of fusion per gram of the materials, ΔH^0_f is the thermodynamic heat of fusion per gram of perfect PEO crystal with the value of 188.9 J/g [99] and $\Delta \chi_P$ is the weight percentage of PEO in the $PED_{80}S_{20}$ membranes.

Sample code	T_g (°C)	T_m (°C)	Crystallinity (%)	P_{CO_2} (Barrer)	P_{H_2} (Barrer)	α_{CO_2/H_2}
$PED_{80}S_{20}$-C1h	- 47 °C	30 °C	26 %	373	36	10.1
$PED_{80}S_{20}$-C3h	- 52 °C	34 °C	29 %	928	154	6.0
$PED_{80}S_{20}$-C6h	- 56 °C	35 °C	30 %	698	127	5.7
$PED_{80}S_{20}$-C12h	- 60 °C	37 °C	32 %	357	75	4.8
$PED_{80}S_{20}$-C24h	- 55 °C	37 °C	34 %	286	65	4.4
$PED_{80}S_{20}$-o30s	- 65 °C	28 °C	25 %	984	102	9.6
$PED_{80}S_{20}$-o60s	- 65 °C	24 °C	27 %	1950	185	11
$PED_{80}S_{20}$-o120s	- 63 °C	25 °C	31 %	1363	149	9.1
$PED_{80}S_{20}$-o300s	- 61 °C	26 °C	32 %	813	80	10.1

PEO crystallinity can affect gas transport and separation performance [171, 172]; however owing to the low melting temperature of these PEO-based materials (see Table 8.1) relative to the measurement temperatures used here, crystallinity plays no significant role in the results shown here. As seen in **Figure 8.9**, the condensation duration also influences the glass transition (T_g) and melting temperatures (T_m) of these materials as well as the inorganic phase morphology. When condensation time increases from 1 to 12 hours, T_g decreases from – 47 ˚C to – 60 ˚C. In these materials, polyether chain mobility

is enhanced by the well-distributed small silicate nanostructures that reduce chain packing organization [173]. As most silicate nanostructures agglomerate to form microstructures after 24 hours of condensation, the lack of well-dispersed small silicate nanostructures facilitates hydrogen bonding between the organic phases and slightly increases T_g to – 55 ˚C. The well-dispersed small silicate nanostructures in $PED_{80}S_{20}$-C1h, $PED_{80}S_{20}$-C3h, and $PED_{80}S_{20}$-C12h materials act as obstacles that disrupt polyether chain organization, thus the low T_ms. In $PED_{80}S_{20}$-C24h materials, the inorganic phase consists of large silicate microstructures that only promote localized chain packing disruptions. Overall, organization in the latter materials is more efficient, thus the higher organic phase crystallinity. High organic phase crystallinity increases the diffusion path tortuosity for gas molecules and will reduce gas permeability at temperatures below T_m.

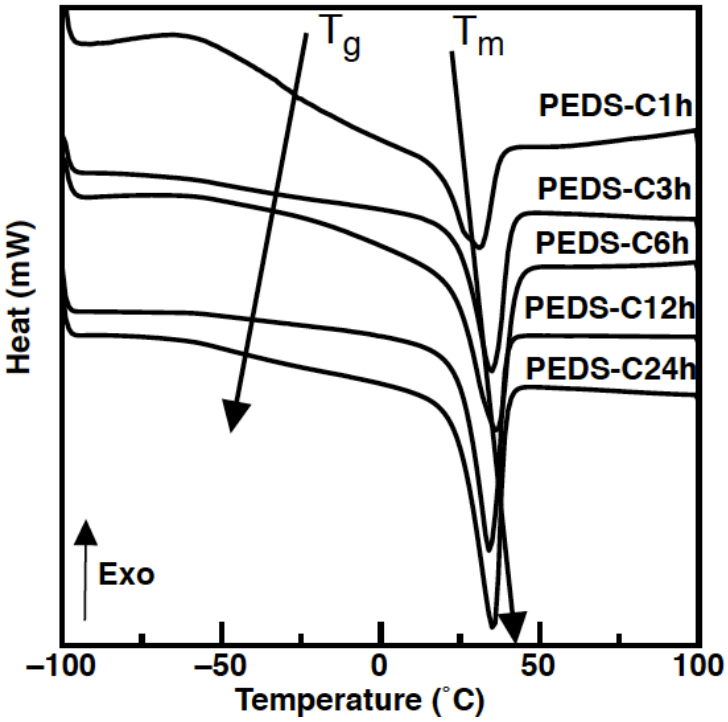

Figure 8.9 DSC plot of the 2nd heating curve of $PED_{80}S_{20}$ materials synthesized using 1 – 24 hours of condensation times. T_g and T_m values were analyzed using the STAR^e Excellence software.

8.3.4 Effect of ozone pre-treatment duration on gas transport properties of organic-inorganic materials

Modifications of the PEDS base materials via ozone pre-treatment and subsequent grafting of alkyl chains significantly enhance gas permeability. The purpose of the ozone pre-treatment is to introduce peroxide moieties onto the main $PED_{80}S_{20}$ main chains, so that subsequent thermal decomposition of these peroxide functional groups can facilitate PEGMA grafting. The degree of modification can be controlled over the ozone pre-treatment duration. The concentration of graft initiation sites, i.e., peroxide moieties on the base PEDS material, decreases with shorter ozone pre-treatment durations [143]. Fewer

graft initiation sites reduce the PEGMA graft content, i.e., the amount of unreacted PEGMA in the synthesis solution will increase. The –OH moieties in these unreacted PEGMA can easily hydrogen bond with water molecules, thus reducing the interaction between water and silicon i.e., reducing the water/silicon ratio [160], thus resulting in agglomerations of silicate nanostructures that are observed in **Figure 8.10**. With lesser graft initiation sites, the only way to increase PEGMA graft content is via a chain propagation mechanism that should yield longer PEGMA chains [159]. Increasing the ozone pre-treatment duration leads to smooth-looking, and compact silicate nanostructures that seem to be regularly spaced apart. Higher PEGMA graft content with longer pre-ozone treatment time [143] reduces the amount of unreacted PEGMA in the synthesis solution, i.e., more water molecules are engaged by the sol-gel reaction during the synthesis procedure [96, 159, 160]. This maintains a high water/silicon ratio that favors a hydrolytic depolymerization, whereby the “nucleation and growth” mechanism is dominant and yields small compact silicate nanostructures [96].

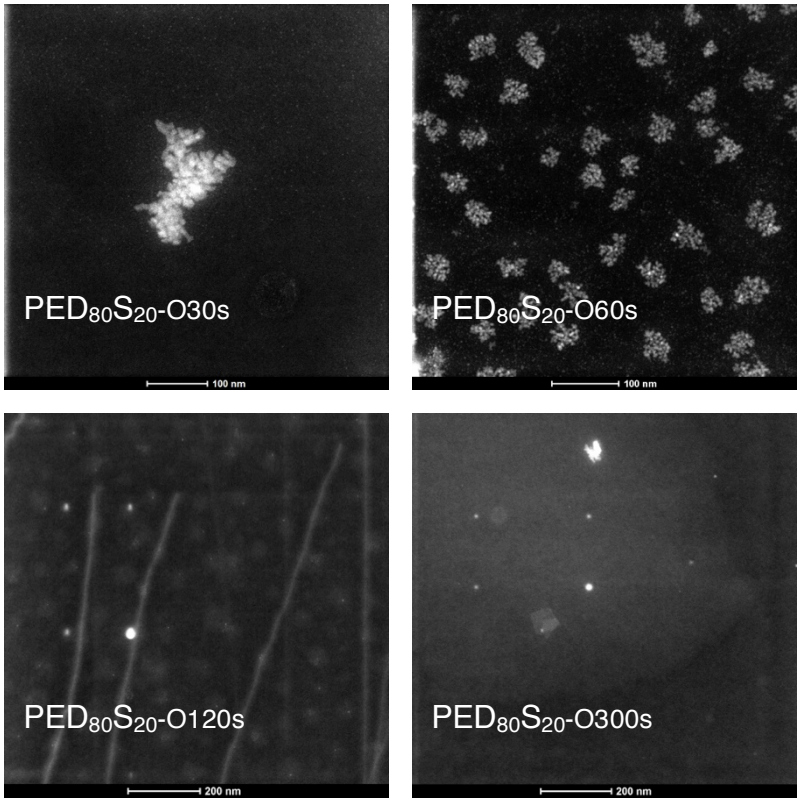

Figure 8.10 STEM images of $PED_{80}S_{20}$ materials synthesized with 1 hour of condensation; then ozone pre-treatments for 30 to 300 seconds, followed by reaction with 43 wt.% of PEGMA. As ozone pre-treatment durations increase, the silicon-basde nanostructure morphology transforms from a nanocluster that resembles like a flower (after 30 and 60 seconds of ozone pre-treatment) to regularly spaced nanodots (after 120 seconds) and to high intensity nanodots in the background of a large low intensity silicon-based patch.

Attributing to the morphological changes in the inorganic phase, the CO_2 permeability of ozone-modified membranes increases with longer ozone pre-treatment durations in **Figure 8.11**. The ideal ozone pre-treatment duration is 60 seconds whereby 15 nm silicate nanostructures randomly agglomerate into flower-like 50 nm silicate nanoclusters. Such silicate nanoclusters seem to surround some organic material and are required for enhancing CO_2 permeability. The increment in H_2 permeability is larger in proportion to the

enhancements in CO_2 permeability; thus, the lower CO_2/H_2 selectivity that is observed in materials that have undergone prolonged periods of ozone pre-treatments. The ideal synthesis protocol for high CO_2 permeability and good CO_2/H_2 selectivity appears to be the combination of 1 hour of condensation, 60 seconds of ozone pre-treatment and 20 wt. % of PEGMA grafted onto a base $PED_{80}S_{20}$ material.

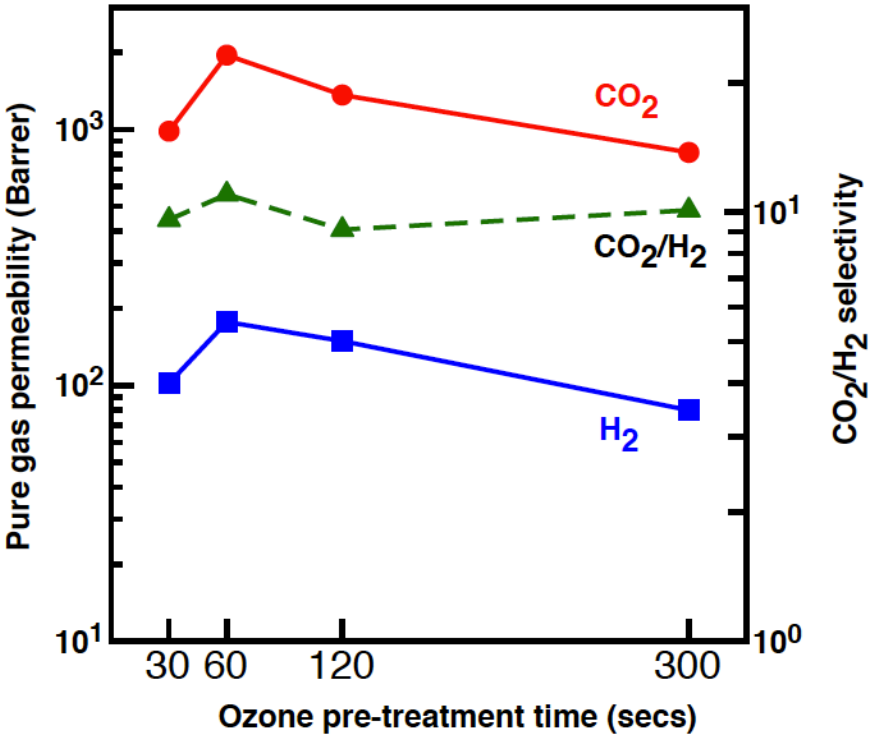

Figure 8.11 Pure gas permeability of $PED_{80}S_{20}$ materials synthesized with 1 hour of condensation; then ozone pre-treatments for 30 to 300 seconds, followed by reaction with 43 wt.% of PEGMA. The solid squares and circles represent CO_2 and H_2 permeability, respectively. The empty inverted triangles represent the CO_2/H_2 gas selectivity of these materials. The lines provide a guide to the eye. Uncertainty in permeability measurements is ± 10%.

8.4. Summary

In **Figure 8.12**, the CO_2 transport properties of optimized nanohybrid

membrane exceed those of other rubbery CO_2-philic membranes [24, 29, 82, 123, 147, 174], while maintaining similar CO_2/H_2 selectivity. The CO_2 permeability of this ideal nanohybrid membrane is in the same range of CO_2 permeability as PDMS [38], thus it is comparable to PDMS, albeit with a higher CO_2/H_2 selectivity. The effects of hydrolysis, condensation and modification durations greatly impact the silicate nanostructures morphology and distribution that consequently play important roles in determining CO_2 permeability. Silicate structure size heterogeneity in these nanohybrid membranes appears to be the key to high CO_2 permeability and good CO_2/H_2 selectivity. Ideally, silicate nanostructures with sizes up to 50 nm surrounded by 5 – 15 nm silicate nanostructures is the preferred inorganic phase morphology that yields optimal nanohybrid membranes. As this work illustrates the relationship between synthesis and modification conditions, and gas permeability, tailored nanohybrid membranes can be easily fabricated according to requirements. Moreover, this work has also provided an insight on inorganic phase morphological changes in sol-derived materials that are commonly used in many other applications.

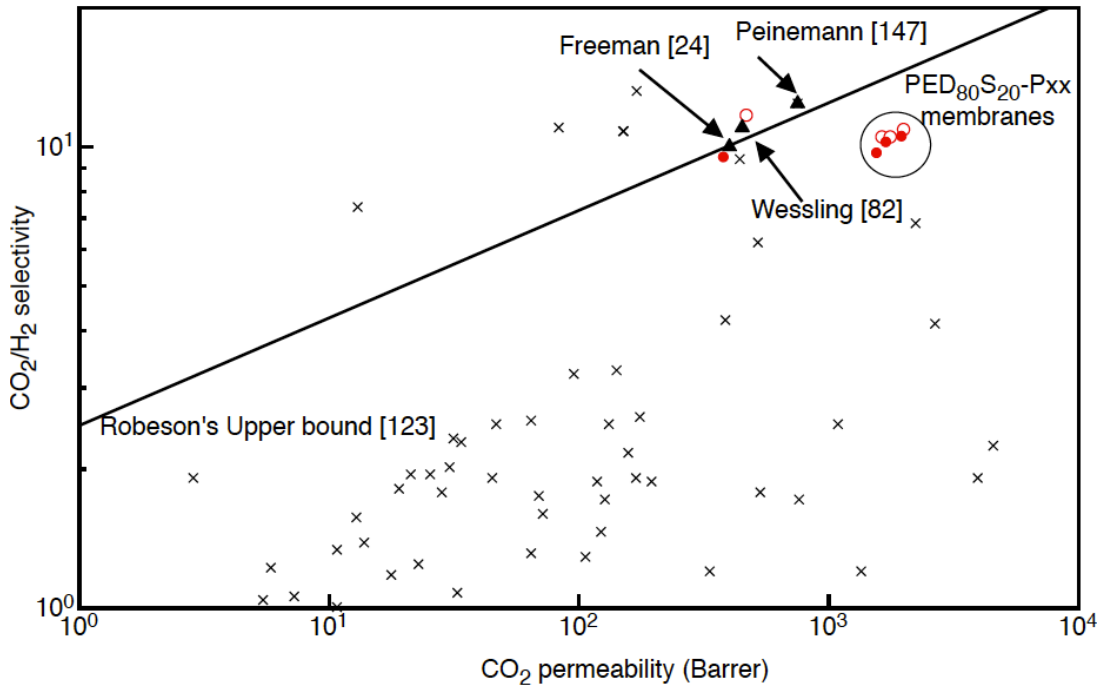

Figure 8.12 A comparison of the CO_2/H_2 separation performance of our nanohybrid membranes with Robeson's upper bound [123] and other membrane materials described in recent literature [24, 29, 82, 123, 147, 174]. Although the performance of these nanohybrid membranes lies below the upper bound line, the tremendous improvement in CO_2 permeability whilst maintaining high CO_2/H_2 selectivity renders these materials attractive for industrial applications.

CHAPTER NINE:

THE EFFECTS OF MODIFICATION NATURE AND SIDE CHAIN LENGTH ON GAS PERMEABILITY IN NANOHYBRID MEMBRANES FOR FLUE GAS APPLICATIONS

9.1 Introduction

Sol-derived nanohybrid membranes display desirable CO_2 transport properties whilst overcoming the issue of nanoparticle agglomeration [29, 93, 94, 159, 160]. Nanohybrid membranes with high CO_2-affinity are useful for applications like CO_2 capture while purifying syngas (H_2) and possibly, flue gas (N_2). Additionally, the sol-gel approach facilitates easy control over synthesis parameters that consequently determine the gas transport and separation properties of the nanohybrid membrane. These synthesis parameters include the organic-inorganic ratio, the water/silicon ratio, the hydrolysis, condensation durations and pertaining to this dissertation, modification durations, and the nature of the graft type.

Attuning these synthesis parameters yields nanohybrid membranes with varying gas separation performances. For instance, Shao and Chung demonstrated that higher CO_2 permeability is a function of increasing organic-inorganic ratio i.e. higher polyether content [29]; while Sforça and Lim demonstrated that the effects of the polyether content on gas permeability [29, 93, 94, 159, 160]. Mogri and Paul studied the effects of side-chain length on gas permeation in poly (alkyl (meth) acrylate)s membranes [175, 176]. A permeation switch that is dependent on crystallinity at different temperatures was observed. Meanwhile, Chapters 6 and 8 of this dissertation have demonstrated the effects of side-chain grafts and the nature of the side-chain grafts on CO_2 and H_2 permeability,

respectively. Other synthesis parameters that play important roles in determining the gas transport and separation properties of sol-derived nanohybrid membranes are the modification nature and the side chain length.

The nature of material modification depends on changes in the molecular structure. Grafting, functionalization [159, 160, 177, 178], and cross-linking [24, 75, 78-80] chemically modifies the molecular structure, while physical blending mainly affects the physical attributes of the membrane material, leaving the molecular structure intact [86, 179]. Yave et al. investigated the effects of blending low molecular weight polyether-based plasticizers in PEBAX®, a commercially available (poly(amide-b-ethylene oxide) copolymer) [179]. The plasticizers enhanced CO_2 permeability by increasing relative FFV content and CO_2 solubility coefficients. In this chapter, the effects of modification nature and side chain length on CO_2, H_2, and N_2 permeability are studied.

9.2 Materials and experimental details

9.2.1 Materials and membrane fabrication

The base organic-inorganic membrane material was derived from a sol-gel approach detailed in Chapter 6, whereby hydrolysis and condensation durations were 30 minutes and 1 hour, respectively. The base membrane consisted of a propylene oxide end-capped polyethylene glycol that is commercially known as Jeffamine® ED-2003 (M_w = 2000 g/mole) and 3-glycidyloxypropyltrimethoxysilane (GOTMS: M_w = 236 g/mole). The base material consisted of 80 wt.% polyether diamine and 20 wt.% alkoxysilane and is coded $PED_{80}S_{20}$. Other organic-inorganic ratios used in this chapter of the work include 75wt.% polyether diamine and 25 wt.% alkoxysilane, and 50 wt.% polyether diamine and 50 wt.% alkoxysilane. These base materials were coded $PED_{75}S_{25}$ and $PED_{50}S_{50}$, respectively.

For the physically blended membrane material, poly ethylene glycol methacrylate (PEGMA: M_w = 360 g/mole) was used. Prior condensation, 43 wt.% of PEGMA was mixed with the base $PED_{80}S_{20}$ material in the solution phase and stirred for 1 hour at room temperature. Upon condensation and solvent evaporation, an organic-inorganic membrane was formed. This membrane is coded $PED_{80}S_{20}$-P_{43}(blend) in this dissertation. The subscript represents the amount of PEGMA blended into the $PED_{80}S_{20}$ base material. PEGMA (M_w = 360 g/mole) was also physically blended with $PED_{75}S_{25}$ and

$PED_{50}S_{50}$ base materials. These membranes are coded $PED_{75}S_{25}$-P_{43}(blend) and $PED_{50}S_{50}$-P_{43}(blend), respectively.

In the case of chemically grafted membranes studied in this chapter, 20 wt.% of poly ethylene glycol methacrylate (PEGMA: M_w = 550 g/mole) was grafted onto the $PED_{50}S_{50}$, $PED_{75}S_{25}$, and $PED_{80}S_{20}$ base materials using the protocol described in Chapter 6. Membranes grafted with PEGMA: M_w = 550 g/mole are coded $PED_{50}S_{50}$-$P_{20}^{(550)}$, $PED_{75}S_{20}$-$P_{25}^{(550)}$, $PED_{80}S_{20}$-$P_{20}^{(550)}$, respectively. The superscript denotes the molecular weight of PEGMA used. Additionally, all other organic-inorganic materials and nanohybrid materials studied in Chapters 6, 7, and 8 were also characterized for flue gas applications.

9.2.2 Membrane characterization

ATR-FTIR and XPS were used to validate the chemical structure of $PED_{80}S_{20}$-P_{20}(blend) and $PED_{80}S_{20}$-$P_{20}^{(550)}$ membrane materials. The subscript represents the amount of PEGMA grafted onto the $PED_{80}S_{20}$ base material, while the superscript denotes the molecular weight of the PEGMA. Bulk PALS was used to characterize the relative FFV content of these materials. The pure gas permeabilities were determined using the constant volume-variable pressure method discussed in Section 3.9.1.

9.3 Results and Discussion

9.3.1 Chemical structure of membrane materials

The chemical structures of the membrane materials studied in this chapter were verified using XPS and ATR-FTIR analyses. **Table 9.1** shows the XPS data of these membrane materials. The C-C peak is referenced at 285 eV. The presence of PEGMA grafts in $PED_{80}S_{20}$-$P_{20}^{(550)}$ nanohybrid materials is verified by the detection of a binding energy peak at 288 eV. This corresponds to the non-carbonyl carbon atom in C-O-C=O [156]. The peak at 285.5 eV denotes the presence of small amounts of C=C bonds [156]. C=C bonds are found in acrylate groups in this work. Hence, indicating a small amount of unreacted PEGMA in the $PED_{80}S_{20}$-$P_{20}^{(550)}$ nanohybrid materials. Meanwhile, in the XPS data of PEDS-P_{43}(blend) materials, there is a higher content of C=C bonds. This is ascribed to the unreacted acrylate bonds in PEGMA that were physically blended with the PEDS base material.

Table 9.1 XPS analysis of $PED_{80}S_{20}$, $PED_{80}S_{20}$-$P_{20}^{(550)}$, and $PED_{80}S_{20}$-P_{43} (blend) membrane materials.

Binding energy (eV)	Functional group	PEDS	PEDS-$P_{20}^{(550)}$	PEDS-P_{43}(blend)
		%	%	%
285 eV	C—C	30.3	28.2	17.3
285.5 eV	C=C	-	1.2	8.6

284.6 eV	O—C—C*	10.8	12.1	10.7
283.8 eV	C—O—C	10.8	11.8	10.5
283.4 eV	C—Si	1.9	1.0	1.8
287.4 eV	C—N	9.6	2.7	2.4
288 eV	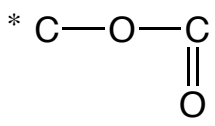	-	9.8	10.8
531.4 eV	C—O—C	25.1	6.0	22.9
532.4 eV	C—OH	2.2	1.1	0.8
533.9 eV	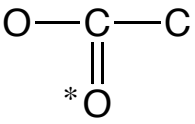	-	14.4	7.8
532.8 eV	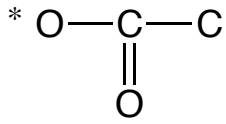	-	14.8	8.1

From the ATR-FTIR spectra in **Figure 9.1**, signature peaks of C-O-C bonds in the PPO-PEO-PPO segment and Si-O-Si bonds in the silicate nanostructures appear at 1105 cm^{-1} and 1258 cm^{-1}, respectively [164, 165]. A peak at 1700 cm^{-1} can be observed in the FTIR spectra of $PED_{80}S_{20}$-P_{20}, $PED_{80}S_{20}$-$P_{20}^{(550)}$ and $PED_{80}S_{20}$-P_{43}(blend) materials. This peak correlates to the O-C=O ester stretch of PEGMA [166]. The asymmetrical peak at around 1650 cm^{-1} in the $PED_{80}S_{20}$-P_{43}(blend) materials could be ascribed to unreacted C=C bonds in acrylate moieties [156].

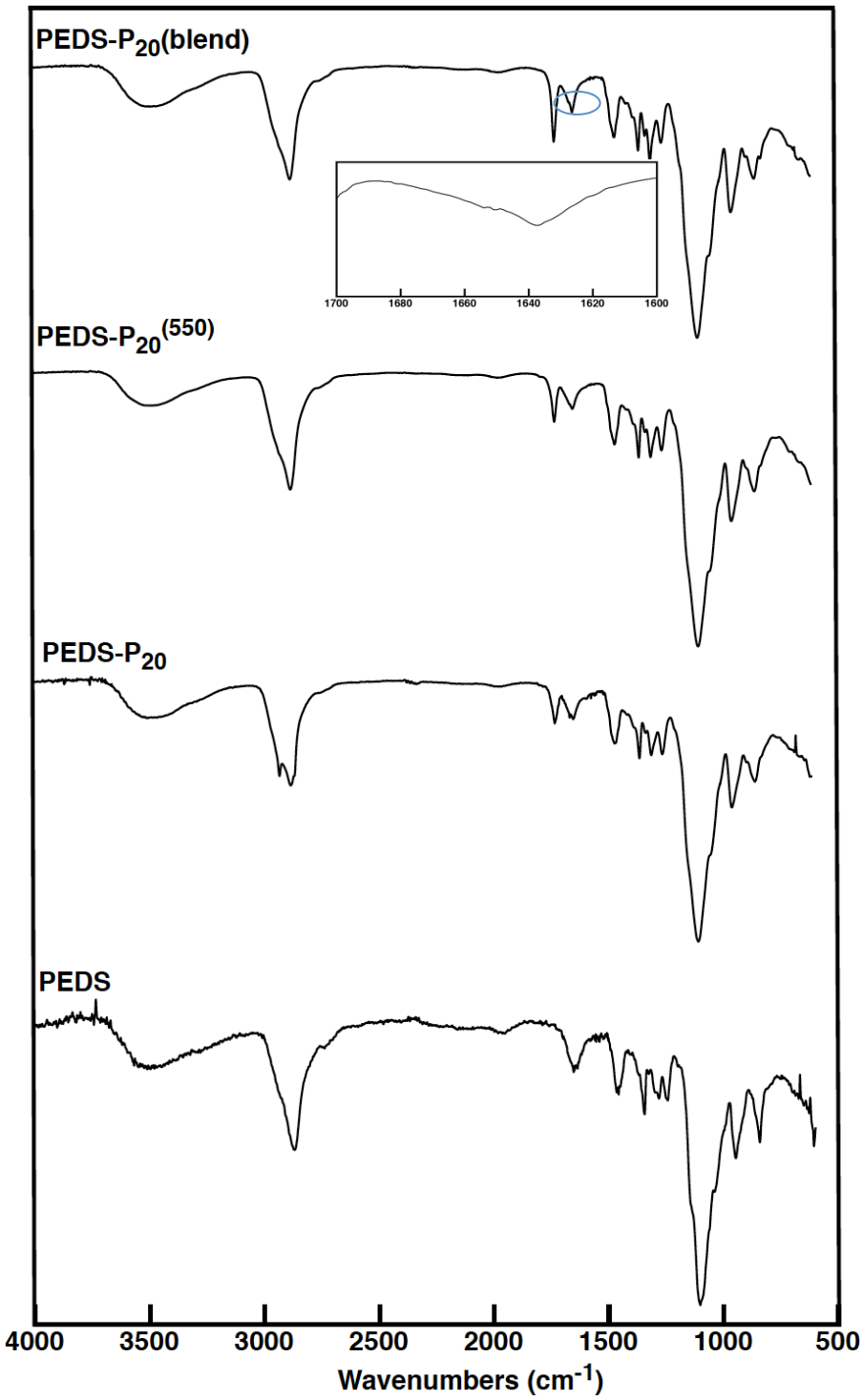

Figure 9.1 ATR-FTIR spectra of $PED_{80}S_{20}$, $PED_{80}S_{20}$-P_{20}, $PED_{80}S_{20}$-$P_{20}^{(550)}$ and $PED_{80}S_{20}$-P_{43}(blend) materials. $PED_{80}S_{20}$-P_{20} materials are included for comparison. The inset shows an enlarged area of the FTIR spectrum of a PEDS-P_{43}(blend) material.

9.3.2 Blends VS grafts - Gas permeability and permselectivity

Table 9.2 shows that gas permeability in $PED_{80}S_{20}$-P_{43}(blend) materials is lower than that of pristine $PED_{80}S_{20}$ materials. The lower CO_2 permeability can be attributed to the lower relative FFV content in physically blended materials. As the unreacted PEGMA additives occupy the empty spaces within the host matrix i.e. the base material (as shown in **Figure 9.2**), the relative FFV content will be reduced. Bulk PALS data in **Table 9.3** validates the aforementioned hypothesis. The relative FFV content and V_f size is smaller in $PED_{80}S_{20}$-P_{43}(blend) membrane materials. can potentially reduce diffusion pathways gas molecules, in particular the large CO_2 gas molecules.

Table 9.2 Pure gas permeability of $PED_{80}S_{20}$, $PED_{80}S_{20}$-P_{20}, $PED_{80}S_{20}$-$P_{20}^{(550)}$ and $PED_{80}S_{20}$-P_{43}(blend) materials.

Sample code	P_{CO_2} (Barrer)	P_{H_2} (Barrer)	P_{N_2} (Barrer)	CO_2/H_2	CO_2/N_2
$PED_{80}S_{20}$	377	39	9.8	9.7	38.5
$PED_{80}S_{20}$-P_{20}	1950	185	35	10.5	55.7
$PED_{80}S_{20}$-$P_{20}^{(550)}$	2080	198	37	10.5	56.2
$PED_{80}S_{20}$-P_{43}(blend)	307	32	7.9	9.6	38.9

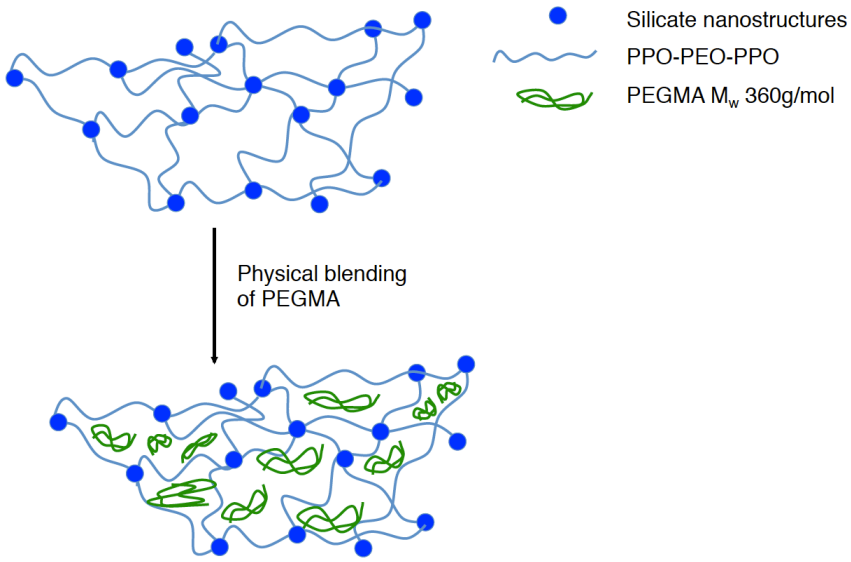

Figure 9.2 A cartoon depicting the filling up of free volume content in $PED_{20}S_{20}$ base materials by physically blending low molecular weight PEGMA additives.

Table 9.3 Average free volume sizes and relative FFV content in (i) $PED_{80}S_{20}$, (ii) $PED_{80}S_{20}$-P_{20}, (iii) $PED_{80}S_{20}$-$P_{20}^{(550)}$ and (iv) $PED_{80}S_{20}$-P_{43}(blend) materials.

	τ_3 (ns)	Ave. V_f size (Å)	I_3 (%)	Relative FFV content (%)
i	2.45	3.33	12.7	3.2
ii	2.59	3.35	12.7	3.6
iii	2.65	3.39	13.7	3.8
iv	2.37	3.17	7.6	1.9

Compared to $PED_{80}S_{20}$-P_{20} materials, CO_2 permeability in $PED_{80}S_{20}$-P_{43}(blend) materials are lower by nearly 6 folds. STEM images in **Figure 9.3** reveal that the silicate nanostructures in $PED_{80}S_{20}$-P_{43}(blend) membranes are similar to

those observed in $PED_{80}S_{20}$-P_{20} materials (Figure 6.9) i.e. the effects of Si-O-Si networks on S_{CO_2} coefficients should be similar as well. Hence, the D_{CO_2} coefficients in $PED_{80}S_{20}$-P_{43}(blend) membranes should be significantly lower. This can be validated by comparing the relative FFV content of these two materials. The relative FFV content in $PED_{80}S_{20}$-P_{43}(blend) membranes is approximately half the amount in $PED_{80}S_{20}$-P_{20} materials.

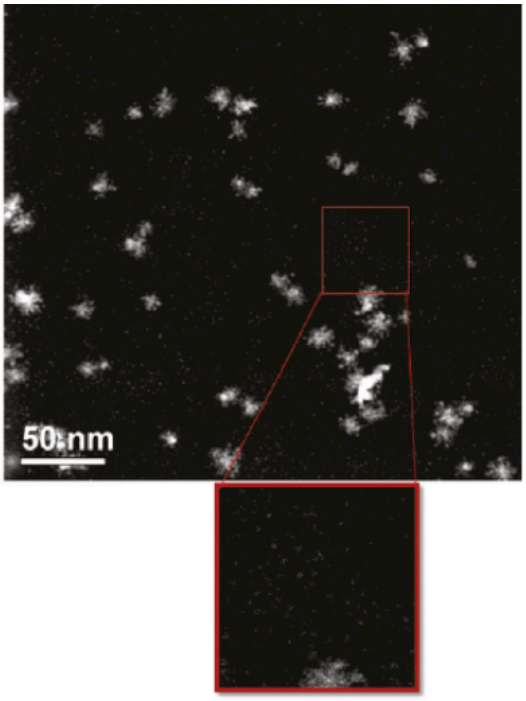

Figure 9.3 STEM image of $PED_{80}S_{20}$-P_{43}(blend) membrane materials. A magnification of the image shows the dispersion of small silicate nanostructures.

The higher CO_2 permeability in $PED_{80}S_{20}$–P_{20} materials (when compared to $PED_{80}S_{20}$-P_{43}(blend) materials) is correlated to the difference in the role of PEGMA. With chemical grafting, the PEGMA side chains inhibit the packing of PEDS main chains i.e. suppressing crystallinity while creating more free volume

content (**Figure 9.4**); while in physical blending, PEGMA chains fill up the free volume content (Figure 9.2). Therefore with longer PEGMA grafts i.e. $PED_{80}S_{20}$-$P_{20}^{(550)}$ materials, the relative FFV content and consequently the gas diffusivity coefficients will be larger when compared to $PED_{80}S_{20}$-P_{20} materials. Thus, the largest gas permeability is observed in $PED_{80}S_{20}$-$P_{20}^{(550)}$ materials (Table 9.2).

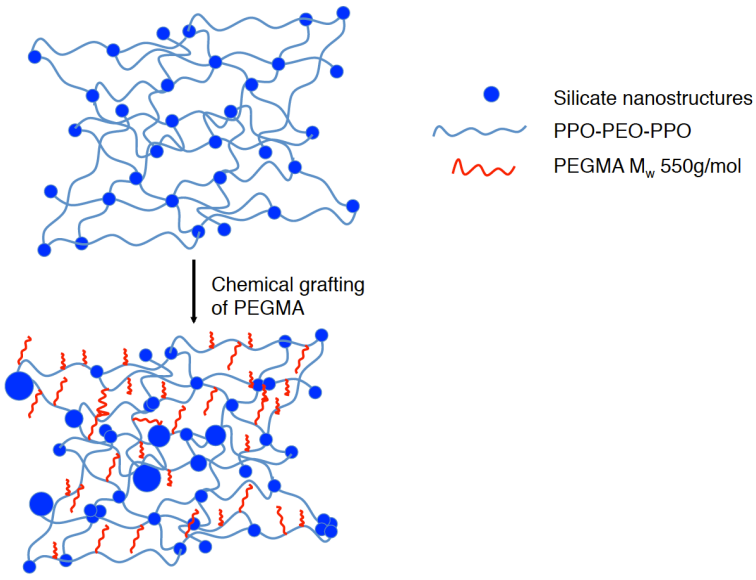

Figure 9.4 PEGMA grafts can increase the relative FFV content in PEDS materials. Additionally, it can also influence the morphology of the silicate nanostructures.

9.3.3 N_2 permeability of nanohybrid materials

Thus far, nanohybrid rubbery membranes studied in this dissertation have been characterized for CO_2/H_2 separation i.e. syngas purification. **Figure 9.5** compares the CO_2 permeability and CO_2/H_2 selectivity of these nanohybrid membranes with Robeson's upper bound line [123]. Although the CO_2

permeability of these nanohybrid membranes are significantly higher than other rubbery materials [24, 75, 78, 79, 82, 94, 147, 179, 180], the CO_2/H_2 permselectivity of these nanohybrid membranes remain at similar levels to those observed in other rubbery materials. The significantincrease in CO_2 permeability can be ascribed to enhanced CO_2 solubility and diffusivity coefficients. CO_2 solubility coefficients are enhanced via sorption with Si-O-Si bonds [160]; while CO_2 diffusivity coefficients are improved by inhibiting the crystallinity in the organic phase [159] i.e. a higher relative FFV content. The higher relative FFV content also contributes to significant increase in H_2 permeability. Thus, CO_2/H_2 selectivity values remain similar to other rubbery materials.

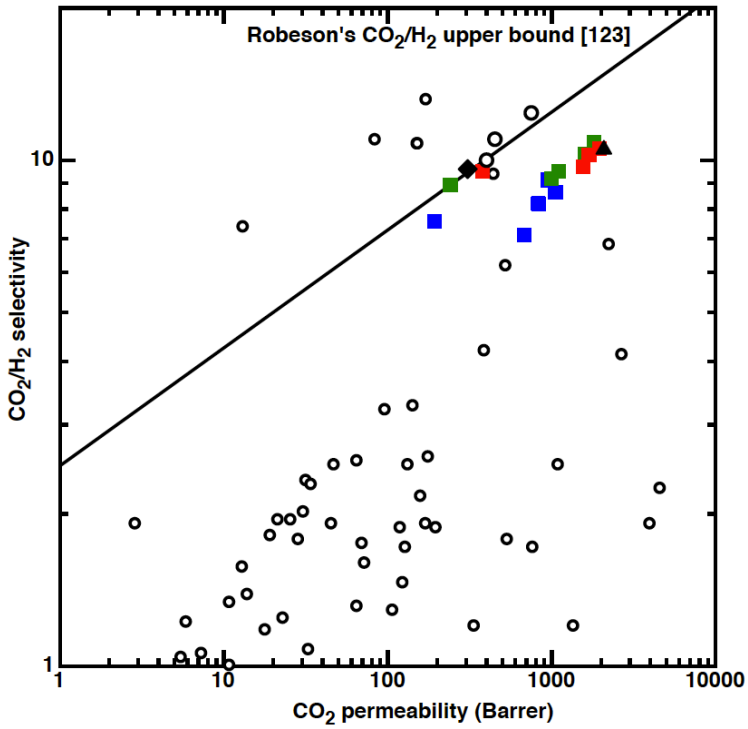

Figure 9.5 A comparison of CO_2/H_2 separation of nanohybrid materials studied in this work with other materials. The blue squares represent the $PED_{50}S_{50}$-P_{xx}

series; green squares represent the $PED_{75}S_{25}$- P_{xx} series; and the red squares represent the $PED_{80}S_{20}$- P_{xx} series. The black diamond and triangle represent $PED_{80}S_{20}$- P_{43} (blend) and $PED_{80}S_{20}$- P_{20} $^{(550)}$ membranes, respectively.

Figure 9.6 compares the CO_2/N_2 permselectivity of the nanohybrid rubbery membranes studied in this dissertation with Robeson's upper bound for CO_2/N_2 separations [123]. The CO_2/N_2 separation performance of these nanohybrid membranes surpasses most other membranes in the Robeson plot. This can be attributed to significant enhancements in CO_2 permeability whilst minimizing the increment in N_2 permeability. The condensability of N_2 gas molecules is significantly lower than that of CO_2 gas molecules (Table 2.1); hence N_2 solubility coefficients should be generally lower. Xia et al. have shown that N_2 sorption is significantly lower than CO_2 sorption in identical nanohybrid membranes [174, 181]. As gas separation in rubbery reverse-selective membranes, in particular CO_2 separation is primarily governed by solubility coefficients; enhanced CO_2 solubility coefficients alongside low N_2 solubility coefficients in the nanohybrid membranes studied in this dissertation yield high CO_2/N_2 selectivity.

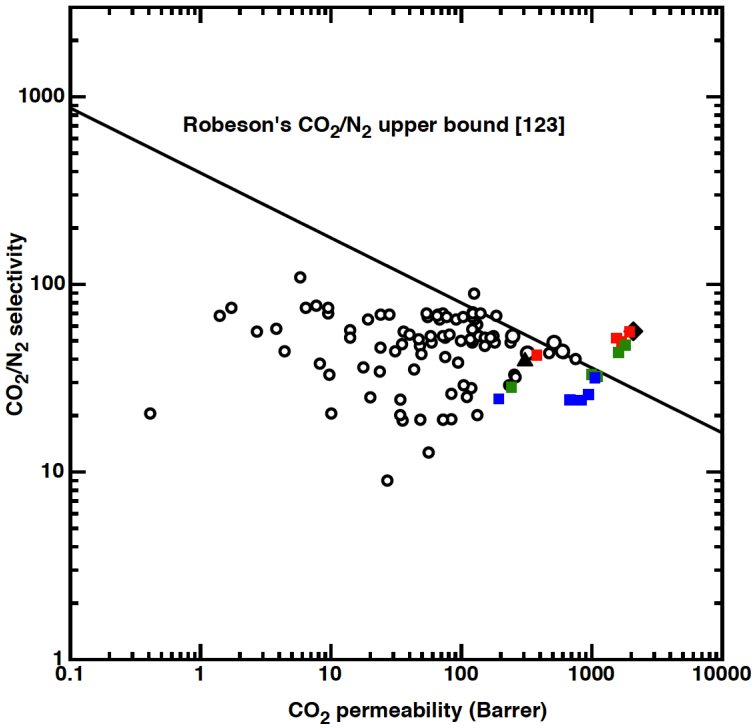

Figure 9.6 A comparison of CO_2/N_2 separation of nanohybrid materials studied in this work with other materials. The blue squares represent the $PED_{50}S_{50}$-P_{xx} series; green squares represent the $PED_{75}S_{25}$- P_{xx} series; and the red squares represent the $PED_{80}S_{20}$- P_{xx} series. The black diamond and triangle represent $PED_{80}S_{20}$- P_{43} (blend) and $PED_{80}S_{20}$- P_{20} [(550)] membranes, respectively.

9.4 Summary

The physical blending of large amounts of PEGMA additives into organic-inorganic materials does not improve gas permeabilities of the organic membranes. High contents of PEGMA additives reduce the relative FFV content and may possibly lower gas diffusivity coefficients. On the other hand, by chemically grafting longer PEGMA monomers onto the main chains of an organic-inorganic material, gas permeabilities can be significantly improved. This is largely due to the inhibition of material crystallinity and the influence of PEGMA grafts on silicate nanostructures that also contribute to CO_2

permeation. With enhanced CO_2 permeation and comparatively low H_2 permeation, these nanohybrid membranes are capable of performing high levels of CO_2/H_2 separation. Meanwhile these membranes can also be used for CO_2 /N_2 separation.

CHAPTER TEN:

CONCLUSIONS AND RECOMMENDATIONS

10.1 Conclusions

Optimal CO_2 separation membranes can be obtained by innovative material modifications on traditional polymeric materials. Modified glassy materials display efficient CO_2 transport and separation capabilities, whilst the work on modified organic-inorganic rubbery materials sheds new light on the relationship between synthesis and modification conditions and gas separation. The mild modification technique used on organic-inorganic rubbery materials yield nanohybrid membranes with high CO_2 permeability and CO_2/light gas selectivity.

10.1.1 Vapor phase modifications on dense film glassy membranes

Although vapor phase modifications have been used on a range of materials for other applications, this project pilots the use of this simple and elegant modification technique to enhance the gas separation performances of a fluorinated polyimide dense film gas separation membrane. Upon vapor phase modification, the membrane structure adopts a physical configuration similar to asymmetric membranes, whereby only the topmost layer is densified while the inner layers remain intact. Compared to pristine fluorinated polyimides, the H_2/CO_2 selectivity of vapor phase modified membranes is higher.

10.1.2 Vapor phase modifications on hollow fiber glassy membranes

To demonstrate the viability of the vapor phase modification technique, this modification technique was also used to modify hollow fiber gas separation membranes fabricated from different types of polyimides. The vapor phase modification technique minimized the deterimental effects of solvent swelling in hollow fiber membranes, hence maintaining structural integrity and gas separation performances. Additionally, a variation of the batch vapor phase modification technique was also used to modify various polyimide hollow fibers. Results showed that both techniques produced identical gas permeability and gas separation performances.

10.1.3 Effects of alkyl chain content on gas separation in rubbery nanohybrid membranes

The combination of high CO_2-affinity organic and inorganic components via a sol-gel approach has yielded an organic-inorganic material with superior CO_2 permeability and CO_2/H_2 selectivity that is comparable to state-of-the-art organic rubbery materials [24]. Through simple material modifications, the CO_2 permeability of the base organic-inorganic material was significantly enhanced from 378 Barrer to 1950 Barrer (an increment of 5 folds). The significant increment in CO_2 permeability could be ascribed to larger S_{CO_2} and D_{CO_2} coefficients due to the changing morphology of the silicate nanoparticles.

Morphological changes in the silicate nanoparticles can be ascribed to changes in the synthesis parameters and conditions.

10.1.4 Effects of water/silicon ratio, organic/inorganic ratio, and graft content on gas separation in rubbery nanohybrid membranes

With increased PEGMA content during the synthesis solution of the nanohybrid materials, the morphology of the inorganic phase transforms from smooth looking nanoparticles into rough-edged flowery nanoclusters. The presence of unreacted PEGMA in the synthesis solution forms hydrogen bonds with water molecules present in the solvent. Hence, reducing the concentration of "free" water to engage in the sol-gel process i.e. water/silicon ratio is reduced. According to Brinker's work, a reduction in water/silicon ratio shifts the growth mechanism of the inorganic phase from a nucleation and growth process that yields smooth nanoparticles to an agglomeration process that yields rough-edged nanoclusters [96]. As the inorganic phase becomes larger, the CO_2 transport behaviors of the silicate structures resemble that of highly permeable silicon-based rubbery (PDMS) and glassy (PTMSP) polymers. Hence, the observed high CO_2 permeability in the nanohybrid membranes studied in this project.

Gas permeability increases with increments in the organic/inorganic ratio of these nanohybrid membranes. In this work, 1) increasing the polyether diamine

content during the synthesis of the base organic-inorganic material, or 2) increasing the PEGMA graft content tunes the organic/inorganic ratio. Higher polyether content yields higher gas permeability and CO_2/light gas selectivity.

10.1.5 Effects of alkyl chain and modification nature on gas separation in rubbery nanohybrid membranes

The gas permeability of these nanohybrid membranes is also dependent on the nature of the alkyl chain. When short alkyl chains like butyl methacrylate were grafted onto the organic-inorganic base material, gas permeability and selectivity decreased. The lower gas transport and separation performances are due to the lower ether oxygen content in butyl methacrylate when compared to PEGMA. With lower ether oxygen content, CO_2 solubility coefficients will be reduced. Additionally, hydrogen bonding between unreacted butyl methacrylates and water molecules during synthesis is significantly reduced with lower ether oxygen content. As a result, the growth process of the inorganic phase remains nearly unchanged i.e. a nucleation and growth process that forms smooth-looking nanoparticles. With longer PEGMA monomers (M_w 526), gas permeability is further enhanced to about 2080 Barrer, whilst maintaining a CO_2/H_2 selectivity of 10.5.

Meanwhile, the modification nature of the nanohybrid membranes also plays an important role in determining gas transport and separation properties. When

high contents of PEGMA are physically blended with the base organic-inorganic material, excessive PEGMA could occupy the free volume in the base material. This was validated using bulk and slow beam PALS. With reduced relative FFV content, CO_2 diffusivity coefficients that are consequently reduced leads to lower CO_2 permeability. As light gas permeation across these materials are mainly dependent on free volume content, lower relative FFV content would lead to the observed lower H_2 permeability.

10.1.6 Effects of hydrolysis, condensation, and modification duration on gas separation in rubbery nanohybrid membranes

Besides altering the molecular structure or chemical composition of the nanohybrid membranes, a simple and straightforward approach to attune gas transport and separation properties of these hybrid materials is to vary the hydrolysis and condensation durations during the synthesis of the base organic-inorganic material.

By increasing the hydrolysis duration from 30 minutes to 24 hours, cross-linking occurs between the Si-O-Si bonds i.e. gelation, inferring the growth of silicate nanoparticles. Gas permeability and selectivity decreased with longer hydrolysis periods. In relation to the theory of Ostwald ripening, larger nanoparticles tend to possess lower surface energy, which may consequently lead to lower CO_2 sorption capabilities. As Patil et al. reported that cross-linking

reduces the free volume content in materials [182], the cross-linking in the silicate nanoparticles may also lead to lower free volume content. Hence, lower CO_2 permeability resulted from reduced solubility and diffusivity coefficients. The decrease in H_2 permeability can be accounted by the possible decrease in free volume content.

When condensation durations increased from 1 hour to 3 hours, gas permeability increased. Subsequently, with longer condensation durations (up to 24 hours), gas permeability decreased. From HAADF-STEM tomographs of materials synthesized from 1-3 hours of condensation durations, small silicate nanoparticles are finely dispersed alongside larger silicate nanoclusters within the polyether matrix. This dispersion of heterogeneously sized silicate nanoparticles is the key to attaining high CO_2 permeability.

The intricate combination of synthesis conditions and mild modification conditions are important to obtaining nanohybrid membranes with high CO_2 permeability at near ambient conditions. Although the uses of rubbery materials in industrial gas separations are rare, the results of this work have pushed the boundaries of CO_2 permeation using rubbery materials. With the emphasis on green technology, it is strongly believed that with superior CO_2 transport and CO_2/N_2 separation properties such membranes are potentially important for

futuristic gas separation applications, especially in the field of flue gas separations.

10.2 Recommendations

10.2.1 Extension of vapor phase modification to other materials

Through the use of a common technique like vapor phase modification, this project has demonstrated its advantages to enhance gas separation properties of various polyimides. The choice of cross-linkers is dependent on the membrane material. In this project, only one combination (amine-based cross-linker and a polyimide) has been studied. To further extend this modification technique to an industrial application, other combinations must be studied as well. For instance, it would be interesting to study the effects of vapor phase modification on PDMS-the most permeable rubbery material, or PTMSP-one of the most permeable polymer known. In these cases, the choice of cross-linkers would have to be varied according to the respective polymer's chemistry with various cross-linkers.

10.2.2 In-depth studies on effect of water vapor and other acidic gases on CO_2 permeability in modified materials

Most of the gas permeation characterization tests in this project were done using pure gases or mixed gases containing two gaseous components. Such ideal cases are only confined to lab-scale research. In real-life applications, water vapor is common in gas mixtures that contains CO_2 and more than two gaseous components including toxic and acidic gases like CO, NO_x, SO_x and H_2S. The presence of other acidic gases may alter the CO_2 permeability of

these nanohybrid membranes. Meanwhile, it would also be interesting to characterize these materials at higher operating temperatures (that resemble real-life operating conditions). Although there were some preliminary characterizations on the effects of water vapor on gas permeability in some nanohybrid membranes in this work, these results are insufficient to conclude the actual gas separation performances of these materials in real-life applications.

10.2.3 The role of silicate nanoparticles in nanohybrid membranes

This work has identified that the silicate nanoparticles contribute to CO_2 transport properties. However, the combination of two CO_2-philic components (alkoxysilane and polyether) makes it difficult to isolate the effects of silicate nanoparticles on CO_2 permeation. To study the independent effects of silicate nanoparticles on CO_2 permeation, a polymer with low CO_2 permeability should be used. Additionally, different types of alkoxysilanes could be used to fabricate nanohybrid membranes. The different functional moieties may result in different silicate morphologies that subsequently affect gas permeation.

10.2.4 Hollow fiber membranes fabricated from nanohybrid materials

There are limited literature working on the development of PEO-based materials into hollow fiber membranes, which are more favorable for industrial applications due to its high flux and self-supporting structure. The slow phase

inversion of PEO in most solvents makes it challenging to fabricate it as asymmetric or composite membranes via dry-jet wet-spinning. To date, only Suzuki et al. have fabricated PI-PEO composite hollow fiber membranes via dry-jet wet-spinning process [183]. As these nanohybrid membranes are insoluble in most solvents after condensation, there is a possibility that these materials are fabricated in the form of hollow fibers. Perhaps this could be achieved by electrospinning. However, to electrospin individual fibers with diameters up to 10 μm, a very strong electric field must be used.

REFERENCES

1. Gale, J. *Overview of CO_2 emission sources, potential, transport and geographical distribution of storage possibilities*. *IPCC workshop on carbon dioxide capture and storage*. 2002. Regina, Canada: Energy Research Centre of the Netherlands.

2. Hočevar, S. and W. Summers, *Hydrogen production*, in *Hydrogen Technology*, ed. A. Léon, 2008, Springer-Verlag Berlin Heidelberg.

3. Léon, A., *Hydrogen technology: mobile and portable applications*. Green energy and technology, ed. A. Léon. 2008: Springer-Verlag Berlin Heidelberg.

4. Williams, L.O., *Hydrogen, the optimum fuel*, in *An End to Global Warming.* 2002, Pergamon: Oxford. p. 89-102.

5. Perry, R.H. and D.W. Green, *Perry's Chemical Engineer's Handbook*. 8th ed, ed. R.H. Perry and D.W. Green. 2008, New York: McGraw Hill.

6. Lemcoff, N.O., *Nitrogen separation from air by pressure swing adsorption*, in *Adsorption and its applications in industry and*

environment protection, A. Dąbrowski, Editor 1999, Elsevier: Amsterdam; New York.

7. Agarwal, A., L.T. Biegler, and S.E. Zitney, *A superstructure-based optimal synthesis of PSA cycles for post-combustion CO_2 capteffectively captureure.* AIChE Journal, 2010. **56**(7): p. 1813-1828.

8. Herzog, H., *An introduction to CO_2 separation and capture technologies*, M.E. Laboratory, Editor 1999.

9. Burt, S.S., A. Baxter, C. Bence, and L.L. Baxter. *Cryogenic CO_2 capture for improved efficiency at reduced cost*. in *AIChE Annual Meeting* 2010. Salt Lake City: AIChE.

10. Le Moullec, Y. and M. Kanniche. *Description and evaluation of flowsheet modifications and their interaction for an efficient monoethanolamine based post-combustion CO_2 capture*. 2010.

11. Agarwal, A., L.T. Biegler, and S.E. Zitney, *Superstructure-based optimal synthesis of pressure swing adsorption cycles for precombustion CO_2 capture.* Industrial & Engineering Chemistry Research, 2009. **49**(11): p. 5066-5079.

12. Sircar, S., *Pressure Swing Adsorption.* Industrial & Engineering Chemistry Research, 2002. **41**(6): p. 1389-1392.

13. Baksh, M.S.A. and A.C. Rosinski, *Continuous feed three-bed pressure swing adsorption system*, in http://www.freepatentsonline.com/7179324.html , U.S.P.a.T. Office, Editor 2007, Praxair Technology, Inc. (Danbury, CT, US) : United States.

14. Koros, W.J. and G.K. Fleming, *Membrane-based gas separation.* Journal of Membrane Science, 1993. **83**(1): p. 1-80.

15. Stern, S.A., *Polymers for gas separations: the next decade.* Journal of Membrane Science, 1994. **94**(1): p. 1-65.

16. Bernardo, P., E. Drioli, and G. Golemme, *Membrane Gas Separation: A Review/State of the Art.* Industrial & Engineering Chemistry Research, 2009. **48**(10): p. 4638-4663.

17. Baker, R.W., *Future directions of membrane gas separation technology.* Industrial & Engineering Chemistry Research, 2002. **41**(6): p. 1393-1411.

18. Abetz, V., T. Brinkmann, M. Dijkstra, K. Ebert, D. Fritsch, K. Ohlrogge, D. Paul, K.V. Peinemann, S. Pereira-Nunes, N. Scharnagl, and M. Schossig, *Developments in membrane research: from material via process design to industrial application.* Advanced Engineering Materials, 2006. **8**(5): p. 328-358.

19. Shao, L., B.T. Low, T.-S. Chung, and A.R. Greenberg, *Polymeric membranes for the hydrogen economy: Contemporary approaches and prospects for the future.* Journal of Membrane Science, 2009. **327**(1-2): p. 18-31.

20. Nunes, S.P. and K.V. Peinemann, *Gas Separation with Membranes*. Membrane Technology, 2006: Wiley-VCH Verlag GmbH & Co. KGaA. 53-90.

21. Nunes, S.P. and K.V. Peinemann, *Membrane Market*. Membrane Technology, 2006: Wiley-VCH Verlag GmbH & Co. KGaA. 5-7.

22. Chung, T.-S., L. Shao, and P.S. Tin, *Surface modification of polyimide membranes by diamines for H_2 and CO_2 Separation.* Macromolecular Rapid Communications, 2006. **27**(13): p. 998-1003.

23. Car, A., C. Stropnik, W. Yave, and K.-V. Peinemann, *PEG modified poly(amide-b-ethylene oxide) membranes for CO_2 separation.* Journal of Membrane Science, 2008. **307**(1): p. 88-95.

24. Lin, H., E. Van Wagner, B.D. Freeman, L.G. Toy, and R.P. Gupta, *Plasticization-enhanced hydrogen purification using polymeric membranes.* Science, 2006. **311**(5761): p. 639-642.

25. Patel, N.P., A.C. Miller, and R.J. Spontak, *Highly CO_2-permeable and selective polymer nanocomposite membranes.* Advanced Materials, 2003. **15**(9): p. 729-733.

26. Tong, J., R. Shirai, Y. Kashima, and Y. Matsumura, *Preparation of a pinhole-free Pd-Ag membrane on a porous metal support for pure hydrogen separation.* Journal of Membrane Science, 2005. **260**(1-2): p. 84-89.

27. Wang, D., J. Tong, H. Xu, and Y. Matsumura, *Preparation of palladium membrane over porous stainless steel tube modified with zirconium oxide.* Catalysis Today, 2004. **93-95**: p. 689-693.

28. Merkel, T.C., B.D. Freeman, R.J. Spontak, Z. He, I. Pinnau, P. Meakin, and A.J. Hill, *Ultrapermeable, reverse-selective nanocomposite membranes.* Science, 2002. **296**(5567): p. 519-522.

29. Shao, L. and T.-S. Chung, *In situ fabrication of cross-linked PEO/silica reverse-selective membranes for hydrogen purification.* International Journal of Hydrogen Energy, 2009. **34**(15): p. 6492-6504.

30. Paul, D.R., *Polymeric gas separation membranes*, ed. D.R. Paul and Y.P. Yampol'skii1994: CRC Press.

31. Mulder, M., *Basic principles of membrane technology*. 2nd ed1996, Boston: Kluwer Academic.

32. Barrer, R.M. and D.E.W. Vaughan, *Solution and diffusion of helium and neon in tridymite and cristobalite.* Transactions of the Faraday Society, 1967. **63**: p. 2275-2290.

33. Stern, S.A., *The "barrer" permeability unit.* Journal of Polymer Science Part A-2: Polymer Physics, 1968. **6**(11): p. 1933-1934.

34. Czichos, H., T. Saito, and L. Smith, *Springer handbook of materials measurement methods*, ed. H. Czichos, T. Saito, and L. Smith. Vol. 978. 2006: Springer.

35. Barrer, R.M., J.A. Barrie, and J. Slater, *Sorption and diffusion in ethyl cellulose. Part III. Comparison between ethyl cellulose and rubber.* Journal of Polymer Science, 1958. **27**(115): p. 177-197.

36. Paul, D.R., *Gas sorption and transport in glassy polymers.* Berichte der Bunsengesellschaft für physikalische Chemie, 1979. **83**(4): p. 294-302.

37. Reid, R.C., J.M. Prausnitz, and B.E. Poling, *The properties of gases and liquids*1987. Medium: X; Size: Pages: 741.

38. Merkel, T.C., V.I. Bondar, K. Nagai, B.D. Freeman, and I. Pinnau, *Gas sorption, diffusion, and permeation in poly(dimethylsiloxane).* Journal of Polymer Science Part B: Polymer Physics, 2000. **38**(3): p. 415-434.

39. Merkel, T.C., Z. He, I. Pinnau, B.D. Freeman, P. Meakin, and A.J. Hill, *Effect of nanoparticles on gas sorption and transport in poly(1-trimethylsilyl-1-propyne).* Macromolecules, 2003. **36**(18): p. 6844-6855.

40. Chung, T.-s. and E.R. Kafchinski, *The effects of spinning conditions on asymmetric 6FDA/6FDAM polyimide hollow fibers for air separation.* Journal of Applied Polymer Science, 1997. **65**(8): p. 1555-1569.

41. Lin, W.-H. and T.-S. Chung, *Gas permeability, diffusivity, solubility, and aging characteristics of 6FDA-durene polyimide membranes.* Journal of Membrane Science, 2001. **186**(2): p. 183-193.

42. McKeown, N.B. and P.M. Budd, *Polymers of intrinsic microporosity (PIMs): organic materials for membrane separations, heterogeneous catalysis and hydrogen storage.* Chemical Society Reviews, 2006. **35**(8): p. 675-683.

43. Du, N., H.B. Park, G.P. Robertson, M.M. Dal-Cin, T. Visser, L. Scoles, and M.D. Guiver, *Polymer nanosieve membranes for CO_2-capture applications.* Nature Materials, 2011. **10**(5): p. 372-375.

44. Park, H.B., C.H. Jung, Y.M. Lee, A.J. Hill, S.J. Pas, S.T. Mudie, E. Van Wagner, B.D. Freeman, and D.J. Cookson, *Polymers with cavities tuned for fast selective transport of small molecules and ions.* Science, 2007. **318**(5848): p. 254-258.

45. Avoyan, R.L., Y.T. Struchkov, and V.G. Dashevskii, *Steric hindrance and conformation in aromatic molecules.* Journal of Structural Chemistry, 1967. **7**(2): p. 283-320-320.

46. Yu, J.-W. and C.S.P. Sung, *Imidization Study by Charge Transfer Fluorescence.* Macromolecules, 1997. **30**(6): p. 1845-1846.

47. Bos, A., I.G.M. P¸nt, M. Wessling, and H. Strathmann, *Plasticization-resistant glassy polyimide membranes for CO_2/CO_4 separations.* Separation and Purification Technology, 1998. **14**(1-3): p. 27-39.

48. Koros, W.J., B.J. Story, S.M. Jordan, K. O'Brien, and G.R. Husk, *Material selection considerations for gas separation processes.* Polymer Engineering & Science, 1987. **27**(8): p. 603-610.

49. Tanaka, K., M. Okano, H. Kita, K.-i. Okamoto, and S. Nishi, *Effects of trifluoromethyl side groups on gas permeabilit and permselectivity in polyimides.* Polymer Journal, 1994. **26**(10): p. 1186-1189.

50. Tanaka, K., H. Kita, M. Okano, and K.-i. Okamoto, *Permeability and permselectivity of gases in fluorinated and non-fluorinated polyimides.* Polymer, 1992. **33**(3): p. 585-592.

51. Kratochvil, A.M. and W.J. Koros, *Decarboxylation-induced cross-linking of a polyimide for enhanced CO_2 plasticization resistance.* Macromolecules, 2008. **41**(21): p. 7920-7927.

52. Wind, J.D., C. Staudt-Bickel, D.R. Paul, and W.J. Koros, *Solid-state covalent cross-linking of polyimide membranes for carbon dioxide plasticization reduction.* Macromolecules, 2003. **36**(6): p. 1882-1888.

53. Liu, Y., R. Wang, and T.-S. Chung, *Chemical cross-linking modification of polyimide membranes for gas separation.* Journal of Membrane Science, 2001. **189**(2): p. 231-239.

54. Goodyear, C., *Improvement in the process of divesting caoutchouc gum-elastic, or India-rubber of its adhesive properties, and also of bleaching the same, and thereby adapting it to various useful purposes.* US Patent Office, 1844. **3633**.

55. Tin, P.S., T.S. Chung, Y. Liu, R. Wang, S.L. Liu, and K.P. Pramoda, *Effects of cross-linking modification on gas separation performance of Matrimid membranes.* Journal of Membrane Science, 2003. **225**(1-2): p. 77-90.

56. Shao, L., L. Liu, S.-X. Cheng, Y.-D. Huang, and J. Ma, *Comparison of diamino cross-linking in different polyimide solutions and membranes by precipitation observation and gas transport.* Journal of Membrane Science, 2008. **312**(1-2): p. 174-185.

57. Low, B.T., Y. Xiao, T.S. Chung, and Y. Liu, *Simultaneous occurrence of chemical grafting, cross-linking, and etching on the surface of polyimide membranes and their impact on H_2/CO_2 Separation.* Macromolecules, 2008. **41**(4): p. 1297-1309.

58. Jia, J. and G.L. Baker, *Cross-linking of poly[1-(trimethylsilyl)-1-propyne] membranes using bis(aryl azides).* Journal of Polymer Science Part B: Polymer Physics, 1998. **36**(6): p. 959-968.

59. Kelman, S.D., S. Matteucci, C.W. Bielawski, and B.D. Freeman, *Crosslinking poly(1-trimethylsilyl-1-propyne) and its effect on solvent resistance and transport properties.* Polymer, 2007. **48**(23): p. 6881-6892.

60. Kelman, S.D., B.W. Rowe, C.W. Bielawski, S.J. Pas, A.J. Hill, D.R. Paul, and B.D. Freeman, *Crosslinking poly[1-(trimethylsilyl)-1-propyne] and its effect on physical stability.* Journal of Membrane Science, 2008. **320**(1-2): p. 123-134.

61. Shao, L., J. Samseth, and M.-B. H‰gg, *Crosslinking and stabilization of high fractional free volume polymers for gas separation.* International Journal of Greenhouse Gas Control, 2008. **2**(4): p. 492-501.

62. Shao, L., J. Samseth, and M.-B. H‰gg, *Crosslinking and stabilization of nanoparticle filled PMP nanocomposite membranes for gas separations.* Journal of Membrane Science, 2009. **326**(2): p. 285-292.

63. Shao, L., T.-S. Chung, S.H. Goh, and K.P. Pramoda, *The effects of 1,3-cyclohexanebis(methylamine) modification on gas transport and plasticization resistance of polyimide membranes.* Journal of Membrane Science, 2005. **267**(1-2): p. 78-89.

64. Shao, L., T.-S. Chung, S.H. Goh, and K.P. Pramoda, *Transport properties of cross-linked polyimide membranes induced by different generations of diaminobutane (DAB) dendrimers.* Journal of Membrane Science, 2004. **238**(1-2): p. 153-163.

65. Zhao, H.-Y., Y.-M. Cao, X.-L. Ding, M.-Q. Zhou, and Q. Yuan, *Effects of cross-linkers with different molecular weights in cross-linked Matrimid 5218 and test temperature on gas transport properties.* Journal of Membrane Science, 2008. **323**(1): p. 176-184.

66. Painter, P.C. and M.M. Coleman, *Fundamentals of Polymer Science - An Introductory Text*. 2nd Edition 1997: CRC Press.

67. Sridhar, S., B. Smitha, and T.M. Aminabhavi, *Separation of carbon dioxide from natural gas mixtures through polymeric membranes: A Review.* Separation & Purification Reviews, 2007. **36**(2): p. 113-174.

68. Kim, S., T.W. Pechar, and E. Marand, *Poly(imide siloxane) and carbon nanotube mixed matrix membranes for gas separation.* Desalination, 2006. **192**(1-3): p. 330-339.

69. Park, H.B., J.K. Kim, S.Y. Nam, and Y.M. Lee, *Imide-siloxane block copolymer/silica hybrid membranes: preparation, characterization and gas separation properties.* Journal of Membrane Science, 2003. **220**(1-2): p. 59-73.

70. Chung, T.-S., W.-H. Lin, and R.H. Vora, *The effect of shear rates on gas separation performance of 6FDA-durene polyimide hollow fibers.* Journal of Membrane Science, 2000. **167**(1): p. 55-66.

71. Li, Y., C. Cao, T.-S. Chung, and K.P. Pramoda, *Fabrication of dual-layer polyethersulfone (PES) hollow fiber membranes with an ultrathin dense-*

selective layer for gas separation. Journal of Membrane Science, 2004. **245**(1-2): p. 53-60.

72. Chung, T.-S., E. Swee Phin Loh, and J.-J. Shieh, *A simple approach to estimate gas permeability and selectivity of extremely thin and brittle materials.* Chemical Engineering Science, 2000. **55**(6): p. 1093-1099.

73. Dal-Cin, M.M., K. Darcovich, S. Saimani, and A. Kumar, *Gas separation transport modeling for PDMS coatings on PEI-PEG IPN membranes.* Journal of Membrane Science, 2010. **361**(1-2): p. 176-181.

74. Lin, H. and B.D. Freeman, *Materials selection guidelines for membranes that remove CO_2 from gas mixtures.* Journal of Molecular Structure, 2005. **739**(1-3): p. 57-74.

75. Lin, H., E.V. Wagner, J.S. Swinnea, B.D. Freeman, S.J. Pas, A.J. Hill, S. Kalakkunnath, and D.S. Kalika, *Transport and structural characteristics of crosslinked poly(ethylene oxide) rubbers.* Journal of Membrane Science, 2006. **276**(1-2): p. 145-161.

76. Drohmann, C. and E.J. Beckman, *Phase behavior of polymers containing ether groups in carbon dioxide.* The Journal of Supercritical Fluids, 2002. **22**(2): p. 103-110.

77. Lin, H. and B.D. Freeman, *Gas solubility, diffusivity and permeability in poly(ethylene oxide).* Journal of Membrane Science, 2004. **239**(1): p. 105-117.

78. Kusuma, V.A., B.D. Freeman, M.A. Borns, and D.S. Kalika, *Influence of chemical structure of short chain pendant groups on gas transport properties of cross-linked poly(ethylene oxide) copolymers.* Journal of Membrane Science, 2009. **327**(1-2): p. 195-207.

79. Kusuma, V.A., B.D. Freeman, S.L. Smith, A.L. Heilman, and D.S. Kalika, *Influence of TRIS-based co-monomer on structure and gas transport properties of cross-linked poly(ethylene oxide).* Journal of Membrane Science, 2010. **359**(1-2): p. 25-36.

80. Kusuma, V.A., S. Matteucci, B.D. Freeman, M.K. Danquah, and D.S. Kalika, *Influence of phenoxy-terminated short-chain pendant groups on gas transport properties of cross-linked poly(ethylene oxide) copolymers.* Journal of Membrane Science, 2009. **341**(1-2): p. 84-95.

81. Car, A., C. Stropnik, W. Yave, and K.-V. Peinemann, *Tailor-made polymeric membranes based on segmented block copolymers for CO_2 separation.* Advanced Functional Materials, 2008. **18**(18): p. 2815-2823.

82. Reijerkerk, S.R., A. Arun, R.J. Gaymans, K. Nijmeijer, and M. Wessling, *Tuning of mass transport properties of multi-block copolymers for CO_2 capture applications.* Journal of Membrane Science, 2010. **359**(1-2): p. 54-63.

83. Yave, W., A. Szymczyk, N. Yave, and Z. Roslaniec, *Design, synthesis, characterization and optimization of PTT-b-PEO copolymers: A new membrane material for CO_2 separation.* Journal of Membrane Science, 2010. **362**(1-2): p. 407-416.

84. Simons, K., K. Nijmeijer, J.G. Sala, H. van der Werf, N.E. Benes, T.J. Dingemans, and M. Wessling, *CO_2 sorption and transport behavior of ODPA-based polyetherimide polymer films.* Polymer, 2010. **51**(17): p. 3907-3917.

85. Sridhar, S., R. Suryamurali, B. Smitha, and T.M. Aminabhavi, *Development of crosslinked poly(ether-block-amide) membrane for CO_2/CH_4 separation.* Colloids and Surfaces A: Physicochemical and Engineering Aspects, 2007. **297**(1-3): p. 267-274.

86. Car, A., C. Stropnik, W. Yave, and K.-V. Peinemann, *Pebax®/polyethylene glycol blend thin film composite membranes for*

CO_2 separation: Performance with mixed gases. Separation and Purification Technology, 2008. **62**(1): p. 110-117.

87. Yave, W., A. Car, S.S. Funari, S.P. Nunes, and K.-V. Peinemann, *CO_2-philic polymer membrane with extremely high separation performance.* Macromolecules, 2010. **43**: p. 326-333.

88. Patel, N.P., J.M. Zielinski, J. Samseth, and R.J. Spontak, *Effects of pressure and nanoparticle functionality on co_2-selective nanocomposites derived from crosslinked poly(ethylene glycol).* Macromolecular Chemistry and Physics, 2004. **205**(18): p. 2409-2419.

89. Zoppi, R.A., S. das Neves, and S.P. Nunes, *Hybrid films of poly(ethylene oxide-b-amide-6) containing sol-gel silicon or titanium oxide as inorganic fillers: effect of morphology and mechanical properties on gas permeability.* Polymer, 2000. **41**(14): p. 5461-5470.

90. Wijmans, J.G. and R.W. Baker, *The solution-diffusion model: a review.* Journal of Membrane Science, 1995. **107**: p. 1-21.

91. Wilder, E.A., C.K. Hall, S.A. Khan, and R.J. Spontak, *Effects of composition and matrix polarity on network development in organogels of*

poly(ethylene glycol) and dibenzylidene sorbitol. Langmuir, 2003. **19**: p. 6004-6013.

92. Mu, J., Y. Liu, and S. Zheng, *Inorganic-organic interpenetrating polymer networks involving polyhedral oligomeric silsesquioxane and poly(ethylene oxide).* Polymer, 2007. **48**: p. 1176-1184.

93. Lim, C., S.-I. Hong, and H. Kim, *Effect of polyether diamine on gas permeation properties of organic-inorganic hybrid membranes.* Journal of Sol-Gel Science and Technology, 2007. **43**(1): p. 35-40.

94. Sforça, M.L., I.V.P. Yoshida, and S.P. Nunes, *Organic-inorganic membranes prepared from polyether diamine and epoxy silane.* Journal of Membrane Science, 1999. **159**(1-2): p. 197-207.

95. Kim, H., *Gas permeation properties of organic-inorganic hybrid membranes prepared from hydroxyl-terminated polyether and 3-isocyanatopropyltriethoxysilane.* Journal of Sol-Gel Science and Technology, 2005. **36**(213).

96. Brinker, C.J., *Hydrolysis and condensation of silicates: Effects on structure.* Journal of Non-Crystalline Solids, 1988. **100**(1-3): p. 31-50.

97. Brinker, C.J., K.D. Keefer, D.W. Schaefer, R.A. Assink, B.D. Kay, and C.S. Ashley, *Sol-gel transition in simple silicates II.* Journal of Non-Crystalline Solids, 1984. **63**(1-2): p. 45-59.

98. Brinker, C.J. and G.W. Scherer, *Sol-gel science: the physics and chemistry of sol-gel processing,* 1990, Boston: Academic Press.

99. Hong, S., L. Yang, W.J. MacKnight, and S.P. Gido, *Morphology of a crystalline/amorphous diblock copolymer: poly((ethylene oxide)-b-butadiene).* Macromolecules, 2001. **34**(20): p. 7009-7016.

100. Hong, X., Y.C. Jean, H. Yang, S.S. Jordan, and W.J. Koros, *Free-volume hole properties of gas-exposed polycarbonate studied by positron annihilation lifetime spectroscopy.* Macromolecules, 1996. **29**(24): p. 7859-7864.

101. Yuan, J.-P., H. Cao, E.W. Hellmuth, and Y.C. Jean, *Subnanometer Hole properties of CO_2-exposed polysulfone studied by positron annihilation spectroscopy.* J. Polym. Sci. B: Polym. Phys., 1998. **36**: p. 3049-3056.

102. Eldrup, M., D. Lightbody, and J.N. Sherwood, *The temperature dependence of positron lifetimes in solid pivalic acid.* Chemical Physics, 1981. **63**(1-2): p. 51-58.

103. Tao, S.J., *Positronium annihilation in molecular substances.* The Journal of Chemical Physics, 1972. **56**(11): p. 5499-5510.

104. Nakanishi, N., S.J. Wang, and Y.C. Jean, *In Positron Annihilation Studies of Fluids*, ed. S.C. Sharma, 1988, Singapore: World Scientific.

105. Lin, W.-H., R.H. Vora, and T.-S. Chung, *Gas transport properties of 6FDA-durene/1,4-phenylenediamine (pPDA) copolyimides.* Journal of Polymer Science Part B: Polymer Physics, 2000. **38**(21): p. 2703-2713.

106. Shao, L., T.-S. Chung, S.H. Goh, and K.P. Pramoda, *Polyimide modification by a linear aliphatic diamine to enhance transport performance and plasticization resistance.* Journal of Membrane Science, 2005. **256**(1-2): p. 46-56.

107. Kanehashi, S., T. Nakagawa, K. Nagai, X. Duthie, S. Kentish, and G. Stevens, *Effects of carbon dioxide-induced plasticization on the gas transport properties of glassy polyimide membranes.* Journal of Membrane Science, 2007. **298**(1-2): p. 147-155.

108. Cao, C., T.-S. Chung, Y. Liu, R. Wang, and K.P. Pramoda, *Chemical cross-linking modification of 6FDA-2,6-DAT hollow fiber membranes for*

natural gas separation. Journal of Membrane Science, 2003. **216**(1-2): p. 257-268.

109. Liu, Y., T.-S. Chung, R. Wang, D.F. Li, and M.L. Chng, *Chemical cross-linking modification of polyimide/poly(ether sulfone) dual-layer hollow-fiber membranes for gas separation.* Industrial & Engineering Chemistry Research, 2003. **42**(6): p. 1190-1195.

110. Low, B.T., Y. Xiao, and T.S. Chung, *Amplifying the molecular sieving capability of polyimide membranes via coupling of diamine networking and molecular architecture.* Polymer, 2009. **50**(14): p. 3250-3258.

111. Piwonski, I. and A. Ilik, *Vapor phase modification of sol-gel derived titania (TiO_2) surfaces.* Applied Surface Science, 2006. **253**(5): p. 2835-2840.

112. Ryu, J. and C.B. Park, *High-temperature self-assembly of peptides into vertically well-aligned nanowires by aniline vapor.* Advanced Materials, 2008. **20**(19): p. 3754-3758.

113. Lu, G.H., L.G. Li, and X.N. Yang, *Achieving perpendicular alignment of rigid polythiophene backbones to the substrate by using solvent-vapor treatment.* Advanced Materials, 2007. **19**(21): p. 3594-3598.

114. Voicu, N.E., S. Ludwigs, E.J.W. Crossland, P. Andrew, and U. Steiner, *Solvent-vapor-assisted imprint lithography.* Advanced Materials, 2007. **19**(5): p. 757-761.

115. Hála, E., *Vapour-liquid equilibrium data at normal pressures*. 2nd English ed, ed. E. Hála, 1967, New York: Pergamon Press.

116. NIST, *Antoine equation parameters - ethylenediamine*, in *NIST Standard Reference Database 69: NIST Chemistry WebBook,* 2011, NIST.

117. Silverstein, R.M., F.X. Webster, and D.J. Kiemle, *Spectrometric Identification of organic compounds*. Seventh Edition, 2005: John Wiley & Sons, New Jersey.

118. Aberg, C.M., A.E. Ozcam, J.M. Majikes, M.A. Seyam, and R.J. Spontak, *Extended chemical crosslinking of a thermoplastic polyimide: macroscopic and microscopic property development.* Macromolecular Rapid Communications, 2008. **29**(17): p. 1461-1466.

119. Le Roux, J.D. and D.R. Paul, *Preparation of composite membranes by a spin coating process.* Journal of Membrane Science, 1992. **74**(3): p. 233-252.

120. Kawai, T., Y.M. Lee, A. Higuchi, and K. Kamide, *Separation of mixed gases through porous polymeric membranes.* Journal of Membrane Science, 1997. **126**(1): p. 67-76.

121. Shi, Y., C.M. Burns, and X. Feng, *Poly(dimethyl siloxane) thin film composite membranes for propylene separation from nitrogen.* Journal of Membrane Science, 2006. **282**(1-2): p. 115-123.

122. Gomes, D., K.V. Peinemann, S.P. Nunes, W. Kujawski, and J. Kozakiewicz, *Gas transport properties of segmented poly(ether siloxane urethane urea) membranes.* Journal of Membrane Science, 2006. **281**(1-2): p. 747-753.

123. Robeson, L.M., *The upper bound revisited.* Journal of Membrane Science, 2008. **320**(1-2): p. 390-400.

124. Robeson, L.M., *Correlation of separation factor versus permeability for polymeric membranes.* Journal of Membrane Science, 1991. **62**(2): p. 165-185.

125. Li, F.Y., Y. Li, T.-S. Chung, H. Chen, Y.C. Jean, and S. Kawi, *Development and positron annihilation spectroscopy (PAS) characterization of polyamide imide (PAI)-polyethersulfone (PES) based*

defect-free dual-layer hollow fiber membranes with an ultrathin dense-selective layer for gas separation. Journal of Membrane Science, 2011. **378**(1-2): p. 541-550.

126. Low, B.T., N. Widjojo, and T.S. Chung, *Polyimide/polyethersulfone dual-layer hollow fiber membranes for hydrogen enrichment.* Industrial & Engineering Chemistry Research, 2010. **49**(18): p. 8778-8786.

127. Shao, L., C.-H. Lau, and T.-S. Chung, *A novel strategy for surface modification of polyimide membranes by vapor-phase ethylenediamine (EDA) for hydrogen purification.* International Journal of Hydrogen Energy, 2009. **34**(20): p. 8716-8722.

128. Widjojo, N., S.D. Zhang, T.S. Chung, and Y. Liu, *Enhanced gas separation performance of dual-layer hollow fiber membranes via substructure resistance reduction using mixed matrix materials.* Journal of Membrane Science, 2007. **306**(1-2): p. 147-158.

129. Ren, J., R. Wang, T.-S. Chung, D.F. Li, and Y. Liu, *The effects of chemical modifications on morphology and performance of 6FDA-ODA/NDA hollow fiber membranes for CO2/CH4 separation.* Journal of Membrane Science, 2003. **222**(1-2): p. 133-147.

130. Hosseini, S.S., N. Peng, and T.S. Chung, *Gas separation membranes developed through integration of polymer blending and dual-layer hollow fiber spinning process for hydrogen and natural gas enrichments.* Journal of Membrane Science, 2010. **349**(1-2): p. 156-166.

131. Peng, N., T.-S. Chung, and K.Y. Li, *The role of additives on dope rheology and membrane formation of defect-free Torlon® hollow fibers for gas separation.* Journal of Membrane Science, 2009. **343**(1-2): p. 62-72.

132. *Process for separating ethylene diamine from caustic and sodium chloride*, in *USPTO PatFT*, USPTO, Editor 1975, Chevron Research Company: United States.

133. Brian, C.S., *Fundamentals of Fourier transform infrared spectroscopy,* 1996, Boca Raton: CRC Press.

134. Jiang, L., T.-S. Chung, D.F. Li, C. Cao, and S. Kulprathipanja, *Fabrication of Matrimid/polyethersulfone dual-layer hollow fiber membranes for gas separation.* Journal of Membrane Science, 2004. **240**(1-2): p. 91-103.

135. van't Hof, J.A., A.J. Reuvers, R.M. Boom, H.H.M. Rolevink, and C.A. Smolders, *Preparation of asymmetric gas separation membranes with high selectivity by a dual-bath coagulation method.* Journal of Membrane Science, 1992. **70**(1): p. 17-30.

136. Arumugam, B.K. and P.C. Wankat, *Pressure Transients in Gas Phase Adsorptive Reactors.* Adsorption, 1998. **4**(3): p. 345-354.

137. Namatsu, H., K. Yamazaki, and K. Kurihara, *Supercritical drying for nanostructure fabrication without pattern collapse.* Microelectronic Engineering, 1999. **46**(1-4): p. 129-132.

138. Mukhopadhyay, M. and B.S. Rao, *Modeling of supercritical drying of ethanol-soaked silica aerogels with carbon dioxide.* Journal of Chemical Technology & Biotechnology, 2008. **83**(8): p. 1101-1109.

139. Lee, S.H. and Y.C. Bae, *Thermal stress analysis for polyimide thin film: The effect of solvent evaporation.* Macromolecular Theory and Simulations, 2000. **9**(5): p. 281-286.

140. Liu, Z., A. Maleki, K. Zhu, A.-L. Kjoniksen, and B. Nystrom, *Intramolecular and Intermolecular Association during Chemical Cross-Linking of Dilute Solutions of Different Polysaccharides under the*

Influence of Shear Flow. The Journal of Physical Chemistry B, 2008. **112**(4): p. 1082-1089.

141. Hajji, P., L. David, J.F. Gerard, J.P. Pascault, and G. Vigier, *Synthesis, structure, and morphology of polymer–silica hybrid nanocomposites based on hydroxyethyl methacrylate.* Journal of Polymer Science Part B: Polymer Physics, 1999. **37**(22): p. 3172-3187.

142. Yano, S., K. Iwata, and K. Kurita, *Physical properties and structure of organic-inorganic hybrid materials produced by sol-gel process.* Materials Science and Engineering: C, 1998. **6**(2-3): p. 75-90.

143. Chen, Y., L. Ying, W. Yu, E.T. Kang, and K.G. Neoh, *Poly(vinylidene fluoride) with grafted poly(ethylene glycol) side chains via the RAFT-mediated process and pore size control of the copolymer membranes.* Macromolecules, 2003. **36**(25): p. 9451-9457.

144. Rousseau, F., C. Poinsignon, J. Garcia, and M. Popall, *Polycondensation of Aminosilanes in Methanol.* Chemistry of Materials, 1995. **7**(5): p. 828-839.

145. Chen, H., M.-L. Cheng, Y.C. Jean, L.J. Lee, and J. Yang, *Effect of CO_2 exposure on free volumes in polystyrene studied by positron annihilation*

spectroscopy. Journal of Polymer Science Part B: Polymer Physics, 2008. **46**(4): p. 388-405.

146. Dlubek, G., D. Bamford, A. Rodriguez-Gonzalez, S. Bornemann, J. Stejny, B. Schade, M.A. Alam, and M. Arnold, *Free volume, glass transition, and degree of branching in metallocene-based propylene/alpha-olefin copolymers: Positron lifetime, density, and differential scanning calorimetric studies.* Journal of Polymer Science Part B: Polymer Physics, 2002. **40**(5): p. 434-453.

147. Yave, W., A. Car, S.S. Funari, S.P. Nunes, and K.-V. Peinemann, *CO_2-philic polymer membrane with extremely high separation performance.* Macromolecules, 2009. **43**(1): p. 326-333.

148. Brands, K., D. Uhlmann, S. Smart, M. Bram, and J.o.C.D. da Costa, *Long-term flue gas exposure effects of silica membranes on porous steel substrate.* Journal of Membrane Science, 2010. **359**(1-2): p. 110-114.

149. Lin, H. and B.D. Freeman, *Gas Permeation and Diffusion in Cross-Linked Poly(ethylene glycol diacrylate).* Marcomolecules, 2006. **39**: p. 3568-3580.

150. Bondar, V., A. Alentiev, T. Masuda, and Y. Yampolskii, *Gas sorption in substituted polyacetylenes.* Macromolecular Chemistry and Physics, 1997. **198**(6): p. 1701-1708.

151. Shah, V.M., B.J. Hardy, and S.A. Stern, *Solubility of carbon dioxide, methane, and propane in silicone polymers: Effect of polymer side chains.* Journal of Polymer Science Part B: Polymer Physics, 1986. **24**(9): p. 2033-2047.

152. Chen, H., Y. Xiao, and T.-S. Chung, *Synthesis and characterization of poly (ethylene oxide) containing copolyimides for hydrogen purification.* Polymer, 2010. **51**(18): p. 4077-4086.

153. Patel, N.P., A.C. Miller, and R.J. Spontak, *Highly CO_2-permeable and -selective membranes derived from crosslinked poly(ethylene glycol) and its nanocomposites.* Advanced Functional Materials, 2004. **14**(7): p. 699-707.

154. Hill, R.J., *Reverse-Selective Diffusion in Nanocomposite Membranes.* Physical Review Letters, 2006. **96**(21): p. 216001.

155. Voronin, E.F., V.M. Gun'ko, N.V. Guzenko, E.M. Pakhlov, L.V. Nosach, R. Leboda, J. Skubiszewska-Zieba, M.L. Malysheva, M.V. Borysenko,

and A.A. Chuiko, *Interaction of poly(ethylene oxide) with fumed silica.* Journal of Colloid and Interface Science, 2004. **279**(2): p. 326-340.

156. Beamson, G. and D. Briggs, *High resolution XPS of organic polymers : the Scienta ESCA 300 database,* 1992, West Sussex, England: John Wiley & Sons Ltd.

157. Pohl, E.R. and F.D. Osterholtz, *Molecular characterization of composite interfaces*, ed. H. Ishida and G. Kumar, 1985, New York: Plenum Press.

158. Iler, R.K., *The chemistry of silica: solubility, polymerization, colloid and surface properties, and biochemistry,* 1979, New York: Wiley.

159. Lau, C.H., S. Liu, D.R. Paul, J. Xia, Y.-C. Jean, H. Chen, L. Shao, and T.-S. Chung, *Silica nanohybrid membranes with high CO_2 affinity for green hydrogen purification.* Advanced Energy Materials, 2011. **1**(4): p. 634-642.

160. Lau, C.H. and T.S. Chung, *Effects of Si-O-Si agglomerations on CO_2 transport and separation properties of sol-derived nanohybrid membranes.* Macromolecules, 2011. **44**(15): p. 6057-6066.

161. Raharjo, R.D., H. Lin, D.F. Sanders, B.D. Freeman, S. Kalakkunnath, and D.S. Kalika, *Relation between network structure and gas transport in crosslinked poly(propylene glycol diacrylate).* Journal of Membrane Science, 2006. **283**(1-2): p. 253-265.

162. Dzielawa, J., A. Rubas, C. Lubbers, D. Stepinski, A. Scurto, R. Barrans, M. Dietz, A. Herlinger, and J. Brennecke, *Carbon dioxide solubility enhancement through silicone functionalization: CO_2-philic oligo(dimethylsiloxane)-substituted diphosphonates*.* Separation Science and Technology, 2008. **43**: p. 2520-2536.

163. Wen, J. and G.L. Wilkes, *Organic/inorganic hybrid network materials by the sol-gel approach.* Chemistry of Materials, 1996. **8**(8): p. 1667-1681.

164. Schmidt, P., J. Dybal, and A. Sturcov·, *ATR FTIR investigation of interactions and temperature transitions of poly(ethylene oxide), poly(propylene oxide) and ethylene oxide-propylene oxide-ethylene oxide tri-block copolymers in water media.* Vibrational Spectroscopy, 2009. **50**(2): p. 218-225.

165. Heitz, C., G. Laurent, R. Briard, and E. Barthel, *Cross-condensation and particle growth in aqueous silane mixtures at low concentration.* Journal of Colloid and Interface Science, 2006. **298**(1): p. 192-201.

166. Chen, J., Y. Nho, O. Kwon, and A. Hoffman, *Grafting copolymerization of polyethylene glycol methacrylate (PEGMA) onto preirradiated PP films.* Journal of Radioanalytical and Nuclear Chemistry, 1999. **240**(3): p. 943-948-948.

167. Brinker, C.J. and G.W. Scherer, *Sol→gel →glass: I. Gelation and gel structure.* Journal of Non-Crystalline Solids, 1985. **70**(3): p. 301-322.

168. Lemire, C., R. Meyer, S.K. Shaikhutdinov, and H.J. Freund, *CO adsorption on oxide supported gold: from small clusters to monolayer islands and three-dimensional nanoparticles.* Surface Science, 2004. **552**(1-3): p. 27-34.

169. Zarkanitis, S. and S.V. Sotirchos, *Pore structure and particle size effects on limestone capacity for SO_2 removal.* AIChE Journal, 1989. **35**(5): p. 821-830.

170. Yampolskii, Y., S. Shishatskii, A. Alentiev, and K. Loza, *Correlations with and prediction of activation energies of gas permeation and diffusion in glassy polymers.* Journal of Membrane Science, 1998. **148**(1): p. 59-69.

171. Bondar, V.I., B.D. Freeman, and I. Pinnau, *Gas sorption and characterization of poly(ether-b-amide) segmented block copolymers.*

Journal of Polymer Science Part B: Polymer Physics, 1999. **37**(17): p. 2463-2475.

172. Horas, J.A. and M.G. Rizzotto, *Influence of crystallinity on gas transprt in polymeric films.* Polymer Engineering & Science, 1999. **39**(8): p. 1389-1393.

173. Chen, H.-W., C.-H. Jiang, H.-D. Wu, and F.-C. Chang, *Hydrogen bonding effect on the poly(ethylene oxide), phenolic resin, and lithium perchlorate–based solid-state electrolyte.* Journal of Applied Polymer Science, 2004. **91**(2): p. 1207-1216.

174. Xia, J., S. Liu, C.H. Lau, and T.-S. Chung, *Liquid-like poly(ethylene glycol) supported in the organic-inorganic matrix for CO_2 removal.* Macromolecules, 2011. **44**(13): p. 5268-5280.

175. Mogri, Z. and D.R. Paul, *Gas sorption and transport in poly(alkyl (meth)acrylate)s. I. Permeation properties.* Polymer, 2001. **42**(18): p. 7765-7780.

176. Mogri, Z. and D.R. Paul, *Gas sorption and transport in poly(alkyl (meth)acrylate)s. II. Sorption and diffusion properties.* Polymer, 2001. **42**(18): p. 7781-7789.

177. Yang, J.-S. and G.-H. Hsiue, *Swollen polymeric complex membranes for olefin/paraffin separation.* Journal of Membrane Science, 1998. **138**(2): p. 203-211.

178. Susanto, H. and M. Ulbricht, *Polymeric membranes for molecular separations*, in *Membrane Operations,* 2009, Wiley-VCH Verlag GmbH & Co. KGaA. p. 19-43.

179. Yave, W., A. Car, K.-V. Peinemann, M.Q. Shaikh, K. Rtzke, and F. Faupel, *Gas permeability and free volume in poly(amide-b-ethylene oxide)/polyethylene glycol blend membranes.* Journal of Membrane Science, 2009. **339**(1-2): p. 177-183.

180. Metz, S.J., M.H.V. Mulder, and M. Wessling, *Gas-permeation properties of poly(ethylene oxide) poly(butylene terephthalate) block copolymers.* Macromolecules, 2004. **37**(12): p. 4590-4597.

181. Xia, J., S. Liu, and T.-S. Chung, *Effect of end groups and grafting on the CO_2 separation performance of poly(ethylene glycol) based membranes.* Macromolecules, 2011. **44**(19): p. 7727-7736.

182. Patil, P.N., S.K. Rath, K. Sudarshan, D. Dutta, M. Patri, and P.K. Pujari, *Effect Of cross-link density on the free volume and segmental relaxation*

in epoxy resin studied by positron annihilation spectroscopy. AIP Conference Proceedings, 2010. **1313**(1): p. 298-300.

183. Suzuki, H., K. Tanaka, H. Kita, K. Okamoto, H. Hoshino, T. Yoshinaga, and Y. Kusuki, *Preparation of composite hollow fiber membranes of poly(ethylene oxide)-containing polyimide and their CO2/N2 separation properties.* Journal of Membrane Science, 1998. **146**(1): p. 31-37.